Variability of Hydroclimate in the North American Southwest: Implications for Streamflow, the Spring Dry Season and Ecosystems

Madeleine Pascolini-Campbell

Submitted in partial fulfillment of the
requirements for the degree of
Doctor of Philosophy
in the Graduate School of Arts and Sciences

COLUMBIA UNIVERSITY

2018

ABSTRACT

Variability of Hydroclimate in the North American Southwest: Implications for Streamflow, the Spring Dry Season and Ecosystems

Madeleine Pascolini-Campbell

The Southwest United States (SWUS) is facing an ongoing drought which has led to water shortages, in addition to forest mortality due to wildfire and bark beetle outbreaks associated with increased temperatures. This region has a population of 9.6 million people and is one of the fastest growing parts of the United States, and pressure on its resources can be expected to increase in the future. The SWUS is also projected to become more arid in the coming century under greenhouse gas induced climate change, which will impact its environmental, economic and social vitality. This thesis explores the climate dynamics which control water availability, streamflow, and vegetation green-up in the SWUS, in order to constrain our understanding of the mechanisms controlling the ecohydrology of the region, and to inform projections for the 21st century.

Chapters 1 and 2 investigate the climate drivers responsible for producing the observed variability in streamflow for the Gila River, a tributary of the Colorado, and the upper Rio Grande. The Gila is the southernmost snowfed river in the SWUS, and has a spring streamflow peak that responds to melting of the snowpack at its headwaters in New Mexico. The Gila is also sufficiently south so that it has a secondary streamflow peak in the summer which is fed by rains from the North American Monsoon (NAM). On interannual timescales, the Gila's spring peak is primarily influenced by natural variability associated with Pacific sea surface temperature (SST), while the summer peak apparently does not respond to interannual variability. The upper Rio Grande is further north and east in the SWUS, and only has one streamflow peak occurring in spring-summer

which is influenced by both tropical Pacific SST and Atlantic SST. Spring streamflow has also declined in each river post-1998, and this is due to a shift in the tropical Pacific leading to negative precipitation anomalies and drying in the SWUS.

Chapter 2 assess a region of the SWUS that receives both winter storm track precipitation and NAM, and therefore has two periods of vegetation green-up annually with an intervening spring dry season. The first peak in vegetation occurs during the spring, and is influenced by the magnitude of winter precipitation and snowmelt, which gradually adds water to the soils. The second peak in vegetation follows the spring dry season when soil moisture recovers with the arrival of the NAM. A climatic shift in the tropical Pacific occurred in 1997/98 and produced a shift to an earlier and more severe spring dry season, and reduced vegetation green-up. An earlier extended dry period in the mid-century (1948 to 1966) also was influenced by a cool phase of the tropical Pacific, which led to a reduction in precipitation of a similar magnitude as the recent drought. However, the recent drought is more severe - and temperatures also have been greater during the recent period. Using a decomposition of the impact of precipitation and potential evapotranspiration (PET) on soil moisture, we found that PET contributed 39% to the negative soil drying anomalies in the recent post-1998 drought, compared to 8% during the earlier extended dry period. This indicates an increased role of temperature during the recent drying.

In Chapter 4 we evaluated 18 CMIP5 models based on comparisons with observations of precipitation, net ecosystem exchange, leaf area index and soil moisture from land surface model output. Following our evaluation, we selected three models which best simulated the bimodal region: CanEMS2, GFDL-ESM2G and GFDL-ESM2M. These models indicate that overall this region will be drier in the 21st century; runoff is projected to decrease, particularly in the spring, soil moisture is reduced, and snow fall declines. The variability in projected precipitation, how-

ever, is large, and we find that for the most part does not exceed what can be expected from model natural climate variability. The multi-model ensemble from the rest of the CMIP5 models indicate an overall decline in annual precipitation by the end of the 21st century, particularly during the spring. The three models also project an increase in net primary productivity in both the spring and summer growing seasons due to the effects of CO_2 fertilization. Enhanced vegetation growth is likely to further exacerbate drying of the soils as vegetation draws down moisture, and enhances water losses via evapotranspiration. The fertilization process is, however, still uncertain and further studies are needed on the representation of CO_2 enhanced vegetation growth in the SWUS to constrain this result.

The findings of this thesis have contributed enhanced our knowledge of how climate dynamics, natural variability, and recent warming have influenced the ecohydrology of the SWUS, and also inform future climate projections. Constraining our understanding of this region is of importance given the growing populations, mounting pressures on natural resources, and anthropogenically induced climate change which is expected to affect this region in the 21st century.

Contents

List of Figures

List of Tables

Acknowledgements

I would like to acknowledge my advisor, Richard Seager, and committee members, Benjamin Cook and Mingfang Ting for providing guidance throughout my PhD. I would like to thank my collaborators David Gutzler, Daniel Griffin, Ariane Pinson and Park Williams for their valuable contributions. I would also like to thank Naomi Henderson for computing support.

Introduction

The interior SWUS covers the states of Arizona and New Mexico, and parts of southern Colorado, Nevada and western Texas, is heavily populated, with the major metropolitan areas (including Pheonix, Arizona, Tucson, Arizona, Las Vegas, Nevada, Albuquerque, New Mexico, and El Paso, Texas) totaling more than 9.6 million people in 2017 (United States Census Bureau 2018). The population of the SWUS, as well as demands on resources, is growing (Konieczki and Heilman 2004). Further, the economic and social vitality of the SWUS is closely related to its natural environment, and its future will depend on how the climate responds to warming in upcoming decades.

The SWUS is beset by numerous environmental crises. The region faces water shortages due to an ongoing drought, and reservoir levels along the Colorado River dropped to historically low levels in 2005 (Fulp 2005; Rajagopalan et al. 2009) and are yet to recover to the levels typical of the latter part of the 20th century. The water supply of the upper Rio Grande, which supplies water to 5 million people in the SWUS, has also declined in both quantity and quality (Dahm et al. 2005). Wildfires and bark beetle outbreaks have devastated southwestern forests (Mantgem et al. 2009); a predicted $\sim$18% of forested areas experienced mortality due to all causes in the SWUS between 1984 and 2006 (Williams et al. 2010). These crises are directly influenced by temperature and moisture availability, and it is therefore of importance to have a robust understanding of the underlying climate mechanisms operating in this region that are driving this natural resource and ecological transformation.

Natural climate variability in the SWUS

The SWUS is highly sensitive to moisture inputs, and is affected by both natural climate variability and anthropogenic climate change. Multiple systems including streamflow, ecosystems and soil water storage, are interrelated through complex dynamics and respond to changes in precipitation and snowpack, which are in turn influenced by modes of climate variability associated with sea surface temperature (SST) in the Pacific and Atlantic Oceans.

The complex dynamics of these natural systems are also influenced by human populations in the SWUS. Humans rely on streamflow and groundwater for domestic and industrial consumption and agriculture, and rising population has placed fresh water availability under pressure. In addition, the SWUS has experienced persistent droughts this century. Warming temperatures have reduced streamflow and snowpack and further stressed water resources in this region. This highlights the necessity for a comprehensive understanding of how natural climate variability and climate change influence the ecohydrology of the SWUS. This dissertation will i) investigate how natural climate variability influences streamflow, ecosystems and water availability, ii) how anthropogenic climate change has influenced these systems, and iii) explore 21st century climate projections to identify potential changes to these systems in future.

The SWUS is influenced by climate variability associated with the El Niño-Southern Oscillation (ENSO) on interannual timescales (Kahya and Dracup 1994; Ropelewski and Halpert 1986, 1989; Trenberth et al. 1998), and the Pacific Decadal Oscillation (PDO) (Zhang et al. 1997; Mantua et al. 1997), as well as the Atlantic Multidecadal Oscillation (AMO) on longer timescales (Enfield et al. 2001). ENSO leads to above normal winter precipitation in the SWUS during its warm phase (El Niño) and below normal precipitation during its cold phase (La Niña), hence influencing in-

terannual SWUS streamflow (Thomas 2007; Nowak et al. 2012). The PDO also produces above normal precipitation for the SWUS during the warm phase, with the last recorded warm phase occurring from 1977 to around 1997 and a cold phase persisting since then (Mantua et al. 1997) . The cold AMO produces positive precipitation anomalies in the SWUS. These teleconnections are strengthened when acting together, with a warm (cold) PDO or ENSO and cold (warm) AMO producing optimal wet (dry) conditions for the SWUS (McCabe et al. 2004; Schubert et al. 2009). Further nuances include the imperfect relationship between SWUS precipitation and SST, as evidenced by the failure of the recent warm ENSO event to deliver above-normal precipitation (Jong et al. 2017). This is likely due to the influence of internal atmospheric variability that is not related to SST.

The SWUS also is influenced by the North American Summer Monsoon (NAM), which delivers northern hemisphere summer (July-August-September (JAS)) rainfall (Adams and Comrie 1997; Barlow et al. 1998). The core region of the NAM extends from Mexico north to Arizona and New Mexico, and is fed by moisture from both the Gulf of Mexico and the Gulf of California (Adams and Comrie 1997). The arrival of the NAM varies year-to-year, and is weakly modulated by ENSO (Higgins et al. 1999; Castro et al. 2001), the Madden-Julian-Oscillation (MJO) (Higgins and Shi 2001), and prior soil moisture (Small 2001). The NAM provides a critical source of moisture to the region during the warm summer months when temperatures locally rise above 40^{o}C (Adams and Comrie 1997).

The combination of winter precipitation (in the form of rain and snow) and summer NAM rainfall, together with soil moisture, runoff, and vegetation, and their interactions, controls the ecohydrology of the SWUS. Winter precipitation falls as snow in the high peaks of the SWUS, particularly in the north, and the moisture is released as snowmelt in the spring. The gradual

release of water as snowmelt allows water to infiltrate soils and build up moisture storage in the spring (Loik et al. 2004). The delay in the release of water from snowpack melt also dictates the timing of water delivery to rivers, and year-to-year variability in snowpack critically impacts the magnitude of spring and summer streamflow pulses (Stewart et al. 2005). The build up of soil moisture from winter precipitation and snowmelt leads to vegetation green-up in the spring (Notaro et al. 2010; Muldavin et al. 2008), which draws down water passing it to the atmosphere by evapotranspiration (ET). The magnitude and timing of these moisture inputs, and the variations in water storage in soils, is of significance for controlling the onset of wildfires. Reductions in winter moisture availability, during cold phases of ENSO, have led to earlier and larger area of fire outbreaks in the western United States (Swetnam and Betancourt 1990).

Summer precipitation arrives in the form of convective rainfall associated with the NAM, and is often more intense (Loik et al. 2004). Unlike the steady build up of soil moisture with the gradual winter snowmelt, summer moisture inputs are more easily lost to surface runoff and ET which is high due to high summer temperatures causing high potential ET. Vegetation uptake of moisture is more concurrent in the summer, with pulses of green-up occurring concurrently with rainfall episodes (Notaro et al. 2010).

Investigating streamflow variability in the SWUS is also nuanced by elevation change throughout the river basins. Much of the streamflow of SWUS rivers is generated by the melting of the winter snowpack from higher elevations at the headwaters. Melting produces runoff during the spring and summer, which is transported by streams to lower elevations. This therefore creates a mismatch between the main geographic region producing runoff, and the regions where the runoff is used by humans, as well as lost via evapotranspiration. The role of temperature on evapotranspiration losses will also vary according to location within the basin. Understanding the variability

of streamflow further downstream in the basins therefore requires an investigation of the climate in the runoff-producing region at higher elevations.

Anthropogenic influence in SWUS to date

Temperatures have warmed in the SWUS by 0.9^{o}C from 1901 to 2010 (Hoerling and Kunkel 2013), with current temperatures exceeding previous droughts in the paleoclimatic record (Woodhouse et al. 2010). Although SWUS droughts are primarily driven by precipitation variability (Wigley and Jones 1985; Karl and Riebsame 1989; Williams et al. 2015a), the severity of droughts in the latter half of the century cannot be explained by low precipitation alone, and have increasingly been driven by high temperatures (Woodhouse et al. 2016; Williams et al. 2015a), which also have contributed to reduced runoff efficiency in the SWUS (Lehner et al. 2017).

Rising twentieth-century temperatures have also been linked to the observed decline in western United States snowpack (Mote et al. 2005, 2018), and its earlier melt (Cayan et al. 2001). This has contributed to the earlier onset of spring in the SWUS, detected in blooming (Cayan et al. 2001; Ault 2015), and also has led to earlier spring and summer streamflow (Fritze et al. 2011; Regonda et al. 2005). The dry season that occurs following winter precipitation and before the arrival of the summer NAM, has also shifted to earlier in the year. This has contributed to an earlier onset of the wildfire season (Westerling et al. 2006; Williams et al. 2014) and also has enhanced dust emissions (Hand et al. 2016).

Projections for the 21st century in the SWUS: climate models

The SWUS is projected to become warmer and drier in the 21st century (Seager et al. 2007; Seager and Vecchi 2010a), with temperatures expected to rise by 1.5 to 6 ^{o}C(IPCC, 2001). The anticipated drying is mainly due to a reduction in winter precipitation and moisture availability, and poleward expansion of the subtropical dry zones, and this is anticipated to exceed natural climate variability by the middle of the 21st century (Seager and Vecchi 2010b; Greene and Seager 2016). Drying is projected to be particularly severe during the spring (Gao et al. 2014; Ting et al. 2018), which will exacerbate the natural spring drying which already occurs seasonally in the SWUS. The projected drying will continue to deplete fresh water resources which will put additional strain on already heavily allocated rivers such as the Colorado (Rajagopalan et al. 2009).

The NAM has also been projected to have a delayed onset in the future (Cook and Seager 2013), or an overall reduction in magnitude (Pascale et al. 2017). Coupled with projected reductions in winter precipitation, this would reduce summertime recovery of soil moisture, vegetation green up, as well as reduce the magnitude of summertime streamflow pulses. However, there remains considerable uncertainty in model projections of the NAM.

As discussed above, the hydroclimate of the SWUS is dominated by the influence of modes of climate variability associated with Pacific and Atlantic SST. Future changes to precipitation in this region will also depend on the strength of the teleconnections in the future, and how they interact against a background of warming temperatures (Meehl and Teng 2007). Following the 2015/16 El Niño, the Pacific has been forecast to return to warmer conditions (Ramesh et al. 2017). If this forecast is true it would imply that human-induced aridification of the SWUS in the upcoming decades will be offset to some extent by the wetting tendency resulting from the warm phase of the

PDO (McCabe et al. 2004; Huang et al. 2005). However decadal forecast skill is very limited and alternative scenarios where human induced change and natural variability combine to exacerbate drying, should also be considered.

Under increased atmospheric CO_2, the SWUS has also been projected to become greener due to enhanced vegetation growth via CO_2 fertilization effects (Mankin et al. 2017, 2018a). Examining climate models, enhanced vegetation growth in the SWUS was found to enhance water losses of soils via uptake in plant growth and evaporative losses (Mankin et al. 2017). This process was also found to occur despite the effects of decreased stomatal conductance under high CO_2, with its potential to offset soil moisture drying through decreasing ET (Milly and Dunne 2016). The overall projected impact is a "greener and drier" SWUS - enhanced soil drying and decreased delivery of runoff to rivers but higher net primary production. This study also, however, is still analysis of climate model projections, and it is not clear whether the real-world will respond in this way (see discussion in Cook et al. (2016), Mankin et al., (2017, 2018)).

Implications for other systems

The climate mechanisms (ENSO, PDO, AMO, NAM), warming temperatures and climate projections discussed above are also of importance for other systems including wildfires, ecosystems, agriculture and dust emissions.

Wildfire in the SWUS is strongly influenced by the vapor pressure deficit (the difference between actual vapor pressure of the air and saturation vapor pressure), which increases with temperature (Williams et al. 2012). A reduced winter snowpack and earlier melt has also has led to an earlier outbreak of the wildfire season in the western United States (Westerling et al. 2006). Tem-

perature increases in the SWUS have contributed to greater bark-beetle outbreaks since warmer conditions favor beetle population growth and can stress trees (Bentz 2008). In recent decades beetle outbreaks have devastated forests in the western United States (Abatzoglou and Williams 2016; Westerling et al. 2006; Penelope et al. 2008; Raffa et al. 2008). Some studies have also suggested that forest mortality, due to, for example, drought, also leads to greater wildfire outbreak from increased fuel supply (Christof et al. 2005; Jenkins et al. 2008).

Summer vegetation green-up in the SWUS responds concurrently to moisture inputs, and is therefore primarily controlled by timing and magnitude of the summer NAM (Weiss et al. 2004; Notaro et al. 2010; Muldavin et al. 2008). The concurrent response of vegetation to moisture is known as the 'pulse-reserve' paradigm, in which vegetation productivity follows pulses of rainfall (Noy-Meir 1973). The earlier annual spring vegetation green-up instead has a delayed response to moisture input, and is influenced by the amount of water stored in soils delivered via winter precipitation and the gradual melting of the snowpack (Notaro et al. 2010). Collectively investigating the climate controls on winter precipitation, snowpack and melt, and the NAM is therefore needed to understand the timing of these separate green-ups and the dry season that separates them.

Fish species are important components of SWUS ecosystems that are influenced by the magnitude and timing of spring-summer streamflow, and there are166 and 98 species in the Rio Grande and Colorado River respectively, many of which are endangered (Dahm et al. 2005). The fragmentation of streams (which increases during dry years) is deleterious to the spawning of fish (Perkin and Gido 2011; Dudley and Platania 2007). An overall reduction in streamflow during low flow years is also harmful to aquatic ecosystems (Jaeger et al. 2014; Perkin and Gido 2011), and this is of concern given projections towards reduced runoff for the SWUS in the future (Seager et al. 2013; Barnett et al. 2008; Mankin et al. 2017; Ting et al. 2018). The SWUS is also home to a

number of bird species, including geese, ducks, ibis, cranes as well as 37 species of shorebirds, among others (Dahm et al. 2005), and bird activity is in addition important for influencing nutrient cycling. Riparian environments are also important as they connect low lying and upper elevation ecosystems and are cool refuges against warming - if they remain continuous with shading by vegetation, and are also of importance to migrating birds (Skagen et al. 1998).

Water availability is of essential importance to humans and is extracted for domestic use, industry, and, primarily, agriculture which accounts for $\sim$80% of all SWUS water withdrawals (MacDonald 2010). Water extraction to support the growing population has increased since the mid-20th century, and can be expected to continue given population growth (Konieczki and Heilman 2004). The Colorado, and upper Rio Grande Rivers are both heavily allocated in a number of river compacts to provide water to the states of Arizona, California, Colorado, Nevada, New Mexico, Utah and Wyoming, and water is also allocated to Mexico through international agreements (Konieczki and Heilman 2004). Ongoing drought means that these critical resources are under stress, and the climate dynamics that influence water supply are therefore of significance for water resource management.

Contribution of this thesis to the literature

The drivers of streamflow in the SWUS have been investigated heavily for the Colorado River, with much research indicating an influence of SST on interannual and interdecadal streamflow variability (Redmond and Koch 1991; Kahya and Dracup 1994; Hidalgo and Dracup 2003). The drivers of streamflow for the upper Rio Grande and the Gila have not yet been assessed to the same extent. The upper Rio Grande is of importance for delivering water to the downstream reaches of

the river, as well as locally providing water for domestic use, industry and agriculture (Woodhouse et al. 2012), and the Gila River is an important tributary to the Colorado (Gutzler 2013), and is the most southward of the snow fed streams in North America.

Current studies indicate the importance of ENSO in influencing upper Rio Grande streamflow (Lee et al. 2004; Khedun et al. 2010). However, these studies do not include the impact of Atlantic SST, and also begin from observations in $\sim$1950. This thesis aims to extend previous studies using longer time-scale observations from stream gages, and proxy streamflow reconstructions from tree-rings, enabling a more thorough observation of longer term decadal variability. This will also permit extended periods of drought and pluvials to be contrasted in order to place the ongoing SWUS hydrological drought into a historical perspective. Streamflow variability on interannual to interdecadal timescales from these two rivers will have important implications for water resource management. The work reported here, therefore, provides an analysis of the relation between climate and streamflow in the SWUS that is more expansive in space and time than has heretofore been presented.

Ecosystem vitality in the SWUS is also highly sensitive to moisture inputs from winter precipitation and the summer NAM. The severity of the dry season which exists between these two annual sources of moisture is also affected by the magnitude of winter precipitation. Storage of water in the soil connects the delivery of water by precipitation and snowmelt and its transfer back to the atmosphere via ET, and is highly seasonally variable with late winter and summer peaks. These complex interactions are also expected to vary on interannual and interdecadal timescales due to natural climate variability in the Pacific and Atlantic Oceans and will change as human-driven climate change advances. This thesis decomposes the different mechanisms involved in the complex ecohydrology of the SWUS to provide insight into the coupling between winter precipitation and

snowmelt, summer NAM, soil water storage, vegetation growth and losses via ET.

As noted above, the nature of droughts has also been observed to change in the SWUS, droughts in recent decades being intensified by higher temperatures (Woodhouse et al. 2016). This thesis will also explore how warming temperatures in the SWUS have affected hydroclimate and ecosystems in this region to date. In particular, this thesis will examine whether the post-1999 dry period of reduced precipitation and lower streamflow ongoing in the SWUS is due to human driven climate change or natural decadal variability. This will provide valuable information on the impact of warming on these systems, and will also inform future changes given projected temperature and aridity increases for the 21st century (Seager et al. 2007).

Following the exploration of climate dynamics, this thesis will turn to climate models projections for the SWUS to determine anticipated 21st century changes in hydroclimate and vegetation vitality. In particular, this thesis will build on previous studies that have investigated SWUS model projections (e.g. Seager et al. 2007, Gao et al. 2014, Ting et al. 2018), by focusing on the dual green-up region and evaluating which models best simulate the complexity of this region, and then examining their projections of hydroclimate and ecosystems. Many climate models do not simulate this region well, and this is taken into consideration as an important caveat when results are presented.

The questions examined in this thesis are as follows:

1. What are the mechanisms that couple together precipitation, runoff, soil moisture, and vegetation in the SWUS?

2. What role does natural climate variability play on i) interannual, ii) interdecadal timescales in driving variability of these complex ecohydrological systems?

3. Is the influence of anthropogenically-forced warming and/or precipitation change detectable in the historical record?

4. How do we expect the complex ecohydrological system of the SWUS to change in future?

Chapter 1 and Chapter 2 address these questions in the context of streamflow variability and change for the Gila River and upper Rio Grande. Chapter 3 investigates the interaction of hydroclimate and vegetation growth in the context of and variability and change of the dual green-up region of the spring season in the SWUS. And finally, Chapter 4 turns to climate model projections to suggest possible future changes for the 21st century in this region. We then present our conclusions.

1 Causes of Interannual to Decadal Variability of Gila River Streamflow over the Past Century

1.1 Introduction

The Gila River flows approximately 600 miles west across Arizona, from its headwaters in New Mexico to join the Colorado River just above its mouth. The Gila River receives water from both extratropical winter storms and the North American Monsoon, producing a complex hydrograph with spring and summer peak flows (Gutzler 2013). The Gila River has been gaged since 1928 and its historical flows show considerable interannual to decadal variability (ibid.). Precipitation and streamflows of other rivers in the Southwest have been shown to be affected by various mechanisms, including responses to Pacific and Atlantic sea surface temperature (SST) anomalies (Gutzler et al. 2002; Sheppard et al. 2002; McCabe et al. 2004). In addition to the influences of climate variability, aridity in the Southwest United States is projected to intensify with global warming (Seager et al. 2007, 2014) and this will have implications for precipitation and streamflow in the region. Understanding these varying influences on streamflow is vital for producing reliable projections of future streamflows and water resources in the coming decades.

The Gila River is a vital source of water for multiple groups in New Mexico and Arizona including farmers, industries, and local communities including the Gila River Indian Community. It supplies water to Catron, Grant, Hidalgo and Luna Counties, New Mexico, for varied purposes including agriculture (which accounts for 86 percent of water consumption in the state (Liverman and Merideth 2002)), commercial use, industry, mining and power extraction. The Gila River is also the subject of an ongoing debate on planning for water use in New Mexico as allowed under

the Arizona Water Settlements Act (AWSA). The social importance of the river motivates the need for improved scientific understanding of the mechanisms responsible for its flow.

Here we present the first comprehensive study of historical Gila River flow variability. Since the river is fed by 1) snowmelt in the spring and 2) the North American Monsoon in the summer, attention must focus on both winter and summer season climate variability. Many previous studies have demonstrated the connection between Southwest precipitation during the winter and Pacific Ocean SST anomalies (Molles and Dahm 1990; Redmond and Koch 1991; Kahya and Dracup 1993, 1994; Cayan et al. 1999; Seager et al. 2005a). This connection is primarily due to the El Niño-Southern Oscillation (ENSO) (Cayan et al. 1999), a coupled atmosphere-ocean phenomenon with equatorial Pacific SST varying at the 2 to 7 year timescale and being strongest during the winter (December-January-February (DJF)) season (e.g. (Trenberth 1997)). The Pacific Decadal Oscillation (PDO) has also been found to influence hydroclimate in the region (Barlow et al. 2001). Those studies found that winters of warm SST anomalies (El Niño events) precede higher than average spring streamflow and precipitation in southwest North America, and periods of cold SST anomalies (La Niña events) tended to go along with low precipitation and streamflow (Cayan et al. 1999). Focusing on precipitation variability, modeling studies have also indicated the importance of Pacific SST anomalies in generating persistent, multiyear, droughts and pluvials in North America (Schubert et al. 2004; Seager et al. 2005b), and multidecadal precipitation variability (Seager et al. 2014).

From Mexico into the southwestern U.S., the North American Monsoon brings a summer (July-August-September (JAS)) peak in rainfall (Adams and Comrie 1997; Barlow et al. 1998) and Monsoon variability presumably can also drive streamflow variability, including of the Gila. Modeling studies have indicated that greenhouse gas (GHG) warming could delay both Monsoon onset and

retreat (Seth et al. 2013; Cook and Seager 2013) though changes in the Monsoon by region have not yet been closely examined. In addition, the role of increased temperature and potential evapotranspiration rates is predicted to have an impact on the hydrology of the region, adding a further dimension to streamflow change in the future (Hurd and Coonrod 2008; Gutzler 2013).

This study will investigate historical variability of Gila River flow, the nature of the double peaked hydrograph, and in particular the association of flow to SST anomalies in the Pacific and Atlantic Oceans. Key questions addressed will include: 1) precipitation variability in which months best explains the variability of the two peak streamflows?, 2) how are precipitation over the basin and streamflow related to SST anomalies?, 3) what is the relationship of flow variability to ENSO?, and 4) what is the nature and cause of the decadal variability of Gila River flow since 1928. Future climate change impacts on Gila River flow are not examined here (but see (Gutzler 2013)). Instead we use observations to explain the past flow variability as one necessary step to understanding its potential present and future predictability.

1.2 Data and Methodology

To investigate streamflow and climate variability four observational datasets for the time period of 1928 to 2012 are used. This time span is used as the base period from which climate anomalies are calculated. For streamflow we use mean daily values for the upper Gila River from United States Geological Survey (USGS) Gage Data (in units of cubic meters per second (c.m.s.)) (USGS gage 09430500) (data last accessed 12/10/2014 online at http://http://waterdata.usgs.gov/) (Gila River and position of USGS gage shown in Figure 1). For precipitation we use two datasets: the first is from the Global Precipitation Climatology Center (GPCC) (in units of mm/month on

a 0.5°x0.5° global grid) which is used for generating data over North America for 1928 to 2010 (Schneider et al., 2011). The second precipitation dataset used is from the Parameter Regression on Independent Slopes Model (PRISM; in units of mm/month on a 4km grid), which uses a well-verified, terrain-sensitive algorithm to interpolate between available stations over the period 1895-present (Daly et al. 2008a). To focus on watershed specific variability, PRISM data was extracted for the Upper Gila Basin (U.S.G.S. Hydrologic Unit Code 150400) using the Westmap internet tool (http://www.cefa.dri.edu/Westmap/). The interpolation between stations in the PRISM data is sensitive to elevation changes, which is important given the varying topography of the study region. For SST, ERSST V3 reanalysis data (in units of degrees Celsius on a 2°x2° global grid) are used (Smith et al. 2008). A reconstruction of the Palmer Drought Severity Index (PDSI) for the United States, based on tree ring data within the North American Drought Atlas (NADAV2a), is used since 1530 A.D. (Cook et al. 2004, 2007, 2010). Season-specific moisture variability in the pre-instrumental era was assessed with tree-ring reconstructions to create the Standardized Precipitation Index (SPI) for the 7-month season ending in April and the 3-month season ending in August for 1530 to 2008 (Griffin et al. 2013). For evapotranspiration, precipitation and temperature output is used from the Global Land Data Assimilation System (GLDAS) Common Land Model (CLM) (1979 to 2000) (Rodell et al. 2004), the Variable Infiltration Capacity (VIC) hydrological model (1929 to 2003) (Liang 1994) as well as NCEP-NCAR CDAS-1 Reanalysis data (1948 to 2012) (Kalnay et al. 1996) ((in units of kg/m^2/s for precipitation and evapotranspiration, and degrees Celsius for temperature, on a 1°x1° global grid). The Variable Infiltration Capacity (VIC) hydrological model is also used for evapotranspiration, precipitation and temperature from 1929 to 2003 (Liang 1994) .The GPCC precipitation, SST and PDSI datasets are available online at the International Research Institute Institute for Climate and Society (IRI) data library

(http://iridl.ldeo.columbia.edu/).

To investigate precipitation variations over the Gila River Basin, a time series is constructed from the PRISM data for the Upper Gila Hydrological Unit. Regions affected by the North American Monsoon have been found to contain large degrees of spatial heterogeneity in rainfall and temperature trends, related to the spatially varying nature of convective cloud activity (Gebremichael et al. 2007) , making it important to examine links between Gila River flow and precipitation on the scale of the basin itself. For example stronger correlation between precipitation and streamflow was found to exist when using the PRISM Upper Gila Hydrological Unit Precipitation compared with a rectangular box containing the Gila River catchment upstream of the gage (spanning 108.5°W to 111.5°W and 31.5°N to 33.5°N). Pacific Ocean SST variability related to ENSO is investigated using the Niño-4 index, which is the SST anomaly averaged over the area bound by 5°N to 5°S and 150°W to 160°E. The Niño-4 index is used rather than the Niño-3.4 index due to the greater correlation of Gila streamflow and precipitation with the former index. For this reason warm and cold events in the Niño-4 region are considered to represent ENSO variability. All the events classified as El Niño years using Niño-4 are also found to be consistent with the Niño-3.4 classification (http://www.cpc.ncep.noaa.gov/). Composites of precipitation over North America corresponding to cold and warm events in the Niño-4 region are also created. Warm (cold) events are identified as those in which the value of the Niño-4 index for DJF season has an anomaly greater (less) than 0.5°C.

A hydrograph for the Gila River is created using streamflow data to determine the magnitude and timing of the dual peaks (as carried out by Gutzler (2013)). Following identification of the peak months of streamflow, a cross-correlation with PRISM precipitation is performed to determine for which months the precipitation is best correlated to flow. Although in general streamflow

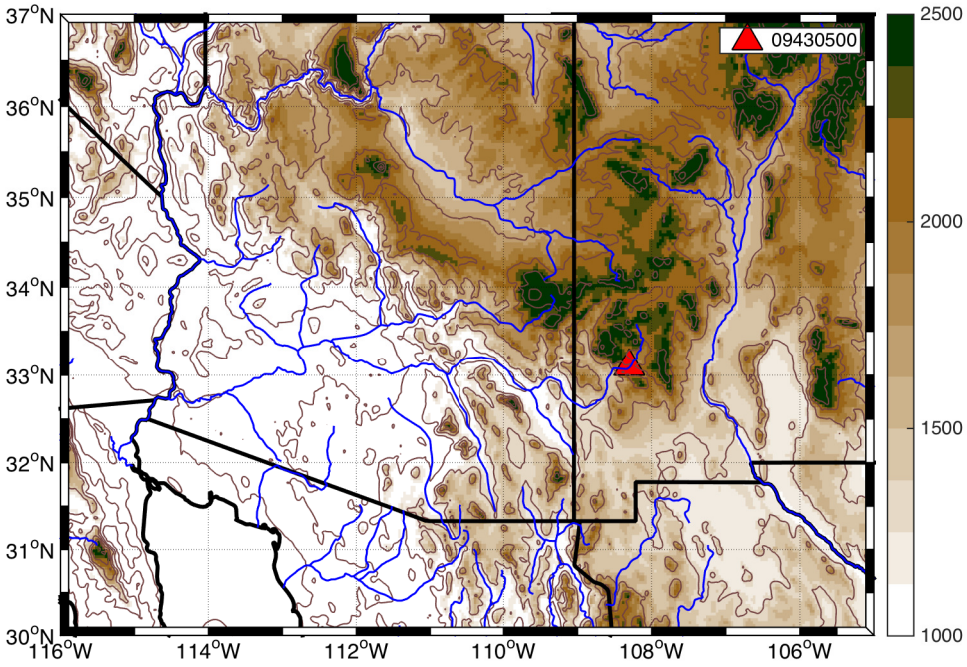

Figure 1: Map of the United States southwest and location of the Gila River. Red triangle indicates the location of USGS gage 09430500 located at 108°W and 33°N. Shading represents elevation (meters).

is expected to correlate with precipitation, other factors such as snowmelt, evaporation and soil moisture may impact the strength of correlations making the precipitation influence interesting to investigate (ie. (Notaro et al. 2010)). The timeseries of streamflow and precipitation for these months were then correlated with SST for 1928 to 2012 to create maps of correlation coefficients showing which ocean regions have the greatest influence on Gila River precipitation and flow.

High and low spring streamflow events are then investigated. High events are identified by determining years in which the magnitude of DJFMAM streamflow is greater than 85 percent of the annual mean, and low events when flow is less than 15 percent of the annual mean for 1928 to 2012. Composites of GPCC precipitation and SST patterns for the high and low events are created to examine co-existing patterns. GPCC data are used for precipitation in this case as they provide global coverage and can be used to illustrate patterns across the entire North American continent.

Decadal variability is investigated through analysis of the timeseries for 1928 to 2012. Composites for GPCC precipitation and SST are created for years of persistently high and low flow to determine the nature of the associated climatic patterns. In addition two dendroclimatological time series are analyzed to examine longer term variability in the region using the winter-spring and summer Standardized Precipitation Indices (SPI). Winter-spring SPI was reconstructed from tree-ring chronologies of earlywood width (EW) and summer SPI was reconstructed from tree-ring chronologies of latewood width (LW) that were adjusted to isolate the variability unique to LW (Griffin et al. 2011; Meko and Baisan 2001). Cross spectral and cross-wavelet coherence analyses indicates that the winter-spring and summer SPI reconstructions are effectively independent at interannual to decadal timescales, or more specifically, at wavelengths less than approximately 32 years. At longer timescales, the reconstructions are essentially coherent and in phase. A greater level of detail is provided in (Griffin et al. 2013). PDSI and SPI are also correlated to examine

consistency between the different data sets. Although both contain information on precipitation variability, the PDSI and SPI reconstructions do not share the same numerical input data. The SPI reconstruction was developed from novel measurements of tree-ring earlywood width at only a few sites, data that was not available nor included in the PDSI reconstructions. In contrast, the PDSI reconstruction is developed from a great many chronologies of total ring width. It is likely that data from some of the same trees entered into both reconstructions, but the data is from a different parameter (earlywood width (SPI) vs. total ring width (PDSI)).

1.3 Results

The box plot (Figure 2a) shows that peak streamflow occurs during the months December-January-February-March-April-May (DJFMAM) and the summer peak occurs during August-September (AS). For these months streamflow reaches monthly mean magnitudes of approximately 5.6 in winter-spring and 2.7 c.m.s. in summer. Figure 2 also shows timeseries of streamflow averaged over the water year (October to September) (Figure 2b), winter-spring (DJFMAM) (Figure 2c) and summer months (AS) (Figure 2d). The timeseries for water year flow (Figure 2b) indicate a high flow period from about 1975 to about 1990, and low flow from about 1945 to about 1960. In addition there is substantial interannual variability in monthly flow throughout the record. There is also a large degree of variability on an annual timescale shown in the box plot of Figure 2a. DJFMAM flow is greater than AS flow, comprising approximately 61 percent of the total mean annual flow compared to 15 percent over the time period 1928 to 2012. However, certain years exist where the AS flow exhibits sharp spikes which far exceed the DJFMAM flow, notably 1988 and 2006 in which AS flow accounts for 55 and 66 percent of the annual mean flow respectively

(Figure 3). The mean cumulative flow was found to be 140 million cubic meters per year, with a maximum mean flow rate of 13 c.m.s. (occurring in December), and a minimum mean flow rate of 1.2 c.m.s. (occurring in June).

As can be seen in Figure 2 the distributions of winter-spring and summer flow are positively skewed, and for this reason subsequent analysis is performed using log-transformed flow data. This improves the value of the correlations since the flow data does not vary linearly with precipitation and other variables (for example see (Gutzler 2013)). The timeseries for log-transformed DJFMAM and AS streamflow over the time period 1928 to 2012 were then cross-correlated (using Pearson correlation) with PRISM precipitation, first by month and then by season (Figure 4). For the monthly analysis, DJFMAM streamflow was found to correlate best with the concurrent winters precipitation, obtaining a maximum correlation coefficient in December of r = 0.70 ($p< 0.000$) (Figure 4a). The lag of flow behind precipitation is consistent with winter precipitation falling as snow and being stored in the basin until spring snowmelt. The seasonal correlation between DJFMAM log-transformed streamflow and winter average (NDJFMAM) precipitation is even higher with a value of r = 0.91 ($p< 0.000$). For monthly analysis of AS log-transformed streamflow, the highest correlation with precipitation is found for the preceding and coincident months of July-August-September (JAS) reaching a maximum value of r = 0.52 ($p< 0.000$) in August (Figure 5b). The seasonal correlation coefficient between JAS precipitation and AS log-transformed flow gave a value of r= 0.77 ($p <0.000$). The lack of any lag between precipitation and flow is because summer precipitation falls as rain with little storage in the basin. Timeseries for DJFMAM log-transformed flow with NDJFMAM PRISM precipitation and NDJF SST anomalies in the Niño 4 region for 1928 to 2012 show the coupling of winter-spring flow with both precipitation and Pacific Ocean SST anomalies (Figure 5a, b). A 7-year running average was applied to both time series (not

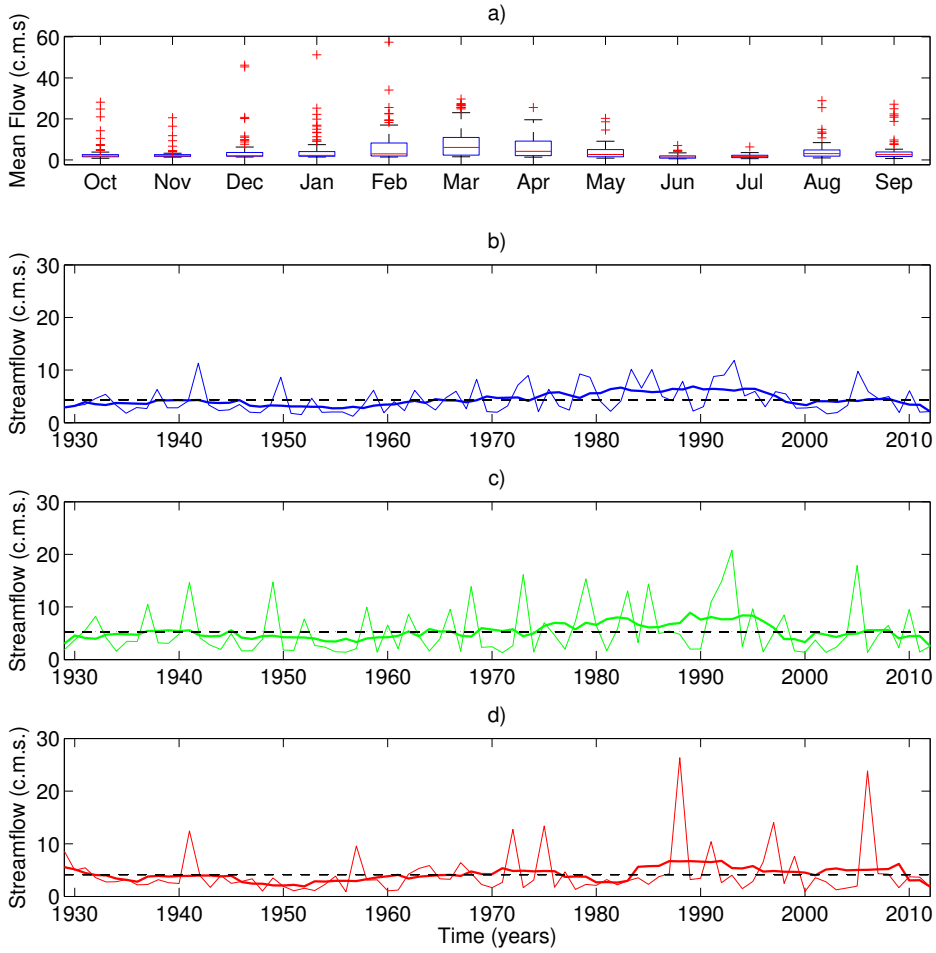

Figure 2: a) Boxplot of monthly flow over the time period 1928 to 2012. For each boxplot, the central mark is the median, the edges of the box are the 25th and 75th percentiles, the whiskers extend to the most extreme data points not considered outliers, and outliers are plotted individually. Timeseries of b) water year (October - September) averaged streamflow, c) December-January-February-March-April-May (DJFMAM) streamflow and d) August-September (AS) streamflow. The thick line shows the ten-year running average. The dashed black line indicates the mean for the time period.

shown) to investigate lower frequency Pacific SST impact on streamflow. This produces a positive correlation of r = 0.45 ($p < 0.000$) with explained variance of 20% (r^2=0.20). The relationship of decadal smoothed winter streamflow with the Pacific Decadal Oscillation index (not shown) also indicates a positive correlation between the two (r=0.59, $p < 0.00$). In addition, 35% of the variance is explained by the relationship between PDO and streamflow (r^2=0.35).

The weaker correspondence of AS log-transformed flow with JAS precipitation and Niño-4 SST anomalies is also demonstrated (Figure 5c, d). While the summer (AS) season correlation between Gila streamflow and basin precipitation is still quite high (r=0.52, $p < 0.000$), it is lower than in winter. To explain this the relationship of summer flow with evapotranspiration and temperature from the GLDAS CLM and VIC models and the NCEP-NCAR reanalysis averaged over the Gila River Basin (spanning 108.5W to 111.5W and 31.5N to 33.5N) was also investigated. Results from these studies (not shown) indicate weak correlations between AS summer flow and evaporation, temperature and precipitation - evaporation. Weak correlation is also found to exist between these variables amongst the different models and datasets which calls into question the validity of the evapotranspiration data. An additional analysis for the longer time period July-August-September-October-November as well as considering data for a smaller area corresponding to the watershed, were also performed to capture all basin storage but this did not improve the correlations.

PRISM precipitation for the Upper Gila Hydrological Unit in NDJFMAM as well as log-transformed DJFMAM streamflow is correlated with GPCC precipitation over North America (Figure 6a,b). The largest correlation coefficients (aside from the region directly over or adjacent to the Gila River basin) are found to occur across all of southwestern North America including the southern (values of approximately 0.5) and central Plains (also with a value of approximately 0.5). Negative correlation coefficients stretch inland from the Pacific Northwest. This pattern

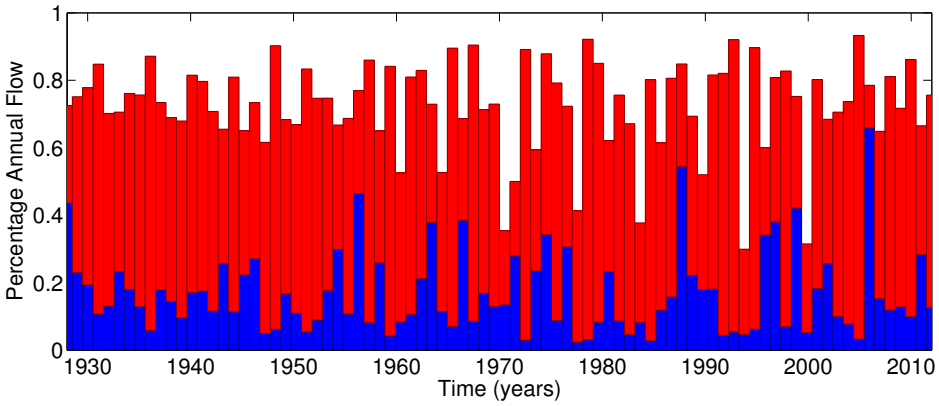

Figure 3: DJFMAM (red bars) and AS (blue bars) streamflow as a percentage of total annual water year mean flow for 1928 to 2012. Percentage values are stacked.

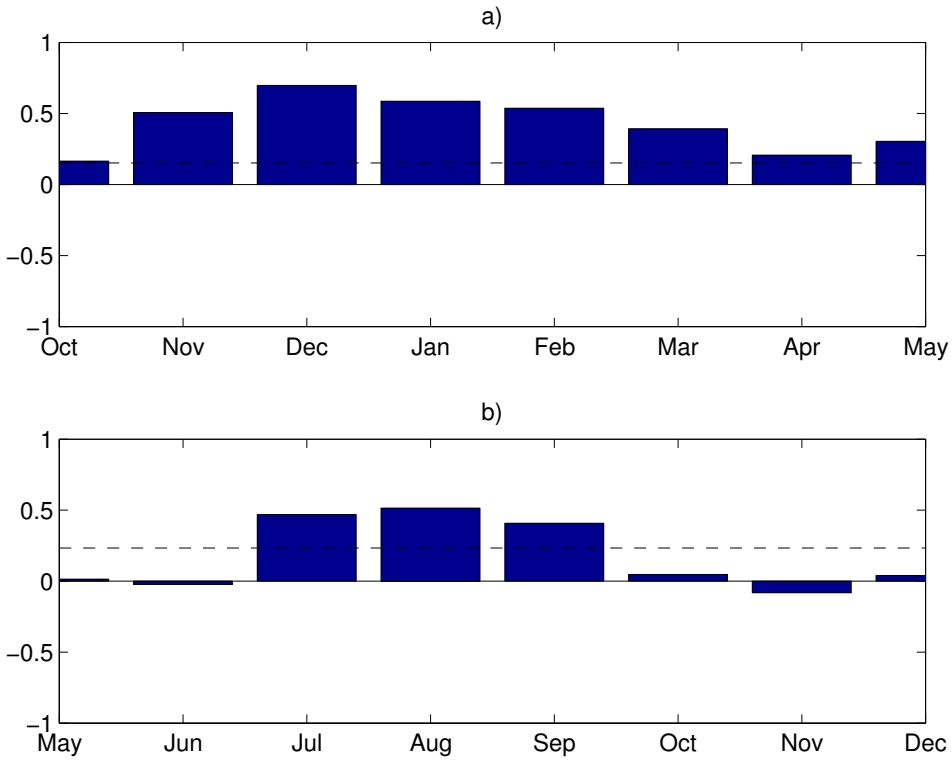

Figure 4: Cross-correlation for a) DJFMAM log-transformed streamflow and b) AS log-transformed streamflow with monthly PRISM precipitation for time period of 1928 to 2012. Dashed line indicates significant at 0.05 level.

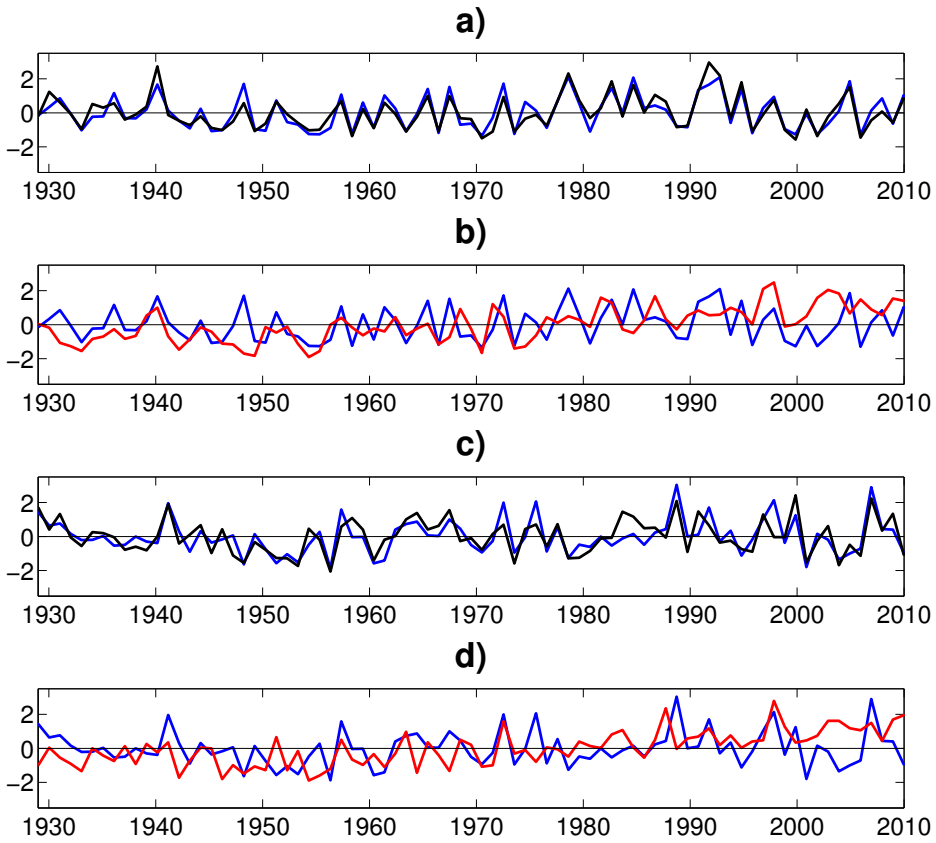

Figure 5: Timeseries of a) DJFMAM log-transformed streamflow and NDJFMAM PRISM precipitation, b) DJFMAM log-transformed streamflow and Niño-4 index for NDJF, c) AS log-transformed streamflow and JAS PRISM precipitation, and d) AS log-transformed streamflow and Niño-4 index for JAS. The data are averaged by year and standardized for time period of 1928 to 2012.

of positive and negative correlations is a typical ENSO pattern (Ropelewski and Halpert 1986, 1989, 1996). The JAS PRISM precipitation and the log-transformed AS streamflow is correlated with JAS GPCC precipitation over the region of Gila River watershed (Figure 6c,d). These maps demonstrate the localized nature of summer flow which is consistent with local-scale convective precipitation.

Streamflow during the peak months, and PRISM precipitation for the preceding NDJFMAM and JAS, were then correlated with global SST anomalies for JFM and JAS, respectively (Figure 7e, f). This is based on the assumption that there should be little lag between SST anomalies and the resulting atmospheric circulation anomalies that cause precipitation anomalies. The results show a positive correlation with SSTs in the ENSO region for DJFMAM streamflow and NDJFMAM precipitation with correlation coefficients reaching approximately 0.5. The greatest correlation coefficients appear to occur in the Niño-4 region. The SST correlation pattern extends from the west coast of South America to about the dateline, with cool waters to the north and south in the classic boomerang shape, all features typical of ENSO warm phase anomalies (Trenberth 1997). A similar southwestern North American precipitation response to tropical SST has been documented in previous studies (Wu et al. 2009; Dai 2013).

Composites of North American precipitation during NDJFMAM for years of warm and cold SST anomalies in the Niño-4 regions are shown in Figures 7a and b (years chosen to select events from 1979 to present to match availability of the ERA-Interim Reanalysis). In each composite, a total of 5 different years corresponding to both the warm (1983 ,1998, 2003, 2004, 2010) and cold (1981, 1984, 1985,1989, 2000) events are included. During anomalously warm years in the Niño-4 region, positive precipitation anomalies occur over southern North America and Mexico. Negative precipitation anomalies are found over the Southwest region corresponding to the Gila River basin

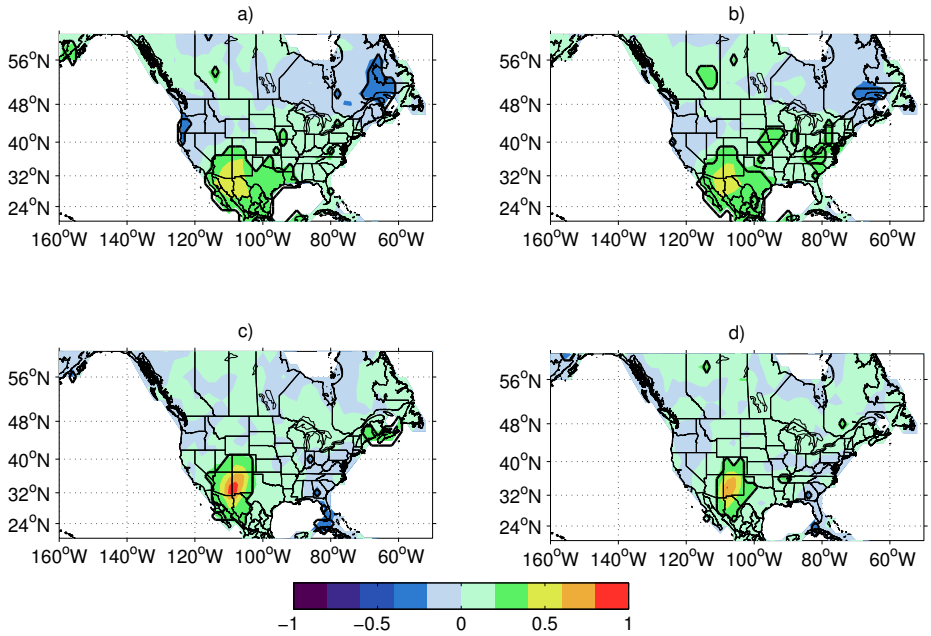

Figure 6: Correlation of North American GPCC precipitation for winter-spring (NDJFMAM) with a) PRISM NDJFMAM precipitation for the Upper Gila Hydrological Unit and b) log-transformed winter-spring (DJFMAM) streamflow and for summer (JAS) with c) PRISM JAS precipitation and d) log-transformed summer (AS) flow. Areas that are significant at $p<0.05$ lie within the black contour.

during anomalously cold years. ERA-Interim vertically integrated mean plus transient moisture transport and its convergence (Figures 7c, d) shows cyclonic flow over western North America and into the southwest during warm years (7c), and anticyclonic flow during cold years (7d).

Years of high streamflow are defined as years in which the streamflow value in DJFMAM flow is 85 percent or greater than the annual mean flow (4 events identified), or less than 15 percent for low flow years (3 events identified) over 1928 to 2012. Figure 8a illustrates a GPCC precipitation composite for the high streamflow years. This demonstrates negative precipitation anomalies over the West and East coast. Positive anomalies exist over the Plains region, the Gulf and over Mexico. This pattern of precipitation anomalies is similar to that expected during an ENSO warm phase (Ropelewski and Halpert 1986). A composite of JFM SST anomalies (Figure 8c) for these high streamflow years shows weak warm anomalies in the central tropical Pacific region. This resembles El Niño conditions but the pattern in the eastern tropical Pacific is not typically El Niño-like in that there are cool off-equatorial SST anomalies. The low streamflow years have below normal precipitation anomalies (Figure 8b) over southwest North America and above normal on the northwest coast of the United States. The SST anomalies for the low flow composite are La Niña like. It is noted that La Niña conditions exert a less strong influence on winter-spring streamflow. This is consistent with prior work that the connection between ENSO and southwest precipitation is nonlinear with El Niño exerting a stronger influence than La Niña as in Zhang et al. (Zhang et al. 2014) and references therein.

Decadal variability is investigated in Figures 9, with years of high streamflow taken as 1977 to 1997 (after the 1977 climatic shift in the Pacific) (Figure 9b,e), and low streamflow as 1945 to 1960 (Figure 9a,d). These different time periods for high and low flow are selected based on analysis of the 10-year running mean of the timeseries for Gila River streamflow from 1928 to 2012

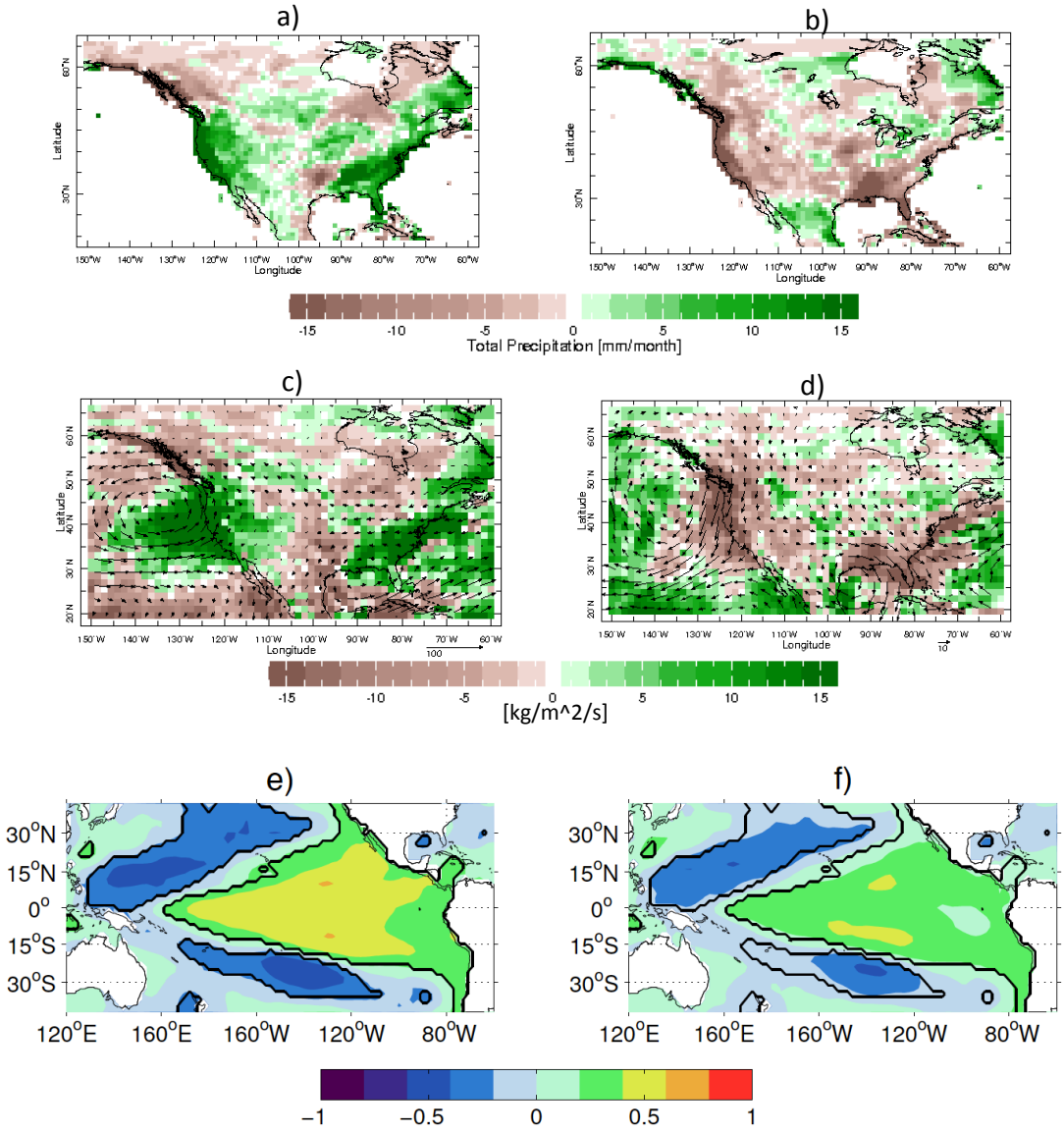

Figure 7: Composites for North American NDJFMAM GPCC precipitation (mm/month) for a) anomalously warm years (1983 ,1998, 2003, 2004, 2010) and b) anomalously cold years (1981, 1984, 1985,1989, 2000) in the Nino-4 region (150°W to 160°E and 5°N to 5°S). Warm (cold) years identified by years in which value of the Nino-4 index for the DJF season has an anomaly greater (less) than one standard deviation above the 1979 - 2012 mean. We focus on this shorter period in order to match the temporal availability of the ERA-Interim Reanalysis. ERA-Interim vertically integrated mean plus transient moisture transport (vectors) and its convergence (colors) for NDJFMAM in c) anomalously warm years and d) anomalously cold years as identified above. Correlation of e) NDJFMAM PRISM precipitation over Gila River basin with DJFMAM SST and f) DJFMAM streamflow with DJFMAM SST. Areas that are significant at $p<0.05$ lie within the black contour.

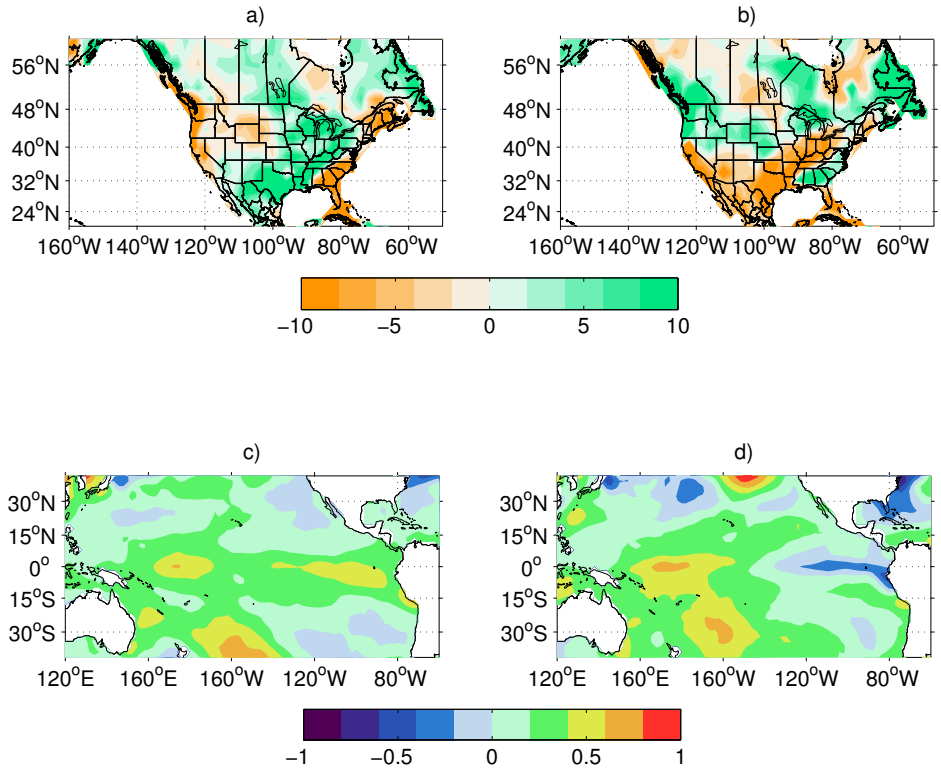

Figure 8: Climate composites for periods of high and low streamflow, defined as high flow for years in which DJFMAM streamflow is greater than 85 percent of the annual flow, and low flows when 15 percent or less for 1928 to 2012. High streamflow composite for a) NDJFMAM GPCC precipitation anomaly and c) DJFMAM SST anomaly, and low streamflow composite for b) NDJFMAM GPCC precipitation anomaly and d) DJFMAM SST anomaly.

in Figure 2b - d. Decadal trends are particularly apparent in the annual average for streamflow shown in Figure 2b, with a mean value of 6 c.m.s. occurring for the years 1977 to 1997 and 3 c.m.s. for the low flow years of 1945 to 1960. The most recent period, 1999 to 2012, is also investigated (Figure 9c,f). During the high streamflow period (Figures 9a,d) positive precipitation anomalies are observed over southwestern North America and the Gulf Region. This pattern again resembles the El Niño related precipitation anomaly pattern over North America. Consistently, positive SST anomalies occur in the central and eastern Pacific within a meridionally broad pattern resembling decadal El Niño variability (Zhang et al. 2012). A region of negative SST anomalies is also found to occur in the North Atlantic region. For the low streamflow years (Figures 9b,e) negative precipitation anomalies occur over southwest North America, the coastal southeast U.S. and the Gulf region. Positive anomalies occur over the northwest and much of the eastern U.S. However the SST anomalies in the Pacific and Atlantic Oceans do not clearly show any climate mode pattern. The most recent decade (Figure 9c,f) shows positive precipitation anomalies over the north west United States, and negative anomalies over the south west and Gulf Region. Pacific Ocean SST has generally warm anomalies in the tropics but cold anomalies in the central Pacific. Consistently it has been shown using SST-forced atmosphere models how a shift in the late 1990s to this SST pattern induced drying across southwest North America (Hoerling et al. 2009; Seager and Vecchi 2010b).

The Upper Gila Watershed is surrounded by a dense network of moisture sensitive tree-ring chronologies that offer a high-quality and long-term perspective on moisture variability in the centuries prior to the instrumental era. The June-August PDSI reconstruction from the North American Drought Atlas (Cook et al. 2010); Figure 10b) illustrates that in the Upper Gila Basin, persistent pluvials centered on the 1910s and 1980s, made the 20th Century perhaps the wettest

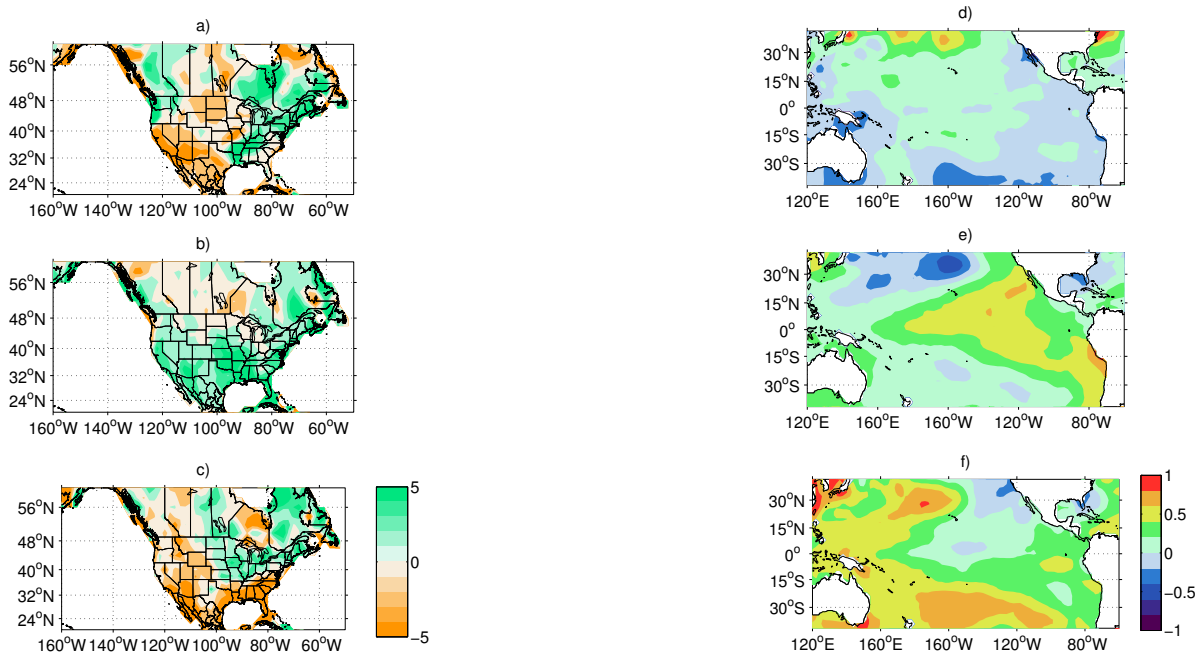

Figure 9: Composite for North American GPCC precipitation during a) 1945-60 period of generally lower flows, b) 1977-97 period of generally higher flows and c) for the most recent decade 1999 to 2012 for NDJFMAM. Composites for SST anomalies during d) 1945-60 period of generally lower flows, e) 1977-97 period of generally higher flows and f) for the most recent decade 1999 to 2012 for DJFMAM over the Pacific.

of the last millenium. It also highlights protracted drought events previously described in the late 16th century (e.g. (Stahle et al. 2009)) , and several ”megadroughts” of the late Medieval Era (e.g., (Meko et al. 2007; Cook et al. 2007; Williams et al. 2013)). The anomalously wet 20th century, 16th century ”megadrought,” and another multidecadal drought event in the early 1400s are also evident in an unpublished reconstruction of water year flow on the Gila River downstream at Safford Arizona, which covers the period 1332-2005 A.D. [Meko and Hirschboeck, http://treeflow.info/loco/gila.html].

A novel perspective on paleomonsoon precipitation variability in this region is available from summer-forming tree-ring ”latewood” (Griffin et al. 2011). Latewood chronologies have been used to reconstruct June-August standardized precipitation indices for a large area of Arizona and western New Mexico (Griffin et al. 2013). In the Southwestern U.S., precipitation influence on the summer PDSI is dominated by the cool season (St. George et al. 2010) and for data in the present study, the relationship between summer PDSI with previous NDJFMAM PRISM precipitation ($r=0.42, p<0.000$) is greater than that with the monsoon (JAS) precipitation (not significant). The summer PDSI is also found to correlate greater with the winter-spring SPI index over 1530 to 2003 ($r = 0.47$, $p<0.000$) than with the summer SPI (not significant). The SPI demonstrates synchronous periods of negative SPI index between the winter-spring (October-April) and summer around 1575, 1675, 1775, 1825, 1880, and 1950 among other periods (although in general the correlation between the two is insignificant). This supports recent Southwestern studies using latewood which find that major decadal droughts of the last several centuries were likely characterized by precipitation deficits during both seasons (Stahle et al. 2009; Faulstich et al. 2013; Woodhouse et al. 2013; Griffin et al. 2013).

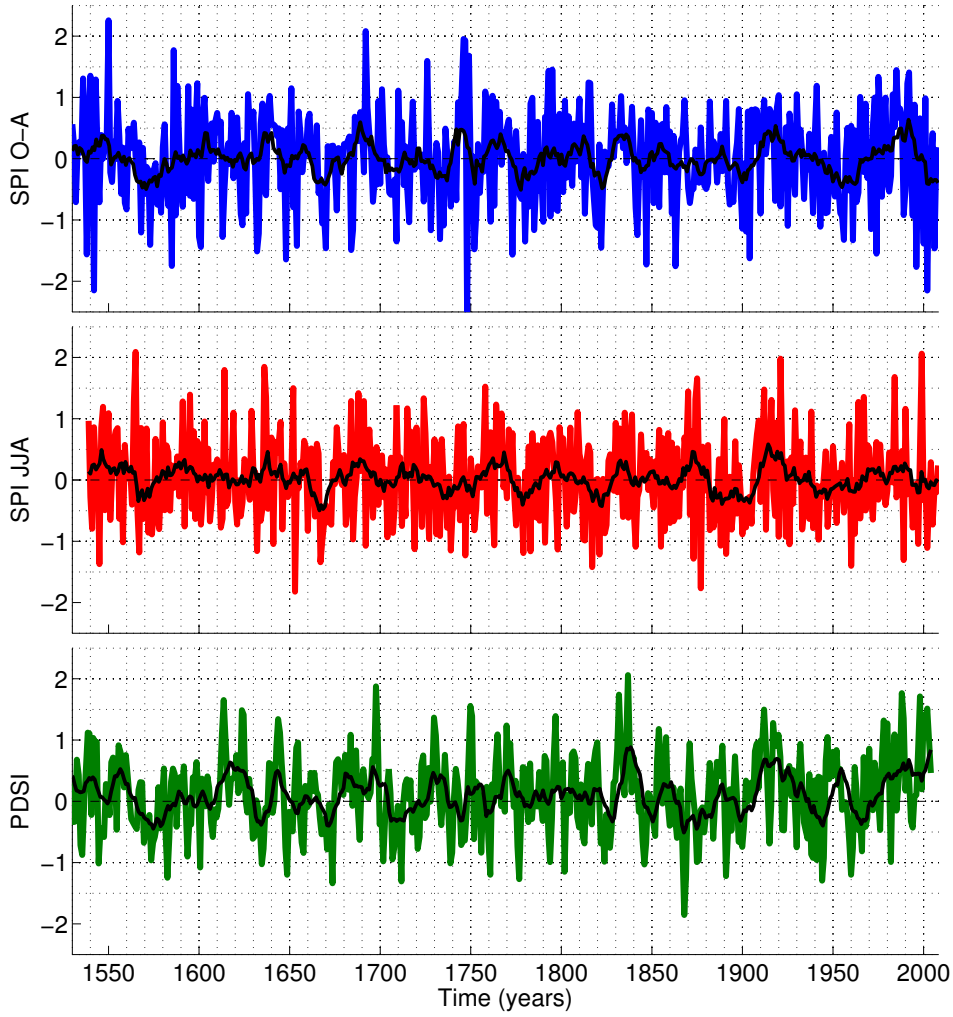

Figure 10: Top time series : reconstructed Standardized Precipitation Index (SPI) (blue line) for 7-months from October to April for 1530 to 2008. Middle time series: Reconstructed SPI (red line) for 2-months from July to August for 1539 to 2008. Bottom time series: Reconstructed PDSI from treering data (green line) from 1530 to 2003. The data are derived from the region of the Gila River drainage basin. The original annual data are smoothed using a moving average over a ten year interval.

1.4 Conclusion

We have presented the first comprehensive analysis of the climatic causes of Gila River flow variability over the time period 1928 to 2012. The Gila River experiences two peaks in its hydrograph: one in the winter to spring (DJFMAM) with a monthly mean magnitude of approximately 5.6 c.m.s, and a second, smaller, peak (about 2.7 c.m.s) in the summer (AS) coinciding with the North American Monsoon The DJFMAM streamflow peak correlates the greatest with precipitation in the preceding NDJFMAM months, with the delay being consistent with winter precipitation falling as snow in the headwaters and moving into the river in spring following snowmelt. The AS streamflow peak correlates the greatest, but at a lower value, with JAS precipitation, the lack of any appreciable lag being consistent with Monsoon precipitation falling as rain and moving quickly into the river. Correlation and composite analyses show that DJFMAM streamflow and NDJFMAM precipitation are positively related to an ENSO like pattern of Pacific SST anomalies. These relations hold in general for individual year examples of high and low spring flows.

In contrast, AS streamflow and precipitation do not have associations to Pacific SST. The weaker link between AS streamflow and summer precipitation, and between summer precipitation and SST anomalies, indicates future studies are needed focused on North American Monsoon variability and the role of other controls on streamflow such as temperature and evapotranspiration variability. Southwest precipitation during the early summer has been found to be influenced in part by tropical Pacific SST, however the later NAM precipitation variability remains largely unaffected by tropical forcing (Grantz et al. 2007). Moisture during the NAM is also derived from a number of different sources including the Gulf of Mexico, the Gulf of California, the Pacific, as well as the land (Jana et al. 2018), and identification of the moisture pathway influencing the

NAM will have important implications for explaining summer streamflow. In addition the Gila River basin is affected by highly localized climate variability involving the monsoon and convective storms, particularly during the summer months, which may be difficult to quantify with sparse rain gauges.

The Gila River flow also has impressive variability on decadal timescales. This can be explained in large part by decadal ENSO-like variability with the composite for the high flow decades of 1975 to 1990 clearly revealing the warm phase of Pacific decadal variability. The post 1990s decline in Gila River flow is also explained in terms of the shift to cooler tropical Pacific SSTs. The reconstructed PDSI and SPI indexes for past centuries demonstrate prolonged droughts and pluvials as well as periods of synchronous summer and winter dry periods.

The history of the spring maxima of Gila River flow can therefore be largely explained in terms of natural precipitation variability forced by interannual to decadal ENSO variability. This should allow some useful seasonal to interannual predictabilty of spring Gila River flows. The high flows in the late 20th Century are associated with the warm phase of Pacific decadal variability and the recent downturn in the 21st Century is consistent with the more generally cold tropical Pacific conditions since the 1997/98 El Niño. As the current century evolves, Gila River flow will no doubt be influenced by human-induced climate change but natural variability such as that identified here will also continue. Projections of future Gila River flows, and its important contribution to southwest water resources, will need to account both for the natural variability and the response to human-induced climate change.

2 Covariability of climate and streamflow in the Upper Rio Grande from interannual to interdecadal timescales

2.1 Introduction

At 3,051 km in length, and with a drainage area of approximately 472,000 km^2, the Rio Grande is the fourth longest river in North America. It provides water to 5 million people for agricultural, municipal and industrial purposes in the U.S. states of Colorado, New Mexico, and Texas, and in Mexico (Woodhouse et al. 2012) (Figure 11). The majority of the flow in the river above its confluence with the Rio Conchos near Presidio, Texas, originates as snowmelt runoff from the mountains in southeastern Colorado and northern New Mexico (Lee et al. 2004; Khedun et al. 2010; Woodhouse et al. 2012) (collectively, the Upper Rio Grande (URG), with a drainage area of approximately 43,000 km^2 (Lee et al. 2004)). Sixty to sixty-five percent of inflows originate in the headwaters region, consisting of the southern Rocky Mountains and San Luis Valley of southwestern Colorado; flows along the Rio Chama and the Jemez River collectively account for another 25 percent of native inflows to the URG, with the remaining inflows coming from minor tributaries (Llewellyn and Vaddey 2013). The majority of the 5 million water users are located south of the Jemez River confluence in the Middle Rio Grande (from the Jemez River to the El Paso Valley). High interannual variability in streamflow poses significant challenges for water supply and flood risk management. Improved understanding of the climate controls on Rio Grande flow variability is essential to improve management of water resources.

Studies have shown that precipitation and streamflow in the Southwestern United States (SWUS) in general are affected by a range of diverse drivers, including the El Niño-Southern Oscillation

(ENSO), the Pacific Decadal Oscillation (PDO) and the Atlantic Multidecadal Oscillation (AMO), as well as the North American Monsoon (NAM). However, the failure of recent El Niño events to generate correspondingly large spring runoff volumes suggests that these relationships are not straightforward. This paper reassesses the impacts of ENSO, PDO, and AMO on streamflow in the Rio Grande basin above Albuquerque, New Mexico, and shows that these teleconnections are an incomplete explanation of the variance in flows.

On interannual timescales, ENSO produces above normal precipitation and streamflow for the SWUS when it is in its warm phase (El Niño) (Kahya and Dracup 1993, 1994). On interannual timescales El Niño has also been found to be associated with above-normal precipitation and streamflow anomalies in the URG basin (Lee et al. 2004; Khedun et al. 2010). The PDO has also been found to produce above normal northern hemisphere winter (December-January-February (DJF)) precipitation and streamflow during its positive phase (Barlow et al. 2001; Cayan et al. 1999; Khedun et al. 2010; Pascolini-Campbell et al. 2015; Guan et al. 2005). The cold (warm) AMO produces positive (negative) streamflow and precipitation anomalies in the SWUS (Enfield et al. 2001; Thomas 2007; Nowak et al. 2012).This relationship is strengthened with a concurrent positive PDO phase (McCabe et al. 2004). The NAM brings a northern hemisphere summer (July-August-September (JAS)) peak in rainfall (Adams and Comrie 1997; Barlow et al. 1998) and NAM variability drives streamflow variability (Pascolini-Campbell et al. 2015). As this paper focuses on flows resulting from snowmelt runoff, the effects of the NAM on late summer flows is not considered further. ENSO, PDO and AMO have also been found to modulate streamflow in other river basins around the world (Ward et al. 2016; Córdoba-Machado et al. 2016; Kiem and Franks 2004).

Streamflow predictability is also influenced by land surfaces processes via the interaction of precipitation, evapotranspiration, snowmelt, soil moisture and vegetation (Koster et al. 2010; Mau-

rer and Lettenmaier 2003). Infiltration into soils, evapotranspiration and canopy water storage can all contribute to reducing runoff of water to streams. Water storage in snowpack and its melt also will impact the timing and magnitude of water delivery to the rivers. Variability of these different processes will influence streamflow timing (Hamlet et al. 2007). Therefore, despite the observed teleconnection between precipitation and SST, the influence of SST on streamflow is modulated by a variety of complex land surface processes.

The purpose of this study is to re-evaluate the climatic drivers which produce the observed mean seasonal cycle of URG streamflow, and mean flow variability on interannual to decadal timescales. Second, we will investigate the drivers of the highest mean monthly northern hemisphere spring-summer (April to September) streamflow anomalies. This study extends previous research on the URG through consideration of the combined role of the Pacific and Atlantic, a longer period of study extending from 1920 to 2016, interannual and decadal variability, and both mean flow and high flow variability. In addition, sea surface temperatures do not account for all streamflow variability. Therefore, the present study will also consider the atmospheric configurations that correspond to streamflow anomalies that can occur across a range of SST states.

Using URG stream gage data, observed precipitation, observed sea surface temperature and atmospheric Reanalysis, this study aims to provide a more complete understanding of URG streamflow variability over the past several decades. The following questions are investigated:

- What climatic drivers produce the observed seasonal cycle of URG flow?
- Which configurations of Pacific and Atlantic SST drive flow variability on timescales of years to decades for the URG and how strong are these relations?

This investigation will advance understanding of the climatic drivers of URG flow variability,

and of extreme high and low flows to the benefit of water management activities. In particular, it will be shown that prior work has overstated the role of sea surface temperature anomalies in driving URG flow variability.

2.2 Data and Methods

To analyze the natural drivers of Rio Grande streamflow at its headwaters, we use seven United States Geological Survey gages (USGS) on tributaries in New Mexico (Figure 11). Tributaries are selected because all stream gages on the Rio Grande main stem are affected by regulation and water withdrawals. Instead, we analyze data from the following unmodified New Mexico tributaries (arranged from northernmost to southernmost): Rio Chama near La Puente (USGS 08284100), Santistevan Creek near Costilla (USGS 08253500), Rio Hondo near Valdez (USGS 08267500), Rio Lucero near Arroyo Seco (USGS 08271000), Rio Pueblo de Taos near Taos (USGS 08269000), Rio Ojo Caliente near Madera (USGS 08289000) and Jemez River near Jemez (USGS 08324000). We use mean monthly streamflow data for these sites to examine flow. We compare the streamflows of these rivers to the naturalized flow record for two gages lying on the main Rio Grande stem itself (Rio Grande near Del Norte, CO, (USGS 08220000), and Rio Grande at Otowi Bridge, New Mexico, (USGS 08313000)) (time period available shown in Table 1). These gages are located in the upper reaches of the Rio Grande in an area characterized by mountainous terrain with peaks exceeding 3500 m.These stream gages drain areas as small as 6 km^2(Santistaven) up to 37,036 km^2 (Otowi) (compared to a drainage area of 43,000 km^2 for the URG (Lee et al. 2004)). We find high correlation (ranging from r = 0.69 to r = 0.84 with Del Norte, and r = 0.79 to r = 0.92 for Otowi) between the Rio Grande gages and the tributary flows, thus allowing the tributaries to serve

as suitable indicators of the natural flow variability (Table 1, last column).

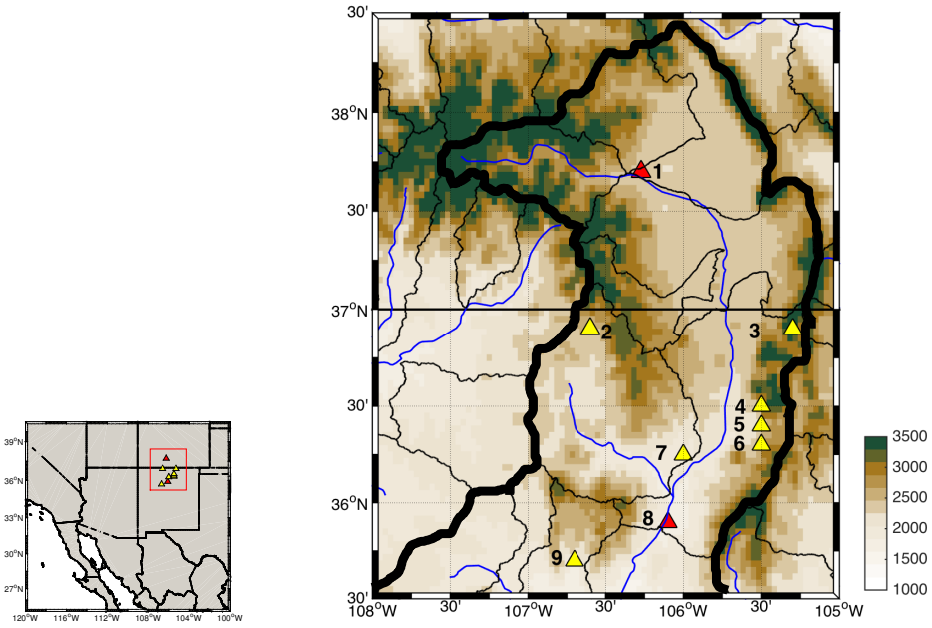

Figure 11: Map showing elevation (meters), delineation of upper Rio Grande basin (thick black line), and location of USGS stream gages used in this study: 1) Del Norte, 2) Rio Chama, 3) Santistaven creek, 4) Rio Hondo, 5) Rio Lucero, 6) Rio Pueblo de Taos near Taos, 7) Rio Ojo, 8) Otowi, 9) Jemez river. Red marker indicates stream gage is located on main stem, yellow marker indicates stream gage is located on a tributary. Inset above shows location of upper Rio Grande region.

Table 1: Summary of USGS station data

Gage Name	Gage Number	Temporal Availability (monthly statistics)	Drainage Area (sq km)	Elevation (m above NGVD29)	Correlation: Del Norte (Otowi) (r-value)
Del Norte	08220000	1908 - 2015	3419	2432	1.00 (0.84)
Rio Chama	08284100	1955 - 2014	1243	2158	0.84 (0.92)
Santistaven	08253500	1937 - 2014	6	2901	0.75 (0.79)
Hondo	08267500	1934 - 2015	94	2331	0.69 (0.86)
Lucero	08271000	1913 - 2014	43	2453	0.72 (0.84)
Pueblo	08269000	1913 - 2014	173	2249	0.69 (0.87)
Ojo	08289000	1932 - 2016	1085	1937	0.75 (0.91)
Otowi	08313000	1919 - 2016	37036	1672	0.84 (1.00)
Jemez	08324000	1936 - 2016	1217	1713	0.71 (0.81)

Seasons discussed in the paper refer to the northern hemisphere. The area receives precipitation as snow during winter months, which melts in the spring and summer. Rainfall is greatest in the summer months when the area is affected by local-scale convective activity. Analysis will cover the period of the full flow records (see Table 1). We use Pearson's correlation throughout to assess the strength of the relationships between variables. Given the positive-skew of streamflow, we use the log-value of streamflow when carrying out the correlations between streamflow.

The precipitation dataset we use is from the Parameter Regression on Independent Slopes Model (PRISM; in units of mm/month on a 4km grid), which uses a well-verified, terrain-sensitive algorithm to interpolate between available stations over the period 1895-present (Daly et al. 2008a). We average precipitation over the catchment area of each of the stream gages to investigate local variability. We acknowledge the limitations of using gridded precipitation data, which has been found to underestimate extremely high rainfall events, which could implicate our understanding of high monthly streamflow events (King et al. 2013). Gridded precipitation data is also less reliable at higher elevations, which is an additional caveat given the high altitude of the drainage gages used in this study (see Table 1) (Tozer et al. 2012). SNOTEL data is used for snow water equivalence (SWE) from sites lying in proximity to the stream gages used (information in Table 2). We use four different SNOTEL sites which correspond to the location of gages used: Upper Rio Grande (corresponding to Del Norte, Rio Chama and Santistaven), Red River Pass 2 (Hondo, Lucero and Pueblo), and the average of Palo and Elk Cabin (Ojo, Otowi and Jemez). For SST, we use ERSST V4 reanalysis data (in units of degrees Celsius on a 2°x 2° global grid) (Smith et al. 2008). We use ERA Interim data for vertically integrated moisture flux (mean and transient) to analyze the atmospheric moisture delivery patterns (1.5°x1.5° global grid) (1979 - 2014) (Dee et al. 2011). We also use ERA Interim precipitation data for comparison to the moisture flux.

Table 2: Summary of SNOTEL station data

Station Name	Station Number	Temporal Availability (monthly statistics)	Elevation (m)
Upper Rio Grande	839	1986 - 2015	2865
Red River Pass 2	715	1978 - 2015	3002
Palo	1170	2010- 2015	2849
Elk Cabin	921	1996 - 2015	2502

We use the following SST indices created from ERSST V4: NINO3.4 (SST in the Pacific area-averaged over 5S - 5N, and 170W - 120W), Pacific Decadal Oscillation (PDO) index (the leading principal component of monthly SST anomalies in the North Pacific Ocean north of 20N) (Zhang et al. 1997), and the Tropical North Atlantic (TNA) index (average anomaly of monthly SST averaged over 5.5N to 23.5N and 15W to 57.5W) to represent AMO (Enfield et al. 2001). We use the TNA due to its high correlation with the AMO, and also due to the fact Atlantic impacts on SWUS climate originate largely from the tropics (Kushnir et al. 2010).

2.3 Results

2.3.1 Climatology and variability of URG streamflow, precipitation and temperature

The water year (October - September) mean streamflow for the tributaries Rio Chama, Santistaven, Hondo, Lucero, Pueblo, Ojo and Jemez stream gages is highly correlated with those of Del Norte and Otowi on the main stem of the Rio Grande (Table 1, last column). The timing of the peak flow is also fairly consistent between the main stem and the tributaries, with highest flows occurring in April-May-June-July (AMJJ) (Figure 12). Gages further north in the basin (Del Norte, Rio Chama, Santistaven, hereafter referred to as 'northern gages') have peak flows occurring more in May-June-July, whereas gages more south in the basin (Ojo, Otowi and Jemez,

hereafter 'southern gages') have peak flows occuring earlier in April-May-June. Middle gages (Hondo, Lucero, Pueblo, hereafter 'middle gages') tend to peak in May-June. This is consistent with above-freezing temperatures and snowmelt occurring earlier further south in the basin, contributing to earlier spring-summer flows (see Figure 13 below). The similar timing in streamflow is expected given the proximity of these stream gages, as well as their comparable elevations in the basin (Table 1). The hydrographs (Figure 12) also illustrate the positive skew of the data: many of the highest flows exceed 1.5 times the interquartile range of the data (as demonstrated by the outliers denoted by a red cross).

We investigate the seasonal cycles of precipitation and SWE using PRISM data averaged over the drainage area of the stream gage and SNOTEL gages located at proximity to the gages respectively (Figure 13). Precipitation over the northern gages displays a bimodal peak: the first occurring in February-March-April (reaching a maximum of 75 mm/month for Rio Chama), and the second in July-August-September (reaching a maximum of approximately 75 mm/month for Rio Chama, Santistaven and Lucero). The southern gages have a more pronounced summer precipitation maximum (June-July-August) indicative of the monsoon influence. For the northern gages, SWE peaks in March whereas for the southern gages the SWE peaks earlier in February. The earlier decline in SWE in the southern gages is mirrored in the earlier peak streamflow (Figure 12).

Interannual variability in AMJJ streamflow is broadly synchronous among gages. Figure 14 (top panel) shows the timeseries of both high pass and low pass AMJJ streamflow using a cut off frequency of seven years (see below for details of the filter). Similar timing in anomalously high annual flows is observed to occur between the different gages, such as the high flow peaks in 1985, 1995 and 2005. Magnitudes are far smaller for the tributaries which drain much smaller basins in the system such as Hondo, Lucero and Pueblo (see Table 1 for drainage area). The AMJJ

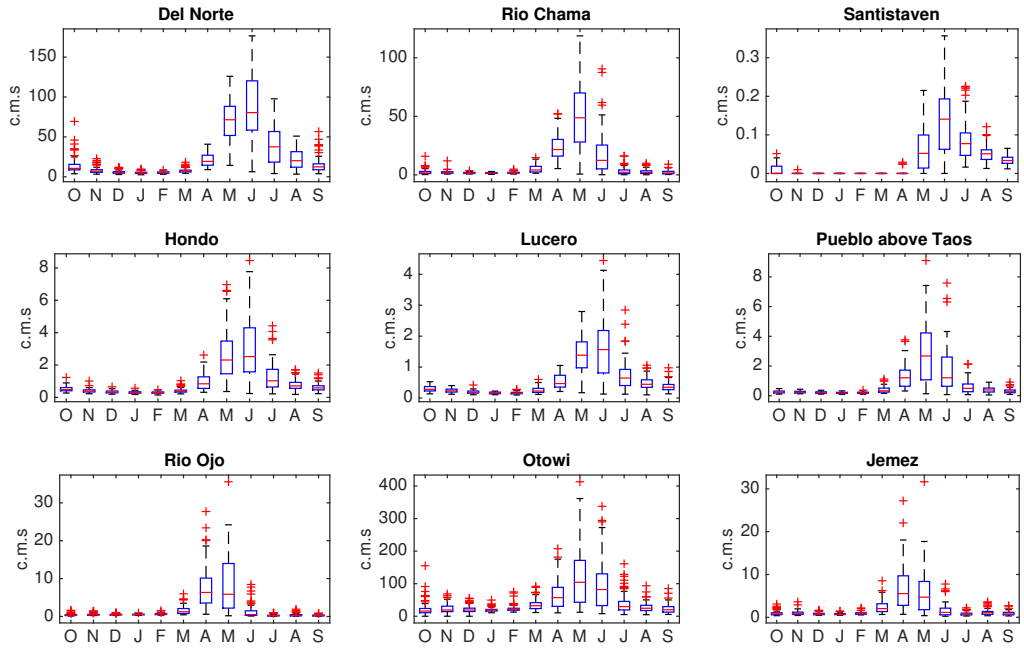

Figure 12: Boxplots of monthly streamflow (c.m.s.) over length of record for each stream gage. For each boxplot, the central mark is the median, the edges of the box are the 25th and 75th percentiles, the whiskers extend to the most extreme data points not considered outliers, and outliers are plotted as crosses.

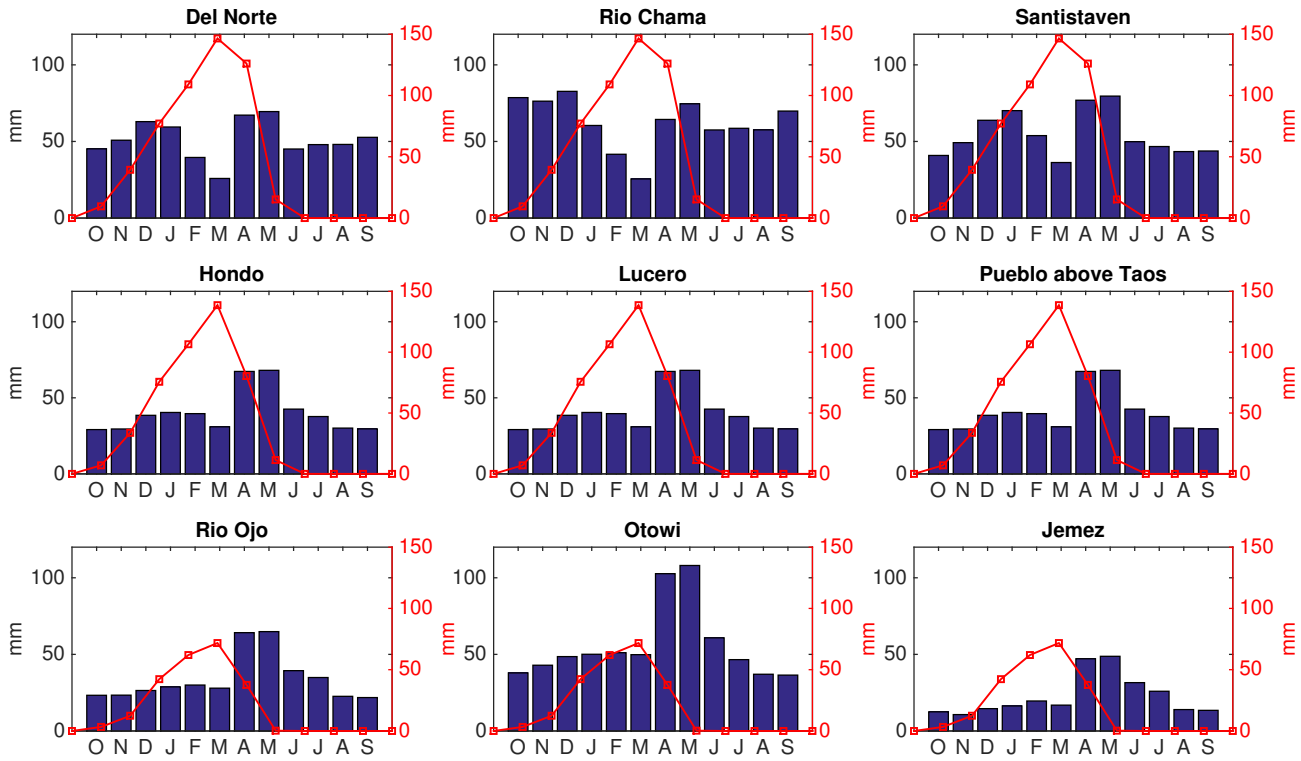

Figure 13: Seasonal cycle of PRISM precipitation area averaged over each gage (bars) (mm/month) and snow water equivalent SNOTEL gage data (red lines) (mm/month).

timeseries in Figure 14 also contain a similar pattern of low frequency high flow centered around 1985 and declining flow from 1996 to present. In the longer streamflow timeseries (for Del Norte) this low frequency variability is seen to also produce above normal flow in the early century (1900-1920) and lower flow between 1945 to 1975. The PRISM timeseries of average annual water year precipitation in the contributing watershed above the stream gages for the period 1895 to 2014 (Figure 14 (bottom graphs)) shows corresponding wetter than average conditions in the early 20th century (1900 - 1920) followed by a decline in the mid-century to drier than average conditions (from approximately 1945 to 1975). The precipitation decadal mean then increases again from the 1980s to around 2000 after which it again tends to decline.

2.3.2 Relation of peak flow variability to antecedent precipitation and ocean states

AMJJ streamflow is influenced by precipitation during the preceding fall to spring (October to May). Since the main Pacific SST teleconnection season is during the DJF and MAM seasons, for the rest of this section we focus on the season December to May. To understand how December to May precipitation influences streamflow, we analyze the relationship among key drivers of precipitation variability (ENSO, PDO, TNA) and streamflow in the URG using both high and low pass filtered streamflow and SST data (Figures 5 - 6). The high (low) pass filter attenuates frequencies below (above) seven years to only capture high (low) frequency variability. We filter frequencies above and below seven years since this period approximately divides interannual ENSO from decadal PDO while the AMO only occurs on the longer timescale. ENSO variability occurs on a timescale of 3 to 7 years (Trenberth et al. 1998). We follow the methods of Zhang et al. (Zhang et al. 1997) who filtered SST using high and low pass filters with a cut off of 6 years to separate interannual from interdecadal variability. In our case, we select 7 years to represent the

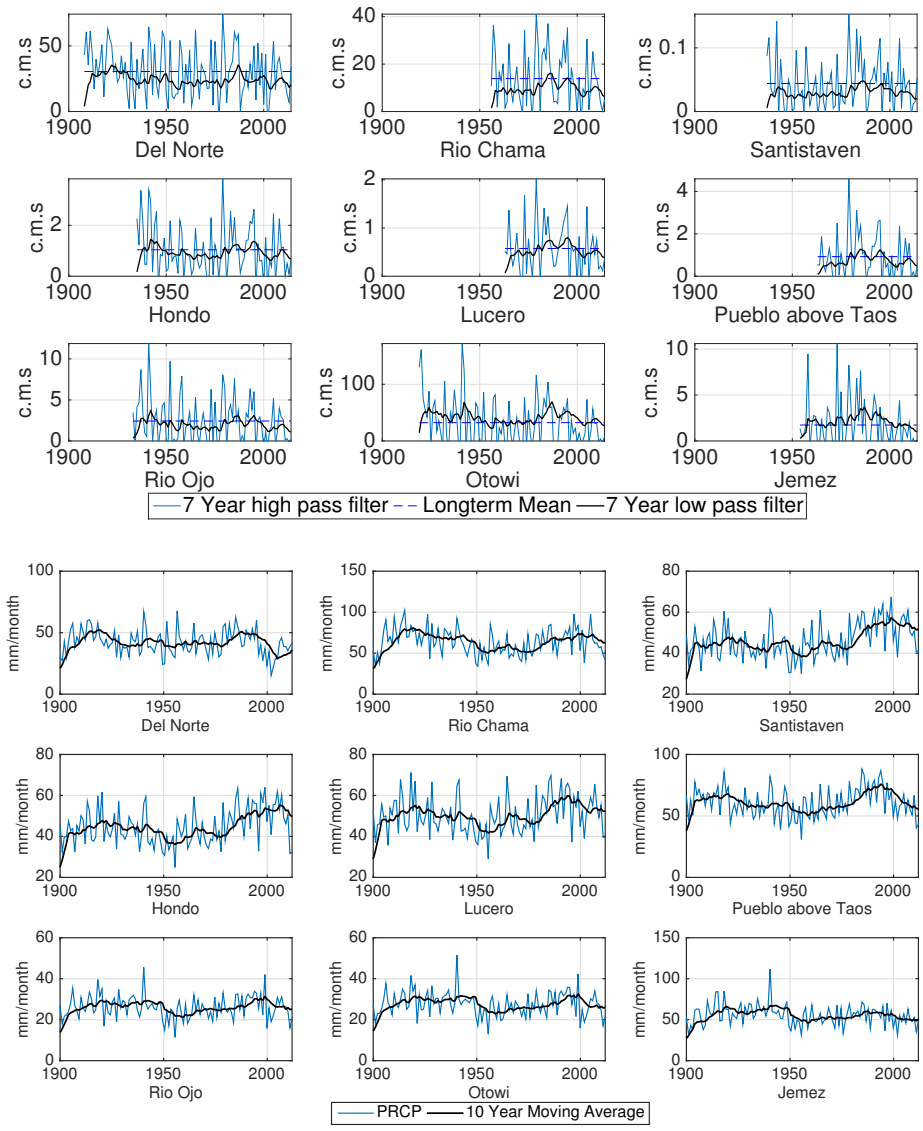

Figure 14: Top: Streamflow timeseries for high pass (blue line) and low pass (black line) filtered AMJJ for each stream (c.m.s.) using a cutoff frequency of 7 years. Blue-dashed line is long term mean for high pass filtered throughstreamflow. Bottom: PRISM precipitation timeseries for annually averaged water year (October to September) (blue line) (mm/month) and 10 year moving average (black line) area-averaged over the catchment of each stream gage.

upper range of ENSO variability. We performed the analysis using cut off filters for different years (6, 7, 8, 10) and found there to be no significant difference in the results for the different cut off years for the low and high pass filters with slight alteration of the cut off period.

The filter we use is the Butterworth filter. We use effective sample size for significance testing in order to account for the issue of autocorrelation arising from the smoothed data series. We are aware of the potential limitations of assuming linearity between SST and streamflow as has been noted in prior work (Córdoba-Machado et al. 2016; Kiem et al. 2003). Hence, we performed composite analyses of SST corresponding to high and low streamflow years for each gage, and these confirmed a predominantly linear relationship between SST and AMJJ streamflow. We therefore have confidence in using the linear correlations between SST and streamflow to investigate this relationship.

In the high pass filtered correlations, AMJJ streamflow is weakly positively correlated with Pacific SSTs in both DJF and MAM (Figure 15). The expected negative correlation between AMJJ streamflow and north Atlantic SST is not evident in either DJF or MAM. Furthermore, the correlations for high pass filtered data are for the most part not significant at $p<0.10$ (denoted by the black contours). The correlations become significant in the tropical Pacific for gages further south in the basin.

Turning to the low pass filtered data (Figure 16), correlations with SSTs are higher for this smoothed time series, with peak positive correlations between r = 0.50 to r = 0.75 in the eastern tropical Pacific and r = -0.50 to r = -0.75 in the subtropical Atlantic. This is unsurprising, since we expect the correlations to be stronger on decadal timescales due to the aggregated effect from multiple warm (cold) years in the tropical Pacific (Atlantic) on SWUS precipitation (Chen and Wallace 2015; Cayan et al. 1999; Enfield et al. 2001; Thomas 2007; Nowak et al. 2012). Despite the

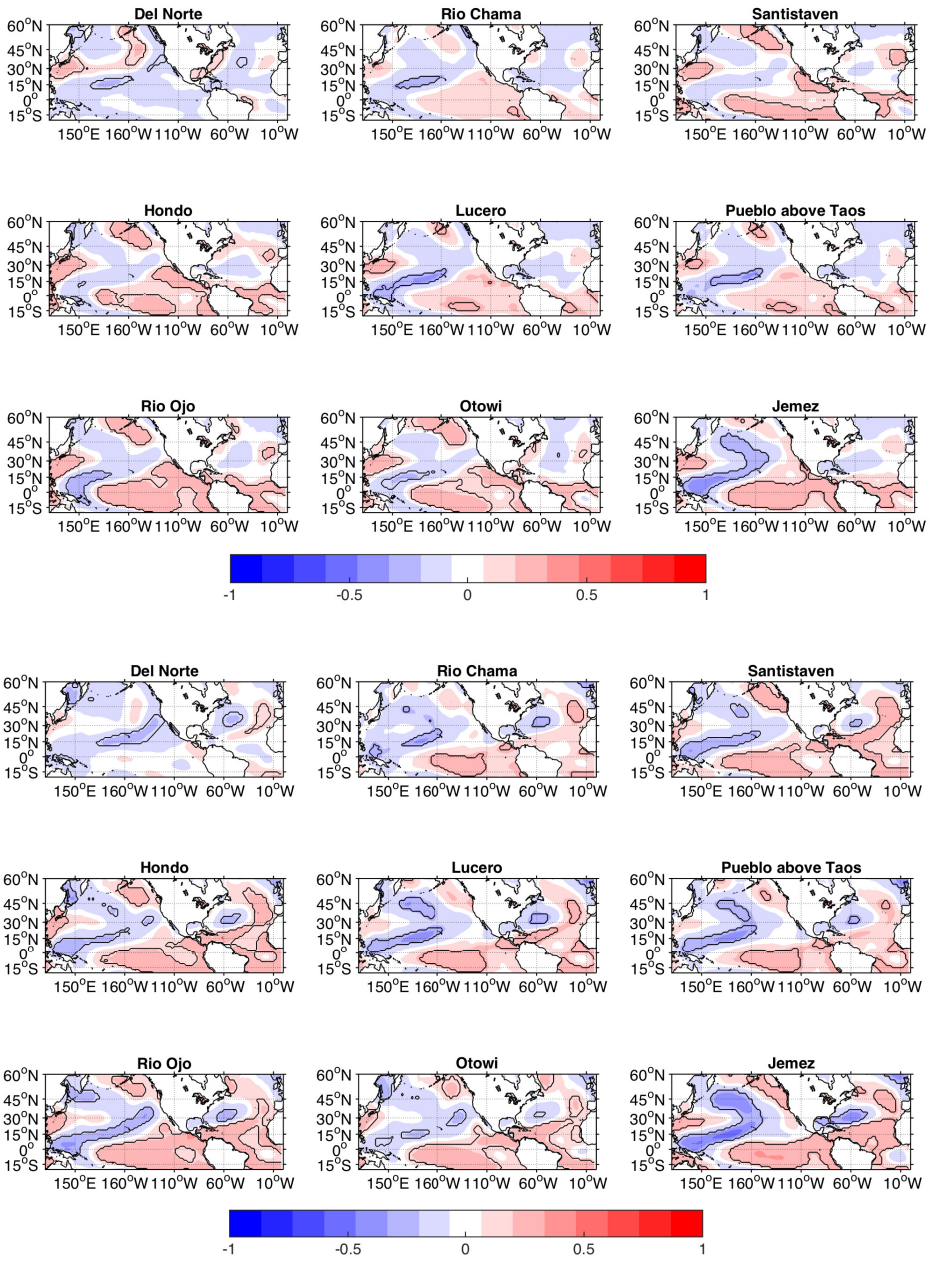

Figure 15: High pass filtered ERSSTV4 DJF (top) and MAM (bottom) SST correlated with high pass filtered AMJJ streamflow for all years covered by stream gages. High pass filtering was done using a cutoff frequency of 7 years. Colorbar indicates magnitude of the correlation [r = 0 to 1]. Areas that are significant at $p<0.1$ lie within the black contour.

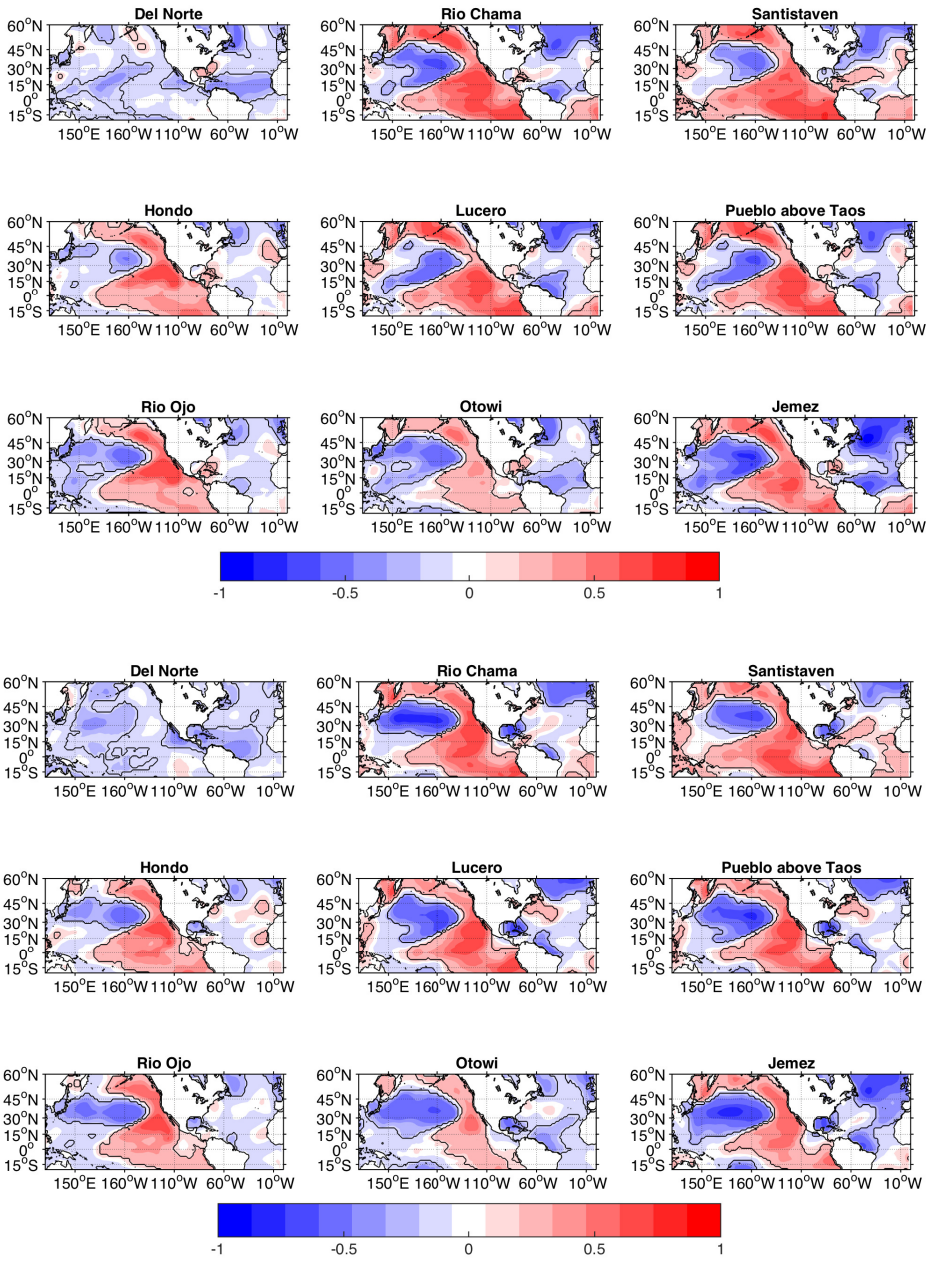

Figure 16: Low pass filtered ERSSTV4 DJF (top) and MAM (bottom) SST correlated with low pass filtered AMJJ streamflow for all years covered by stream gage. Low pass filtering was done using a cutoff frequency of 7 years. Colorbar indicates magnitude of the correlation [r = 0 to 1]. Areas that are significant at $p<0.1$ lie within the black contour.

limited significance (our effective degrees of freedom dropped from n=36 to n=8 in the smoothed time series), these results are consistent with the expected physical processes (McCabe et al. 2004; Schubert 2009). We find that the predictability is increased on decadal timescales.

To address further the interannual variability of Pacific SST and streamflow, we find the maximum monthly flow in a given water year and plot it along with the value of the DJF NINO3.4 index for the full length of each stream gage (Figure 17, separately for the northern, middle and southern gages). The northern gages correspond less to NINO3.4 SST (maximum r = 0.25) than the middle and southern gages (maximum r = 0.31). This is consistent with the ENSO precipitation teleconnection pattern being stronger in the southern half of the URG region. Results indicate that although high flows typically correspond with positive DJF NINO3.4 values, several notable exceptions occur. This includes the highly positive flow anomalies in 1942,1984 and 1985 following negative DJF NINO3.4, and negative flow anomalies in 1958 and 2002 following a positive DJF NINO3.4.

Figure 18 extends this analysis to include the influence of both the tropical Pacific and Atlantic on streamflow. We plot the AMJJ streamflow for each year going back the full length of each stream gage. The magnitude of AMJJ flow is scaled and plotted as marker diameter along with the corresponding value of DJF NINO3.4 and DJF TNA in the season preceding the high flow. The circle is colored red if it is one of the top 10 AMJJ flow events in the record. Positive DJF NINO3.4 and negative DJF TNA, based on prior work, is the configuration expected to produce above normal streamflow in the SWUS (McCabe et al. 2004; Schubert 2009). Figure 18 shows in general that moving south in the basin leads to higher monthly streamflow occurring after warm NINO3.4. There is more variability in the impact of DJF TNA on AMJJ streamflow for the highest seasonal events, with high streamflow events occurring following both warm and cold DJF TNA.

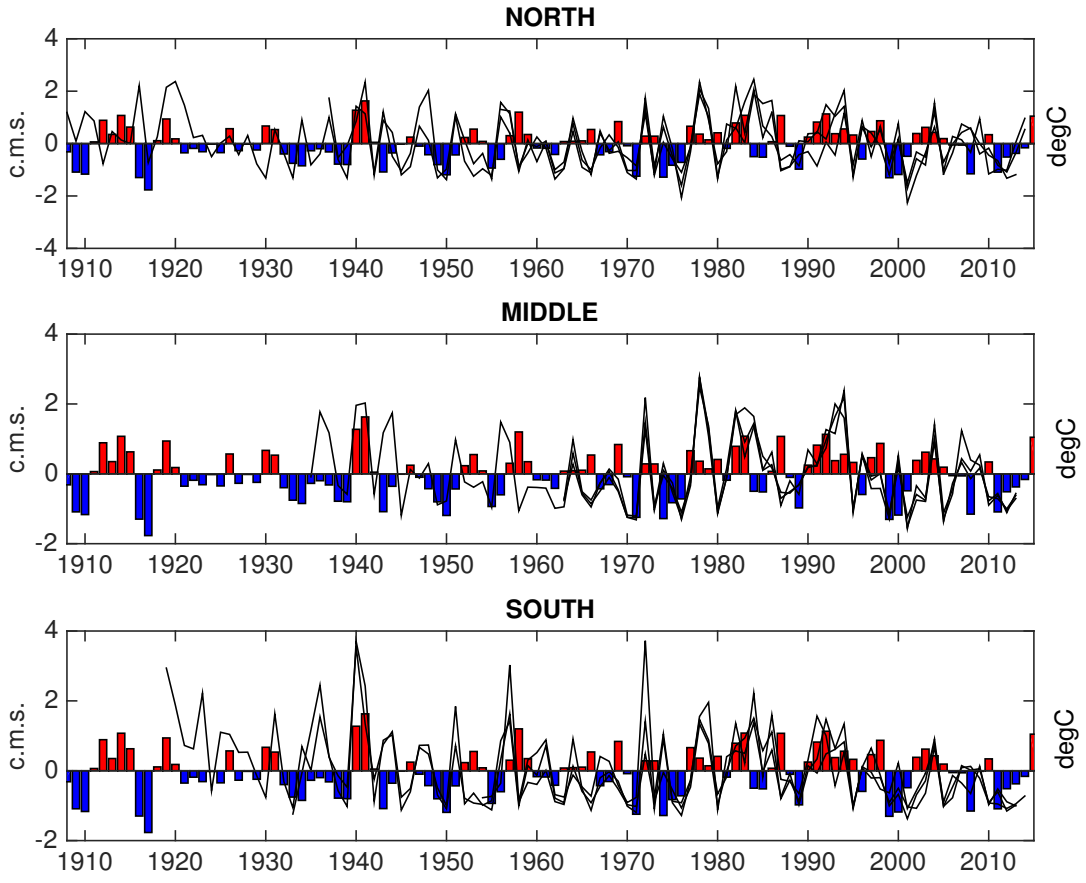

Figure 17: Bar graph shows NINO3.4 SST anomaly (^oC) for the DJF season, and black lines show the standardized anomaly for the maximum monthly flow occurring in each water year (c.m.s.). These are arranged as follows: the three most northern gages (Del Norte, Rio Chama, Santistaven) (top panel), middle gages (Hondo, Lucero, Pueblo) (middle panel) and southern gages (Ojo, Otowi, Jemez) (bottom panel).

This figure demonstrates that exceptions to the 'ideal' conditions conducive to high flow exist: high monthly streamflows can occur following cold NINO3.4 or warm TNA events (or both). We also used bootstrap statistics, and resampled the AMJJ streamflow data 1000 times and stratified it according to SST phase, and found that the percentage of total streamflow in each quadrant is no more than that which is likely to occur by chance at $p < 0.10$. These results again indicate the limited explanatory power of SST on interannual flows.

Given the limited explanatory power of SST on streamflow we also looked at atmospheric moisture convergence corresponding to the highest streamflow events. Results indicated that a large variety of atmospheric circulation patterns can lead to wetting anomalies on the URG. The lack of a consistent pattern in atmospheric anomalies contributing to these high flow events suggests that many of them are forced by transient systems rather than SST.

2.3.3 Climatic causes of decadal variability of URG flow

To investigate the strength of the SST-streamflow relationship on decadal timescales we turn our analysis to the longer streamflow timeseries of Del Norte and Otowi (Figure 14). In these streamflow timeseries we identify dry decades (1945-1975 and 1996-present) and wet decades (1900-1920 and 1979-1995). Figure 19 contains composite anomalies for the early century dry decades (1945-1975) and wet decades (1900-1920) for both water year PRISM precipitation and DJF ERSST V4 SST. For the dry composite, widespread negative precipitation anomalies occur over the SWUS and include the region of the URG. The early wet composite has wet anomalies over the SWUS in a region more centered over the Rio Grande basin. This is the early 20th century North American pluvial of 1900 to 1917 (Woodhouse et al. 2005; Cook et al. 2011b).

The pattern of DJF SST for the dry years indicate a region of cooling in the equatorial Pacific

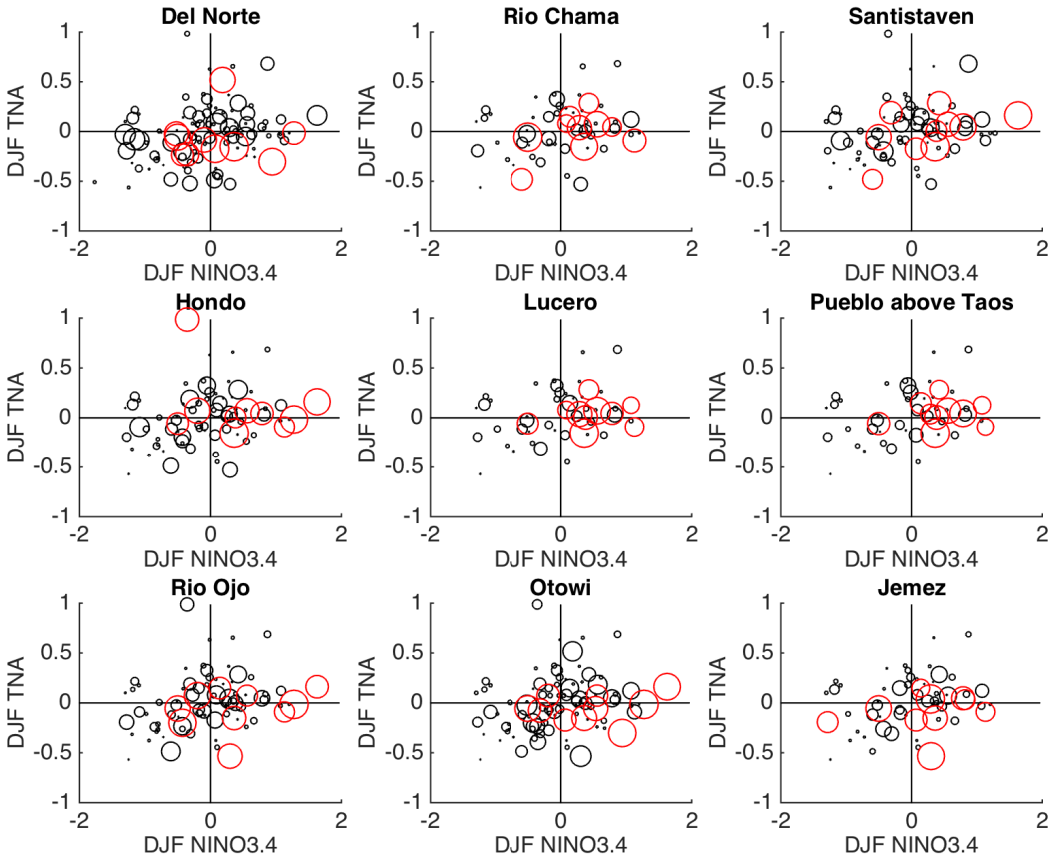

Figure 18: Scatter plot of NINO3.4 DJF, TNA DJF and the associated AMJJ streamflow at each stream gage. The size of the AMJJ flow is exponentially scaled and represented by the radius of the circular marker. Units on the x- and y-axis ^oC. Red circle coloring indicates the event is a top 10 AMJJ streamflow in the period of record.

and along the North American west coast, positive anomalies in the central North Pacific and positive anomalies in the tropical North Atlantic (Figure 19, bottom left panel). This decadal pattern of SST is consistent with the cool phase of the PDO (characterized by a cool equatorial Pacific and warm North Pacific (Zhang et al. 1997)), and the warm phase of the AMO (Enfield et al. 2001), ideal conditions for a drier than normal climate in the SWUS (Schubert 2009). The composite for wet years indicates a warm equatorial Pacific, cool north east Pacific and cool tropical north Atlantic. The weakness of the tropical Pacific SST anomalies during the pluvials, however, is consistent with Cook et al. (2011) who found little evidence of tropical Pacific driving of the early 20th century pluvial. Again, this disconnect between the tropical Pacific and streamflow highlights the limited explanatory power of SST on streamflow.

Figure 20 examines decadal variability for the later part of the twentieth century to present, for the two halves of the water year (October to March and April to September) in precipitation and SST. For October to March, the wet decades (1979-1995) minus the dry decades (1996 - 2015), show positive precipitation anomalies over the region of the URG, positive SST anomalies in the equatorial Pacific, negative SST in the north Pacific, and negative SST anomalies in the Atlantic. The Pacific SST pattern and the cyclonic flow over the central north Pacific are consistent with the positive phase of the PDO which has been associated with above normal streamflow and precipitation in the SWUS (Zhang et al. 1997; Barlow et al. 2001; Cayan et al. 1999; Pascolini-Campbell et al. 2015). The magnitude of these anomalies is reduced in April to September.

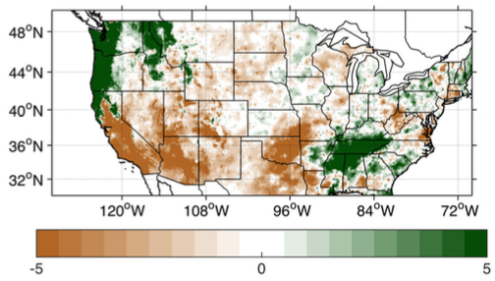

(a) OCT - MAR [1945 - 1975] - 20C

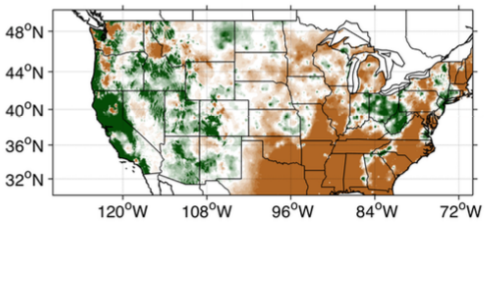

(b) OCT - MAR [1900 - 1920] - 20C

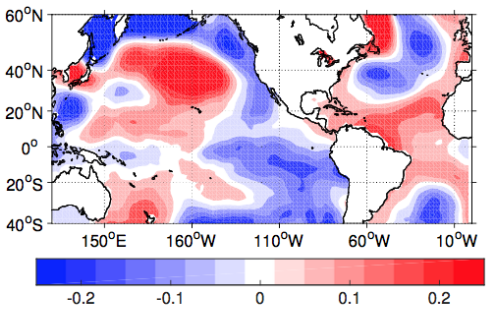

(c) DJF [1945 - 1975] - 20C

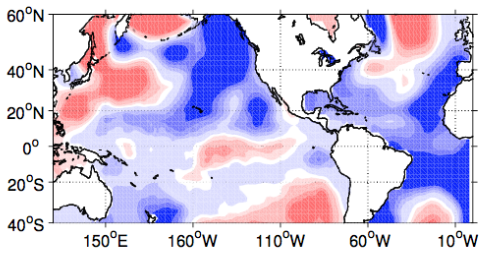

(d) DJF [1900 - 1920] - 20C

Figure 19: Dry decades (1945-1975) minus 20th century climatology (left panels) and wet decades (1900-1920) minus 20th century climatology (right panels) for water year composite PRISM precipitation (top) and DJF ERSST V4 SST (bottom).

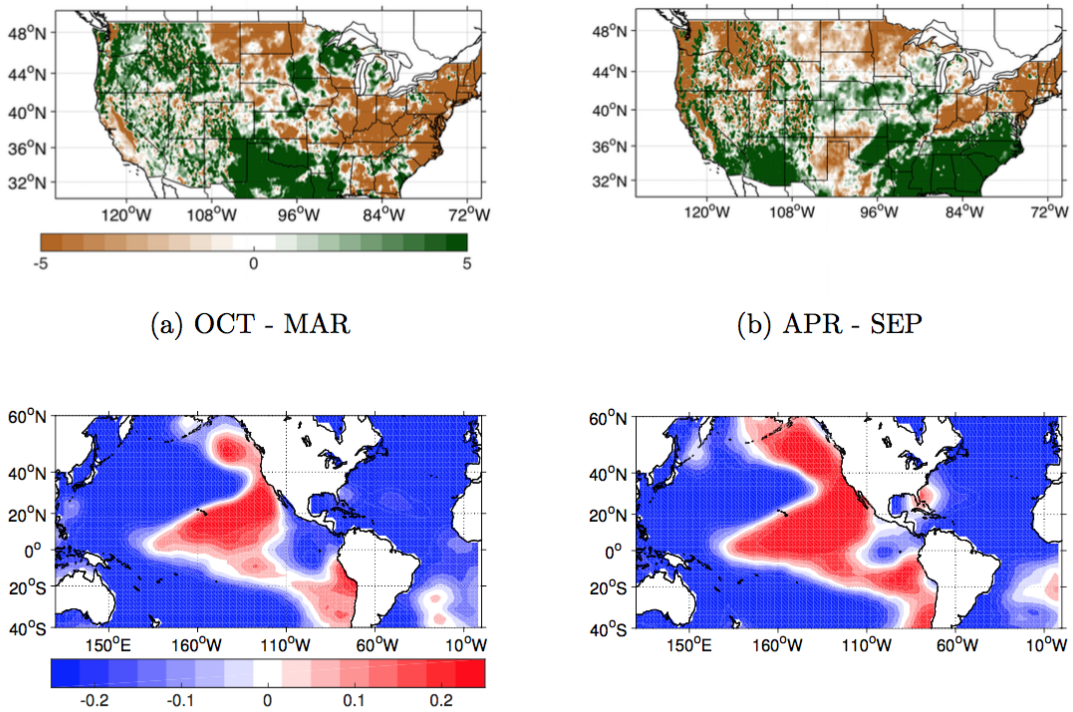

(a) OCT - MAR

(b) APR - SEP

(c) OCT - MAR

(d) APR - SEP

Figure 20: Wet decades (1979-1995) minus dry decades (1996-2012) composites. Top panel: PRISM precipitation. Colorbar indicates magnitude of anomaly [mm/day]. Bottom panel: ERSSTV4 SST. Colorbar indicates magnitude of SST anomaly [$^{\circ}C$]. Oct-Mar (left) and Apr-Sep (right).

2.4 Discussion and Conclusions

This study has examined 1) the controls on the seasonal cycle and variability of URG streamflow, and 2) the ocean and atmosphere mechanisms which result in anomalous streamflow. We extend the work of previous authors on the role of ENSO and PDO on URG streamflow (Lee et al. 2004; Guan et al. 2005; Khedun et al. 2010; Kahya and Dracup 1994), and other studies which examine the interrelationship of different modes of climate variability on SWUS precipitation (McCabe et al. 2004) by providing the following findings:

1. The mean seasonal cycle of streamflow for the URG is characterized by a spring-summer peak, which occurs later for northern gages and earlier for southern gages (Figure 12). This is consistent with the timing of winter snowpack melt (Lee et al. 2004). Spring-summer streamflow is influenced the most by precipitation in the preceding winter-spring throughout the URG, with all months being about equally important.

2. Assuming a linear relationship between SST and AMJJ streamflow, as in prior studies of the URG (Lee et al. 2004; Khedun et al. 2010), the results suggest limited influence of the oceans on interannual flow variability. To the extent there is an influence, the ocean configuration favoring above normal URG streamflow consists of a warm equatorial Pacific and cold north Atlantic in the winter-spring preceding spring-summer flow (Trenberth et al. 1998; Enfield et al. 2001; McCabe et al. 2004; Kushnir et al. 2010). The relationship of flow to tropical SSTs weakens to the north, meaning that the areas producing the largest share of native inflow have the weakest relationship with tropical Pacific and Atlantic SSTs.

3. Some of the largest streamflow anomalies on interannual timescales do not follow the ideal conditions of a warm tropical Pacific and cold north Atlantic, such as 1942, 1984 and 1985.

Analysis of atmospheric moisture transport for these years indicates that anomalous convergence located in the URG is driven by a variety of atmospheric circulation patterns. The lack of a consistent pattern in atmospheric anomalies contributing to these high flow events, suggests that many of them are forced by transient systems rather than persistent circulation anomalies driven by SST.

4. Decadal high flow periods from 1900 - 1920, 1979 - 1995, and low flow periods from 1945 - 1975 and 1996 - 2014, are found to be influenced by the phases of the PDO and AMO. The SST composite for dry decades (1945 - 1975) shows SST patterns characteristic of the cool PDO and warm AMO phases. The drop in URG streamflow in the most recent decades (1996- 2014) is associated with a turn to a cool PDO and warm AMO. The increase in multiple warm Pacific SST years during positive PDO events was also found to produce above normal streamflow in studies of other basins (Kiem and Franks 2004). We conclude that on decadal timescales, sustained periods of both high and low flow can be explained in terms of oceanic decadal variability.

The ocean-atmosphere configurations described explain streamflow variability in the URG on timescales of months to decades. However, much of the streamflow variability on interannual timescales is still unexplained by the Pacific and Atlantic SST teleconnections. Several of the highest flow years do not follow a warm Pacific/cold Atlantic configuration. Further, atmospheric anomalies demonstrate a wide range of conditions which can produce localized URG wetting. This suggests there will be limited predictability of URG flow on interannual timescales. The aggregate effect of multiple warm Pacific SST years, as occurs during positive PDO phases, contributes decadal periods of high flows and vice versa for negative PDO phases. In particular the declining

flow over recent decades can be explained in terms of decadal changes in Pacific and Atlantic SSTs toward a state (cold tropical Pacific - warm tropical North Atlantic) that is ideal for inducing dry conditions over the URG headwaters. As Rio Grande flow will be impacted by human driven climate change this information on natural variation of flow is essential for its management, lying as it does in a region where climate models project an increasingly arid climate (Seager et al. 2007; Vano et al. 2014; Ault et al. 2014).

3 Dynamics and variability of the spring dry season in the United States Southwest as observed in AmeriFlux and NLDAS-2 data

3.1 Introduction

There is a region of the interior Southwest United States (SWUS) which has two seasons of precipitation: one from the winter storm track and one from the North American summer monsoon (NAM). This region undergoes two periods of vegetation green-up (Adams and Comrie 1997; Guirguis and Avissar 2008), with a dry season occurring throughout the intervening spring months when ecosystem productivity declines. The bimodality of vegetation green-up, and the characteristics of spring drying, clearly are a result of interactions of precipitation, snowmelt, soil moisture and evapotranspiration (ET) but these mechanisms are not fully understood (Notaro et al. 2010; Vivoni et al. 2008).

The NAM is the dominant source of moisture in the region, delivering a large amount of precipitation as rain during the summer months (Adams and Comrie 1997). A smaller peak in precipitation also occurs during the winter in the form of both rain and snow, and is largely influenced by the Pacific storm track. Ecosystems are highly sensitive to moisture inputs in this arid region of the SWUS, and soil moisture provides a critical connection between precipitation and vegetation growth. Prior studies using both observations and land surface modeling for the SWUS, have identified the storage of water in soils from winter to spring as being critical to the bimodal seasonal cycle of vegetation green-up (Notaro et al. 2010; Muldavin et al. 2008).

The essential climate and ecological processes in the region are as follows. Winter precipitation

and snowmelt add water to the soils, which is then gradually drawn down by vegetation growth and rising spring temperatures, leading to enhanced ET (Kurc and Small 2007; Vivoni et al. 2008). Vegetation greening reaches its spring peak, and then declines with soil moisture during the spring dry season, until the arrival of the NAM, which creates a new pulse in soil moisture and vegetation growth. Climate controls on spring drying can therefore influence the timing and intensity of spring and summer greenings.

The severity of spring drying and the availability of water for ecosystems, is in part controlled by the initial input of moisture from winter precipitation. In addition to internal atmosphere variability, year-to-year variations in winter precipitation are modulated by tropical Pacific sea surface temperatures (SSTs). These teleconnections are well documented, with the El Niño Southern Oscillation (ENSO) being the dominant driver interannually (Ropelewski and Halpert 1986, 1989), and the Pacific Decadal Oscillation (PDO) operating on interdecadal timescales (McCabe et al. 2004). The tropical North Atlantic ocean also plays a likely role, with cold years favoring above normal precipitation in the SWUS (Enfield et al. 2001). The end of the spring dry period is marked by the arrival of the NAM, which also varies interannually, and has been weakly influenced by phases of ENSO (Higgins et al. 1999; Castro et al. 2001), the Madden-Julian-Oscillation (MJO) (Higgins and Shi 2001), and soil moisture (Small 2001).

Twentieth-century observations have indicated an earlier onset of spring in the SWUS, as defined by the timing of blooming and snowmelt, which is primarily attributed to increased spring temperatures (Cayan et al. 2001; Ault 2015). The magnitude, timing and melt of the snowpack following winter precipitation influences the storage of water in soils, and observational studies of Snow Telemetry (SNOTEL) sites have indicated a trend towards reduced snowpack in the western United States and earlier melt (Mote et al. 2005; Fritze et al. 2011; Mote et al. 2018). Impacts on

the SWUS include an earlier dry season, an earlier spring vegetation green-up as well as earlier spring streamflow (Fritze et al. 2011; Hand et al. 2016). An earlier spring dry season also leads to a longer wildfire season (Westerling et al. 2006; Williams et al. 2014) and can enhance dust emissions (Hand et al. 2016).

Modeling studies have also projected increased drying in the SWUS due to future reductions in precipitation and increases in potential ET (PET) (Seager et al. 2007; Cook et al. 2015; Seager et al. 2012), and this drying is particularly robust during the spring (Gao et al. 2014). Analysis of the Coupled Model Intercomparison Project Phase 5 (CMIP5) ensemble attributed projected spring drying in the SWUS to decreased mean moisture convergence associated with enhanced dry zonal advection (Ting et al. 2018). Other modeling studies have indicated a delayed onset of the NAM, and declines in early season NAM precipitation (Cook and Seager 2013), or overall weakening of the NAM under enhanced greenhouse gas forcing (Pascale et al. 2017). It follows that implications for the dry season would include a longer and more intense spring drying, with resulting ramifications on ecosystems in this sensitive SWUS region.

Given the complex interaction between multiple variables (precipitation, snowmelt, ET, runoff, soil moisture and vegetation), different moisture inputs (winter storms and NAM), modes of climate variability (ENSO, PDO), and anthropogenic change, a comprehensive understanding of the climate dynamics required to understand past and projected future change in this unique region is needed. In this study we will address the following:

1. What mechanisms produce the observed seasonal cycle of i) bimodal vegetation activity and ii) the intervening spring dry season?

2. How has the hydroclimate of the spring dry season changed on decadal timescales and how

has this influenced the magnitude, timing and duration of the spring dry season?

3. How are these decadal changes expressed in terms of the interaction of precipitation, snowmelt, ET, runoff, soil moisture and vegetation? Is there an influence of warming temperatures?

4. What are the implications of climate change and continued anthropogenic warming for the spring dry season and ecosystems?

This study will seek to answer these questions using *in situ*, remotely sensed observations and land surface models (LSMs). Results from this study will identify the key climate mechanisms which influence the climatology, decadal variability and trends in spring drying in this region, and provide a background for what to expect under future climate change.

3.2 Data and Methods

To examine the characteristics at the site level we use *in situ* observations from the Ameriflux network. For a broader study of the dual season region over a longer time period we examine data from LSMs forced by gridded meteorological data.

The *in situ* observations of precipitation, net ecosystem productivity (NEP), latent heat flux and soil water content are obtained from the Ameriflux network for different sites in the SWUS (available online at: http://ameriflux.lbl.gov), and their location, climate and temporal availability are listed in Table 3. The Ameriflux network uses eddy covariance methods to make half-hourly temporal resolution estimates of the fluxes of ecosystem CO_2, water and energy in North America (Baldocchi et al. 2001).

Table 3: Summary of Ameriflux in situ data

Site Name	Location	Temporal Availability	Vegetation	Elevation (m)
US-Valles Caldera Ponderosa Pine (US-Vcp)	35.8, -106.6	2007 - 2014	Evergreen Needleleaf Forest	2500
US-Valles Caldera Mixed Conifer (US-Vcm)	35.8, -106.5	2007 - 2014	Evergreen Needleleaf Forest	3030
US-Flagstaff Managed Forest (US-Fmf)	35.1, -111.7	2006 - 2010	Evergreen Needleleaf Forest	2160
US-Flagstaff Unmanaged Forest (US-Fuf)	35.1, -111.8	2006 - 2010	Evergreen Needleleaf Forest	2180
US-Flagstaff Wildfire (US-Fwf)	35.4, -111.8	2006 - 2010	Grasslands	2270
US-Sevilleta grassland (US-Seg)	34.4, -106.7	2007 - 2014	Grasslands	1596
US-Sevilleta shrubland (US-Ses)	34.3, -106.7	2007 - 2014	Open Shrublands	1604
US-Willard Juniper Savannah (US-Wjs)	34.4, -105.9	2007 - 2014	Savannah	1931
US-Mountainair Pinyon-Juniper Woodland (US-Mpj)	34.4, -106.2	2007 - 2014	Woody Savannah	2196
US-Santa Rita Creosote (US-SRC)	31.9, -110.8	2008-2015	Open Shrublands	991
US-Santa Rita Grassland (US-SRG)	31.8, -110.8	2008 - 2015	Grasslands	1291
US-Santa Rita Mesquite (US-SRM)	31.8, -110.8	2004 - 2015	Woody Savannas	1120
US-Walnut Gulch Lucky Hills Shrub (US-Whs)	31.7, -110.0	2007-2015	Open Shrublands	1370
US-Walnut Gulch Kendall Grassland (US-Wkg)	31.7,-109.9	2004-2015	Grasslands	1531
US-Audobon Research Ranch (US-Aud)	31.6, -110.5	2002-2015	Grasslands	1469

Table 4: Summary of other data sets

Dataset	Temporal Availability	Resolution	Variable
NLDAS-2 Noah, Mosaic, VIC	1979 - 2018	1/8th^o, hourly	Precipitation, soil moisture, snow melt evapotranspiration, total runoff
SM-MCDI	1895 - 2018	1/8th^o, monthly	Soil moisture 0-200 cm
CLIMGRID	1895 - 2018	1/24th^o, monthly	Precipitation, temperature
GIMMS	1981 - 2015	1/12th^o, half-monthly	NDVI
NOAA NCEP-NCAR Reanalysis	1948- 2018	2.5^o, monthly	SST, 200mb geopotential height

Given the limited temporal and spatial coverage of the Ameriflux sites, we also use output from the second phase of the National Land Data Assimilation system (NLDAS-2) LSMs Noah, Mosaic and VIC for soil moisture, ET, snowmelt, snowfall, and total runoff (surface plus subsurface) at 1/8th-degree resolution (Xia et al. 2012), available online at: https://ldas.gsfc.nasa.gov/nldas/). The LSMs do not have dynamic vegetation and annual cycle of the leaf area index (LAI) is prescribed. The LSM data are available from 1979 to present at hourly temporal resolution. Each of the three LSMs are forced with Climate Prediction Center unified gauge-based precipitation data with Parameter-elevation Regressions on Independent Slopes Model (PRISM) precipitation adjustments ((Daly et al. 2008b) see: http://prism.oregonstate.edu) and the other meteorological forcing data come from the North American Regional Reanalysis (Mesinger et al. 2006).

Half-hourly and hourly resolution data are averaged into five day means. Where data are available to present, we analyze through 2017 because 2018 is not yet complete. We validate the NLDAS-2 LSMs used in this study by comparing their data for the grid points and time period that correspond to the *in situ* Ameriflux sites within the dual season region (where both winter and summer precipitation peaks are observed in the mean annual cycle). In general, sufficient agreement exists between the in situ observations and the LSM simulations to justify use of the latter

for larger scale and longer time period analyses.

For a longer-term perspective, we use monthly estimates of 0-200 cm soil moisture based on a Model Calibrated Drought Index (MCDI) developed by Williams et al. [2017]. These estimates cover 1895-2018 and are based on a bucket-type moisture-balance model that was tuned by Williams et al. [2017] to have the temporal persistence properties of 0-200 cm monthly soil moisture simulated by the the Noah LSM. The MCDI calculations are forced by monthly precipitation and PET. Monthly precipitation and temperature are from the National Oceanic and Atmospheric Administration Climgrid data set (Vose et al. 2014) (available online at https://www.ngdc.noaa.gov/). The PET calculation also uses vapor pressure from PRISM gridded monthly mean dew-point data (Daly et al. 2008b), and wind and solar radiation data from NLDAS-2 and the version 2 Princeton Global Forcing Dataset (Sheffield et al. 2006) (http://hydrology.princeton.edu/data/pgf/v2/0.5deg/). The soil moisture estimates based on the MCDI (hereafter SM-MCDI) agree very well with the NLDAS-2 soil moisture in the SWUS and permit us to examine historical soil moisture extending prior to the 1979 start date of NLDAS-2. Also the MCDI is forced by observational climate datasets that are more accurate than reanalysis data used to force the NLDAS-2 LSMs.

To measure vegetation green-up, we use the Global Inventory Modeling and Mapping (GIMMS) satellite Normalized Difference Vegetation Index (NDVI) which is available twice monthly from 1981 to 2015 at 1/12th-degree resolution (Tucker et al. 2004). We also use SST and 200mb geopotential height from NOAA NCEP-NCAR Reanalysis at monthly time resolution and 2.5-degree spatial resolution (available online at https://www.esrl.noaa.gov/) (Kalnay et al. 1996).

3.3 Results

3.3.1 Characterization of precipitation regime in the SWUS

First, we identify the region of the SWUS where the average seasonal cycle of PRISM precipitation had one or more peaks during 1979 to 2017 (Figure 21). To identify the region with two peaks, we divide the seasonal cycle into three seasons: fall-winter (October to March), spring (April to June), summer (July to August). Since we are primarily interested in the region with a winter and summer peak, a grid point is said to have two peaks if the mean fall-winter precipitation is greater than the spring precipitation, and the summer precipitation is also greater than the spring precipitation. We also check this against maps of precipitation seasonality for North America (online at http://www.cpc.ncep.noaa.gov/).

This two peak region covers most of Arizona, western New Mexico, and extends south into Mexico. Next, a box spanning the northern portion of this bimodal region (red outline shown on Figure 21), that encompasses the available Ameriflux monitoring stations is chosen to represent this region later in the study. The bimodal regions identified in this map are checked against existing observations for seasonality of precipitation in North America (Adams and Comrie 1997).

3.3.2 Observations: seasonal cycles of precipitation, ET, soil moisture, and vegetation

We analyze *in situ* observations from the Ameriflux network for 15 different monitoring sites from the SWUS that are located in or near the bimodal region identified in Figure 21 (descriptions in Table 3, location shown in Figure 21). The seasonal cycles of precipitation for each of the 15 sites are shown in Figure 22 (top panels) and compared with the NLDAS-2 precipitation forcing for the same location and temporal availability (we save a quantitative evaluation between

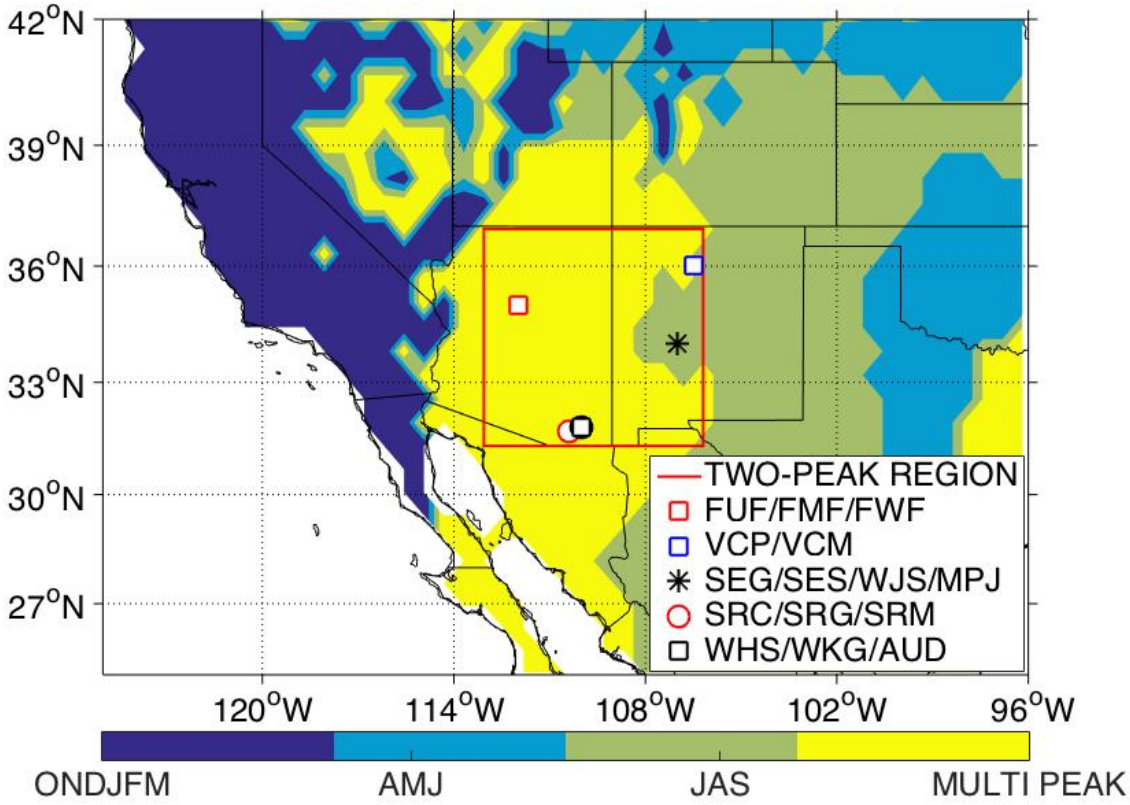

Figure 21: Map of study area. Shading indicates season of maximum precipitation (ONDJFM, AMJ, JAS or bimodal). Red box indicates region used in the study as the bimodal precipitation region. We indicate location of the Ameriflux sites (Fwf, Fuf, Fmf, Vcp, Vcm, Seg, Ses, Mpj, Wjs).

the Ameriflux and NLDAS-2 simulations for section 3c below). Each of the 15 sites receive precipitation in the winter months, but the seasonal cycle is dominated by the NAM with maximum precipitation occurring during the summer. Each site also has a dry season occurring during the late spring-summer. The seasonal cycle of Ameriflux ET (Figure 22, bottom panels) also shows bimodality: a smaller peak in ET during the early spring (March-April), declines to May-June, then increases to a second and greater peak during the summer.

Inter-site differences exist in the precipitation and ET among the various Ameriflux stations. The southern sites (SRC, SRG, SRM, Whs, Wkg, Aud) show a more dominant ET peak during the summer compared to the more northern sites. The highest precipitation during the main NAM season occurs at the Flagstaff, Arizona, sites (Fmf, Fwf, Fuf), presumably because of their higher elevation (2160m to 2270m). The next greatest NAM precipitation peak occurs at the southern sites (Whs, Wkg, Aud) near Tucson, Arizona, closer to the core of the monsoon.

We also examine the seasonal cycle of soil water content (which measures soil water from the top $\sim$ 10cm) from the available Ameriflux sites (Figure 23, bottom panels). Observations of soil water content indicate two peaks in soil moisture: for the northern sites (Fmf, Fwf/Fuf), the largest peak occurs during the late winter-spring (February-March), after which soil moisture declines to a minimum in April-May-June, before increasing to a second and smaller peak in the summer monsoon season (July-August).

Next we examine the seasonal cycle of vegetation in the bimodal region using observations of net ecosystem productivity (NEP) from the Ameriflux network (Figure 24, bottom panels) and GIMMS NDVI (Figure 24, middle panels). NEP is defined as the difference between gross primary production and total ecosystem respiration. When the NEP is positive, this indicates vegetation green-up, when negative it indicates vegetation senescence.

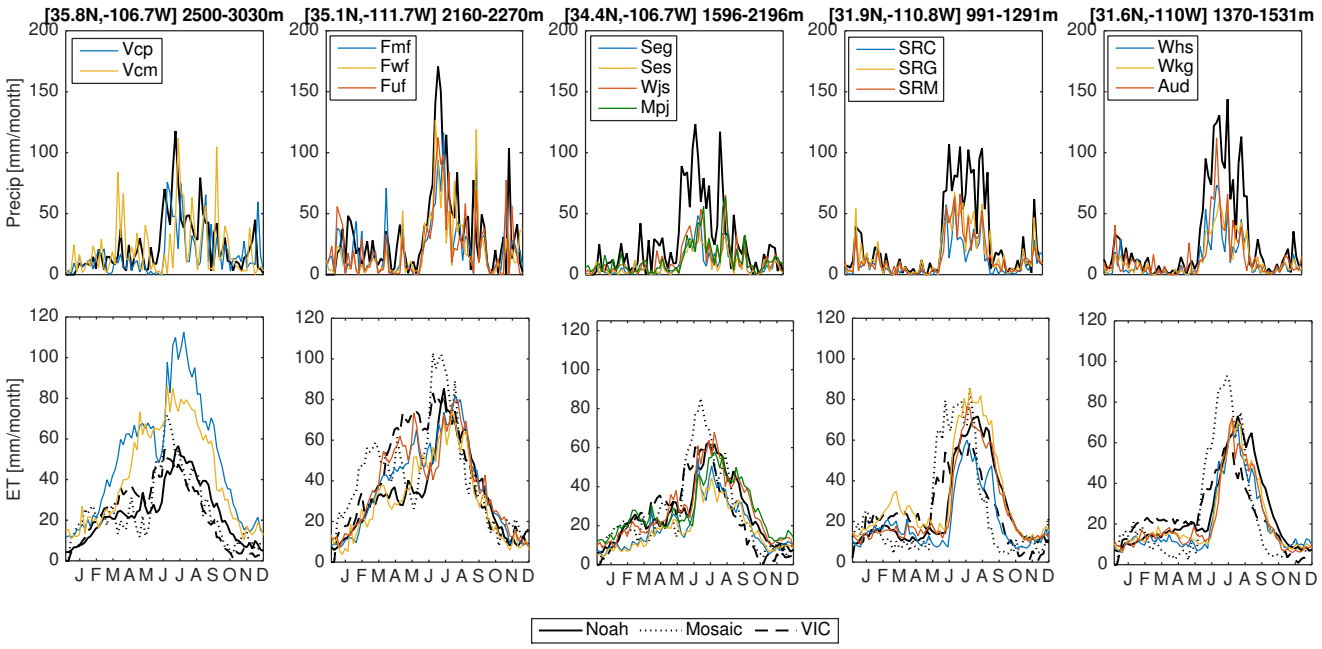

Figure 22: Comparison of NLDAS-2 and AmeriFlux sites in the bimodal precipitation region for precipitation (top panels - each LSM uses the same precipitation forcing) and evapotranspiration (ET) (bottom panels). Output from the NLDAS-2 models (Noah, Mosaic, VIC) corresponds to the grid point location of each of the AmeriFlux sites for the corresponding time period available (Vcp/Vcm sites 2007 - 2014, Fmf/Fwf/Fuf sites 2005 - 2010, Seg/Ses/Wjs/Mpj sites 2007 - 2014, SRC/SRG/SRM sites 2008 - 2014 and Whs/Wkg/Aud sites 2007 - 2014). Both NLDAS-2 and AmeriFlux data are plotted at a temporal resolution of 5 day means.

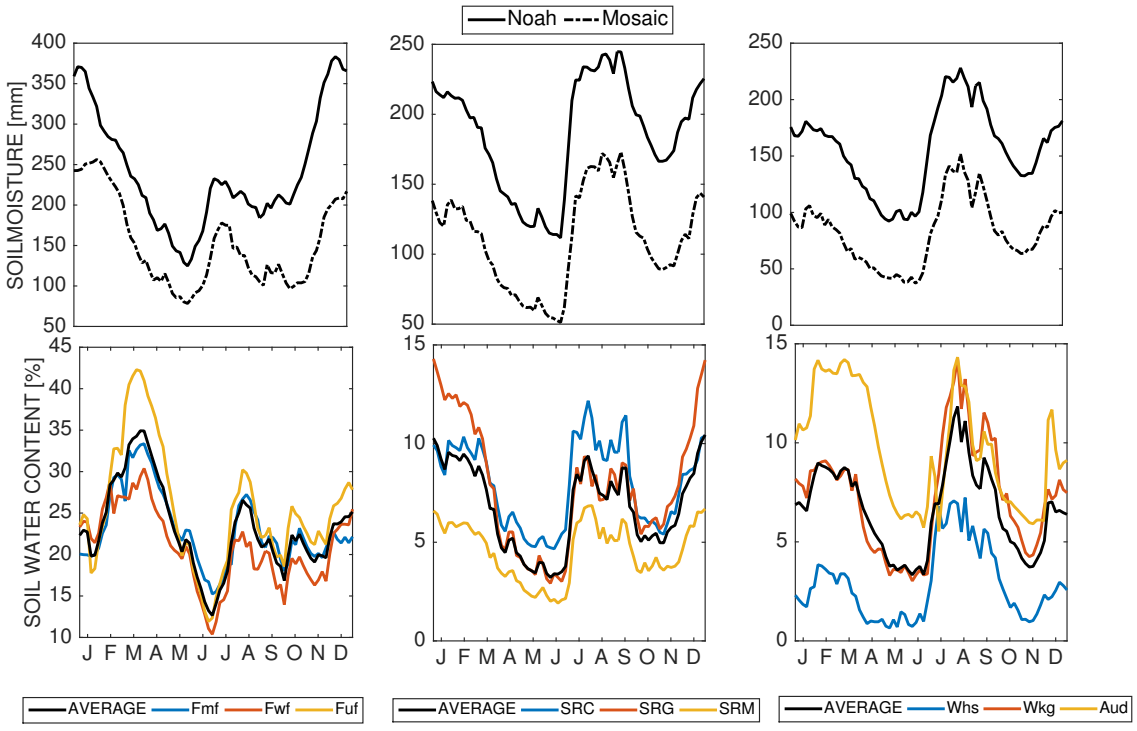

Figure 23: Seasonal cycle of NLDAS-2 (Noah, Mosaic) 0-10 cm soil moisture (top) compared with AmeriFlux soil water content in percent (derived from upper 10 cm of soil moisture) (bottom). This level is the only one available from the AmeriFlux network which is why we use it to compare with NLDAS-2. The NLDAS-2 soil moisture corresponds to the grid point location and available time period of the AmeriFlux site used.(Fmf/Fwf/Fuf, SRC/SRG/SRM sites, and Whs/Wkg/Aud sites). Both NLDAS-2 and AmeriFlux data are plotted at a temporal resolution of 5 day means.

NEP peaks twice annually for the different Ameriflux sites: once in the early spring (March-April), and again in the summer (JAS). The dry season (indicated by vegetation senescence) lies between approximately May-June for the different sites. Inter-site differences exist between the Ameriflux stations due to differences in vegetation type, elevation, and location (details in Table 3). For example, of the Flagstaff sites, the managed and unmanaged evergreen needleleaf forests (Fmf and Fuf respectively), have larger values of NEP than the other nearby grassland wildfire site (Fwf), as has been noted in previous studies (Dore et al. 2010; Sullivan et al. 2011). The NEP is higher for the Flagstaff and Valles Caldera sites than for the Sevilleta grass and shrubland sites, which is expected given the vegetation type (evergreen forest versus open shrublands). The more southern sites (SRC, SRG, SRM, Whs, Wkg, Aud) also have a much larger summer vegetation peak than spring peak consistent with the dominance of summer precipitation (Figure 22).

The observational GIMMS NDVI also is consistent with the Ameriflux pattern of bimodal vegetation greening at each of the sites, however the amplitude of vegetation growth and senescence is less pronounced than that in NEP.

3.3.3 Evaluation of NLDAS-2 LSMs with Ameriflux and GIMMS NDVI

Given the localized nature and short time period of the Ameriflux site data, we need to use the NLDAS-2 LSM simulations to obtain a spatially broader and longer term assessment of the spring dry season in the bimodal region.

In Figures 2 and 5 the seasonal cycles of precipitation, ET, soil moisture, and LAI of the Ameriflux sites in the bimodal region of the SWUS are compared with NLDAS-2 LSM simulations, and, in general, there is good agreement. The largest differences in precipitation for the two data sets occur at the central-eastern and southern Arizona sites where monsoon precipitation is too

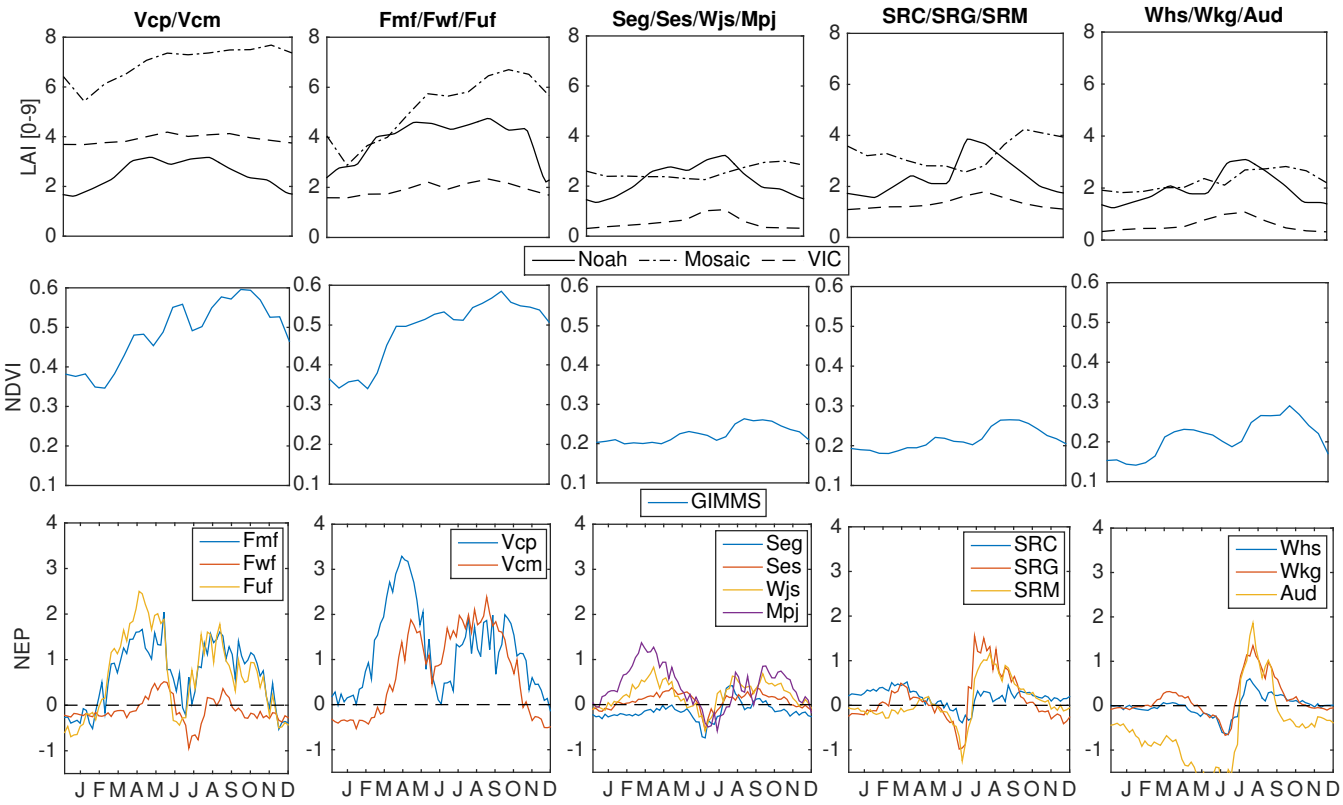

Figure 24: Seasonal cycle of NLDAS-2 Noah, Mosaic, and VIC leaf area index (LAI) (0-9) (top panels), GIMMS NDVI (middle panels), and the negative of AmeriFlux net ecosystem exchange (bottom panels). Net ecosystem exchange is defined as the total respiration (autotrophic plus heterotrophic) minus net primary production (NPP) and reflects ecosystem exchange of carbon with the atmosphere. During the growing season when productivity exceeds respiration, NEE is negative. Here we plot the negative of NEE (Net Ecosystem Productivity (NEP)) in order to better visualize plant growth. The NLDAS-2 leaf area index and GIMMS NDVI corresponds to the grid point location and available time period of the AmeriFlux site used.

high in NLDAS-2. Using Pearson's correlation we find the r-values between the seasonal cycle of precipitation from NLDAS-2 forcing and Ameriflux sites varies between a low value of r = 0.37 of the northern Valles Caldera site (Vcm), to r=0.93 at the Tucson site (Wkg).

NLDAS-2 LSMs and Ameriflux measurements are also in general agreement ($r > 0.5$) on the mean annual cycle of ET (Table 5). The largest difference between Ameriflux and NLDAS-2 ET occurs at the Valles Caldera northeastern site where NLDAS-2 ET is half that in Ameriflux. For the other 13 sites the magnitude and seasonal cycle of ET agree reasonably well between Ameriflux and NLDAS-2. The r-values for ET from the Ameriflux sites are greater with NLDAS-2 Noah than with either Mosaic or VIC.

Table 5: Correlation of NLDAS-2 LSM output with Ameriflux (r-values significant at α=0.05 unless surrounded by parentheses ())

	Vcp	Vcm	Fmf	Fwf	Fuf	Seg	Ses	Wjs	Mpj	SRC	SRG	SRM	Whs	Wkg	Aud
Precip	0.48	0.37	0.57	0.58	0.61	0.68	0.65	0.62	0.57	0.76	0.85	0.86	0.92	0.93	0.82
ET (Noah)	0.96	0.91	0.92	0.93	0.85	0.92	0.94	0.97	0.93	0.92	0.97	0.98	0.95	0.97	0.96
ET (Mosaic)	0.71	(0.21)	0.73	0.78	0.66	0.79	0.79	0.58	0.65	0.57	0.54	0.56	0.81	0.75	0.76
ET (VIC)	0.83	0.28	0.89	0.86	0.88	0.77	0.76	0.48	0.64	0.72	0.75	0.72	0.79	0.78	0.80
0-10 cm SM (Noah)	-	-	(-0.05)	0.36	(0.13)	-	-	-	-	0.88	0.74	0.90	0.87	0.95	0.46
0-10 cm SM (Mosaic)	-	-	(0.11)	0.51	(0.23)	-	-	-	-	0.89	0.69	0.89	0.86	0.94	0.48

Turning to soil moisture (0 - 10 cm), NLDAS-2 Noah and Mosaic (0 - 10 cm is not reported by VIC) are characterized by a bimodal seasonal cycle for the Flagstaff sites, but the winter peak is earlier in the year (January-February) compared to the Ameriflux observations (March). Away from the Flagstaff sites, LSM soil moisture broadly agrees with the observed soil water content. The other more southern Ameriflux sites have earlier winter soil water content peaks (January-February) and these compare well in timing with the NLDAS-2 soil moisture which also peaks at this time. The summer maximum occurs in June-July-August-September, and also agrees with the simulated NLDAS-2 soil moisture. The timing of the spring dry season is comparable across the region, and occurs in April-May-June. The timing of the soil moisture increase that ends the spring dry season also agrees between the Ameriflux sites and NLDAS-2, except for the Flagstaff sites where NLDAS-2 is one month too early. We speculate that the earlier soil moisture peak could be due to snowmelt in this region occurring too early in the NLDAS-2 models.

We compare observations of NEP and NDVI with NLDAS-2 prescribed LAI (Figure 24). Noah specified LAI best captures the bimodality of the two-peak greening and also most closely resembles GIMMS NDVI for the different sites (Figure 24). Mosaic captures some of the bimodality in the Flagstaff sites, however it is less pronounced than that from Noah. VIC also has a bimodal cycle at the Valles Caldera and Flagstaff sites, but it only has a single vegetation peak for the southern sites. Based on these results, we find that the Noah model best represents the observations, and we therefore use it in subsequent analyses.

3.3.4 Relationship of vegetation green-up with soil moisture

The relationship between vegetation green-up and soil moisture is explored in Figure 25. We create composites across sites and years of NEP from the 15 Ameriflux sites over the period of

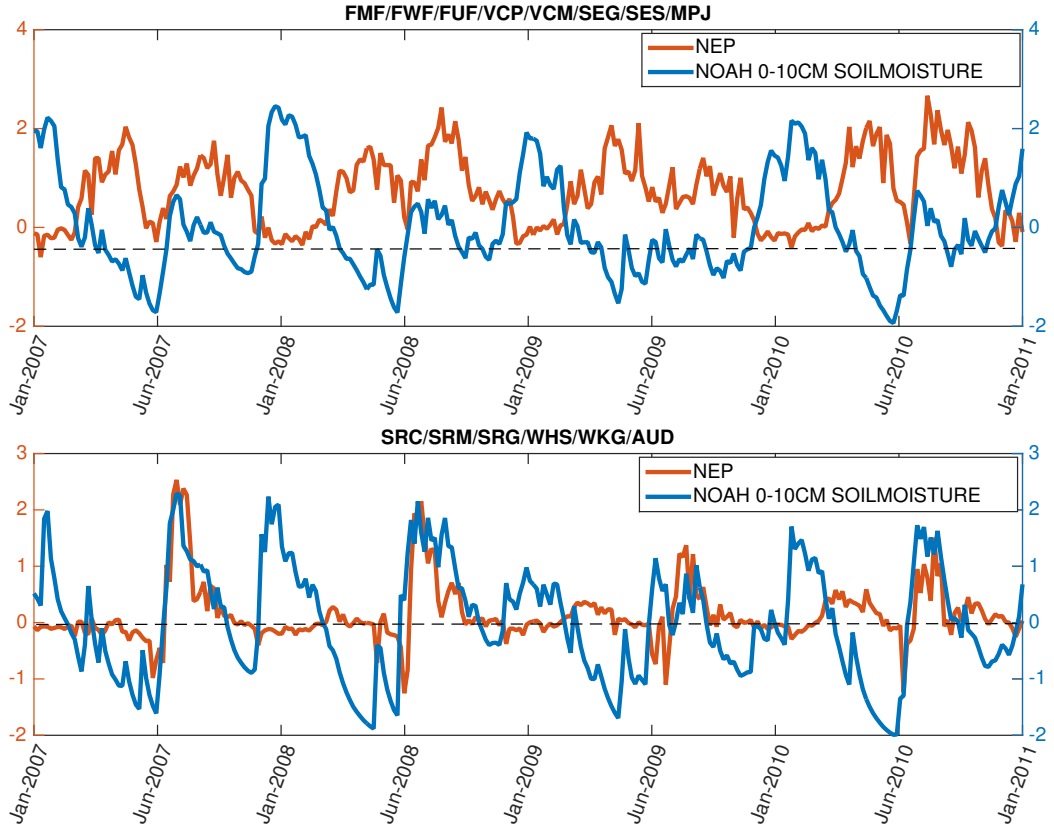

Figure 25: Composite of Net Ecosystem Productivity (NEP) for AmeriFlux sites (red line) and standardized Noah 0-10 cm soil moisture corresponding to sites (blue line). Data are in five-day means for 2007 to 2010. Top panel are for northern sites (Fmf, Fwf, Fuf, Vcp, Vcm, Seg, Ses, Srm, Mpj) and bottom panel is for southern sites (SRC, SRG, SRM,Whs,Wkg,Aud).

overlap (2007-2010) in five day means for the more northern sites (Figure 25, top panel) and southern sites (Figure 25, bottom panel). This is compared with a composite of Noah soil moisture (0 to 10 cm) at the grid point locations of the Ameriflux sites. We choose to use the model soil moisture since it provides a more continuous record of soil moisture than from the Ameriflux data (which has missing data in the timeseries). As a caveat we note that NLDAS-2 Noah vegetation is prescribed and has the same seasonal cycle each year, which will in turn influence soil moisture draw down. Therefore we expect soil moisture to not completely track the observations of NEP from Ameriflux.

The peak in winter soil moisture occurs during the low vegetation productivity winter months. NEP then increases during spring and draws down the soil moisture. This is more prominent among the northern sites (top panel). The NEP then declines when soil moisture has been drawn down to low values prior to the summer monsoon. The second maximum of NEP then follows after the monsoon driven summer maximum in soil moisture. An exception occurs in 2009 in which NAM rainfall was significantly below average (verified in records of PRISM precipitation for the summer of 2009). The green-up of vegetation with the NAM is particularly striking for the southern sites, which have greater vegetation productivity during summer and only a muted spring green-up despite a clear spring soil moisture maximum. This is consistent with the southern sites being dominated by C4 grasses which are more sensitive to summer conditions (Notaro et al. 2010).

The observations presented in this figure indicate the strong coupled relation between NEP and soil moisture (consistent with previous studies (Notaro et al. 2010; Muldavin et al. 2008)). Following this, we use soil moisture as an indicator of the dry season due to its strong association with ecosystem productivity.

3.3.5 Larger SWUS bimodal region: seasonal cycle of precipitation, ET and soil in NLDAS-2 Noah

Next, we turn our analysis to the broader SWUS bimodal area identified in Figure 21. We use spatially averaged precipitation, ET, and soil moisture (0 to 200 cm) to create seasonal cycles in five day means from 1979 to 2017 from the Noah output (Figure 26). First, we correlate the seasonal cycle of 5-day mean precipitation and ET from the average of the 15 Ameriflux sites and the corresponding NLDAS-2 grid points, and find that over the greater region, precipitation agrees at r = 0.79, and ET at r = 0.91. These high correlation values for the broader area give us confidence in using the spatially averaged Noah simulations for the rest of the analysis.

The 0 to 200 cm soil moisture shows a maximum in winter followed by a drying in the spring, which is restored to a smaller secondary peak in the summer. The 0 - 200 cm soil moisture has the same bimodal pattern as the 0 - 10 cm values. However, the winter and summer peaks occur later in the year and are more muted. The larger winter peak arises due to both the steady nature of precipitation in the winter months, allowing water to readily infiltrate the soil, and cooler temperatures and low evaporative demand (Loik et al. 2004). In the summer, monsoon precipitation is overall greater in magnitude and more intense, but also is short lived occurring in convective storms, and much of this water is lost to surface runoff. This is an increasingly important mechanism further south in the study region where monsoon precipitation dominates and the surface runoff to precipitation ratio is large (not shown). In addition, evaporative demand is also much greater during the summer, leading to soil moisture drawdown.

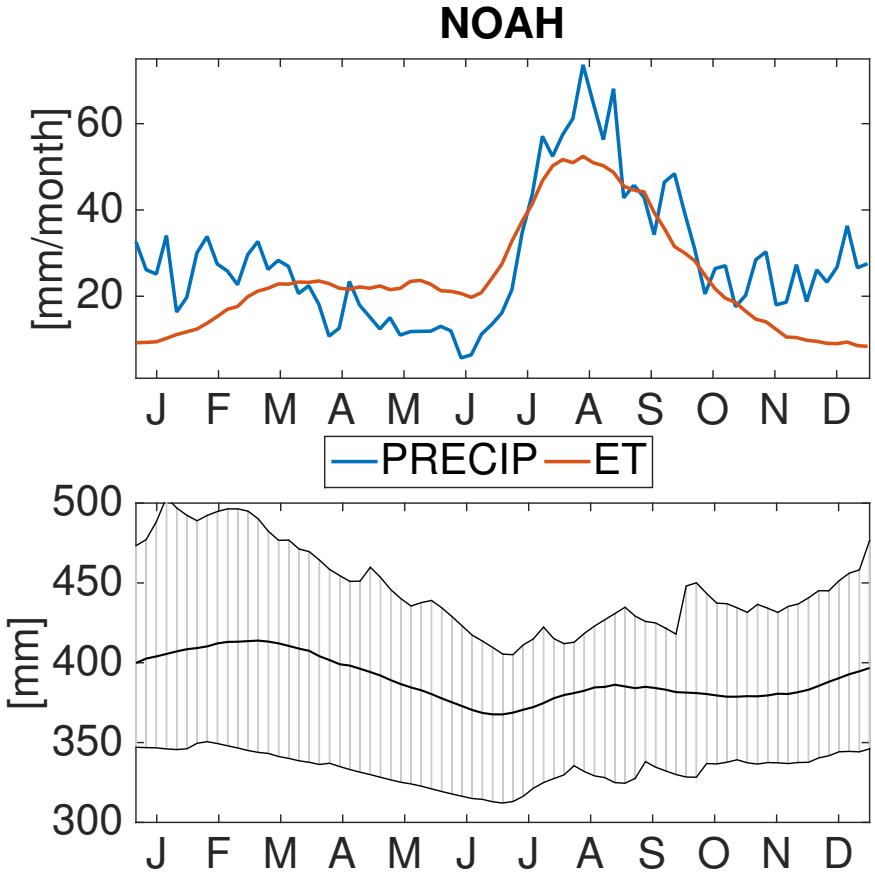

Figure 26: Seasonal cycle of the bimodal region for precipitation and evapotranspiration (ET) (top panels) and soil moisture (0-200 cm) (bottom panels) for NLDAS-2 Noah time averaged from 1979 to 2017. Shading on soil moisture indicates the variability over the years averaged.

3.3.6 Decadal shifts

We examine two periods over the last three decades: 1979 to 1997, and 1999 to 2017. These periods are selected based on the climate shifts observed over the tropical Pacific which are known to have implications for the SWUS (Zhang et al. 1997; Mantua et al. 1997). We also ensure both periods are of equal length (19 years), and select 1979 to 1997 to capture the particularly wet year 1979. The recent dry period is chosen to start in 1999 as this excludes the wet year 1998 (resulting from the 1997/98 El Niño), and captures the more severe dry years of the recent period. We end the period in 2017 to ensure complete years of data, but note that this drought is ongoing in 2018.

However, since GIMMS NDVI begins in 1981, it is averaged over the bimodal region for 1981 to 1997, and 1999 to 2015 (Figure 27). NDVI is significantly lower during March to July in the later decades: using a Student's t-test significant at $\alpha = 0.05$, we compared the distribution of NDVI values in each period and found the distributions to have different means for all months from March to July. There is no significant decline in the later summer months in NDVI. A slight shift to later start in green-up is also observed in later decades for the mean seasonal cycle, with green-up starting in mid-February for 1999-2015 compared to early February (1981 - 1997) (Figure 27). However, this delayed green-up start is found not to be significant when we test the distribution of green-up start times in either period (using a Student's t-test we find $t = 1.06$, $p = 0.29$).

Seasonal cycles of rain, snow fall, total runoff, snow melt, soil moisture (0 to 200 cm), ET, the ratio of snow to total precipitation and SWE from NLDAS-2 Noah are shown in Figure 28. The seasonal cycles are averaged over the same two time periods: 1979 to 1997, and 1999 to 2017. A drying is observed in each of these quantities for the later decades. Rain is reduced in the winter-spring, but no significant change occurs during the summer monsoon season. SWE and snow melt

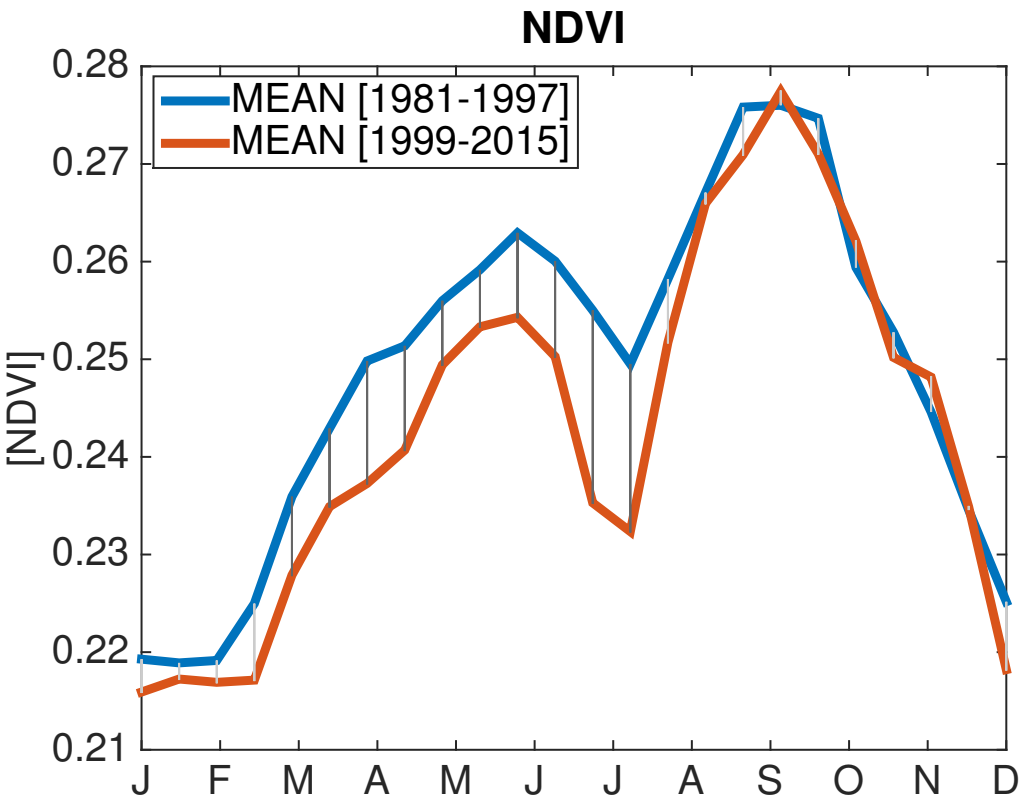

Figure 27: Seasonal cycle of GIMMS NDVI area averaged over the bimodal precipitation region (indicated in Figure 21). The seasonal cycles for two different decadal periods are shown: 1981 - 1997 and 1999 - 2015. Vertical solid black lines indicate the difference is significant (using a Student's t-test at a 0.05 significance level to each half-month distribution from the different periods), and dotted lines indicate difference is not significant between the two periods.

are also reduced in the later decades. Soil moisture also declines and shifts to an earlier spring minimum in the later decades. The mean minimum occurs on average one week earlier in the later decades, but this earlier timing is not significant when testing the timing for the distribution of years from either period (using a Student's t-test we find t = 0.29, p = 0.78).

To place these changes in the SWUS region in the context of planetary scale Pacific decadal variability, the continent-wide spatial patterns of our two periods of interest are shown in Figure 29 for annual average precipitation, ET, total runoff, snow melt, soil moisture (0 to 200 cm), air temperature, along with Pacific-North America patterns of detrended SST and 200mb geopotential height. Drying in the later decades is apparent across the SWUS for each of these variables, as well as a widespread increase in temperature across much of the continental United States. This pattern of drying during the later decades is consistent with the tropical Pacific influence on winter precipitation in the SWUS (Delworth et al. 2015; Seager and Vecchi 2010b; Mantua et al. 1997; Huang et al. 2005). After the 1997/1998 El Niño, there was a shift to cooler SST and low geopotential heights over the tropical Pacific and positive 200mb geopotential height anomalies over the west which cause the drying (Delworth et al. 2015; Seager and Vecchi 2010b; Flavio et al. 2018). The same patterns associated with the Pacific are apparent for the mid-century drought (see Appendix Figure A1 below).

We create a metric of spring drying based on soil moisture from Noah and SM-MCDI (Figure 30, top panel). We define the length of the dry season as the period of drying between the winter maximum in soil moisture and the spring minimum, before recovery with summer precipitation. We use the deeper depth (0 - 200cm) soil moisture for Noah to be consistent with the SM-MCDI. No significant trend in the duration of the dry season is detected during 1979 to 2017 (based on results of a Mann Kendall significance test we find τ = 8.22, p = 0.30 and τ = -75.79, p = 0.83 for

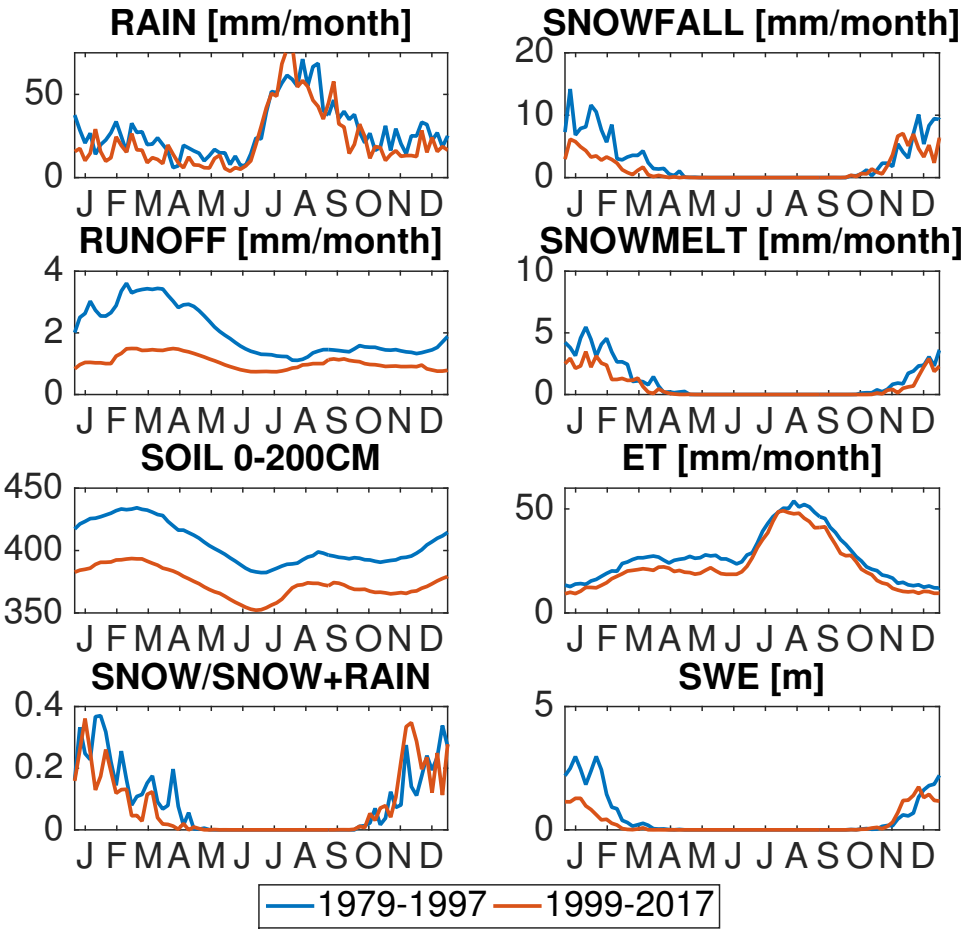

Figure 28: NLDAS-2 Noah seasonal cycle of the bimodal region showing decadal shift of hydrological variables for wet decades (1979-1997) and dry decades (1999-2017) for a) rain, b) snow fall, c) total runoff, d) snowmelt, e) soil moisture (0 - 200cm), f) ET, g) the ratio of snow to total precipitation, and h) SWE.

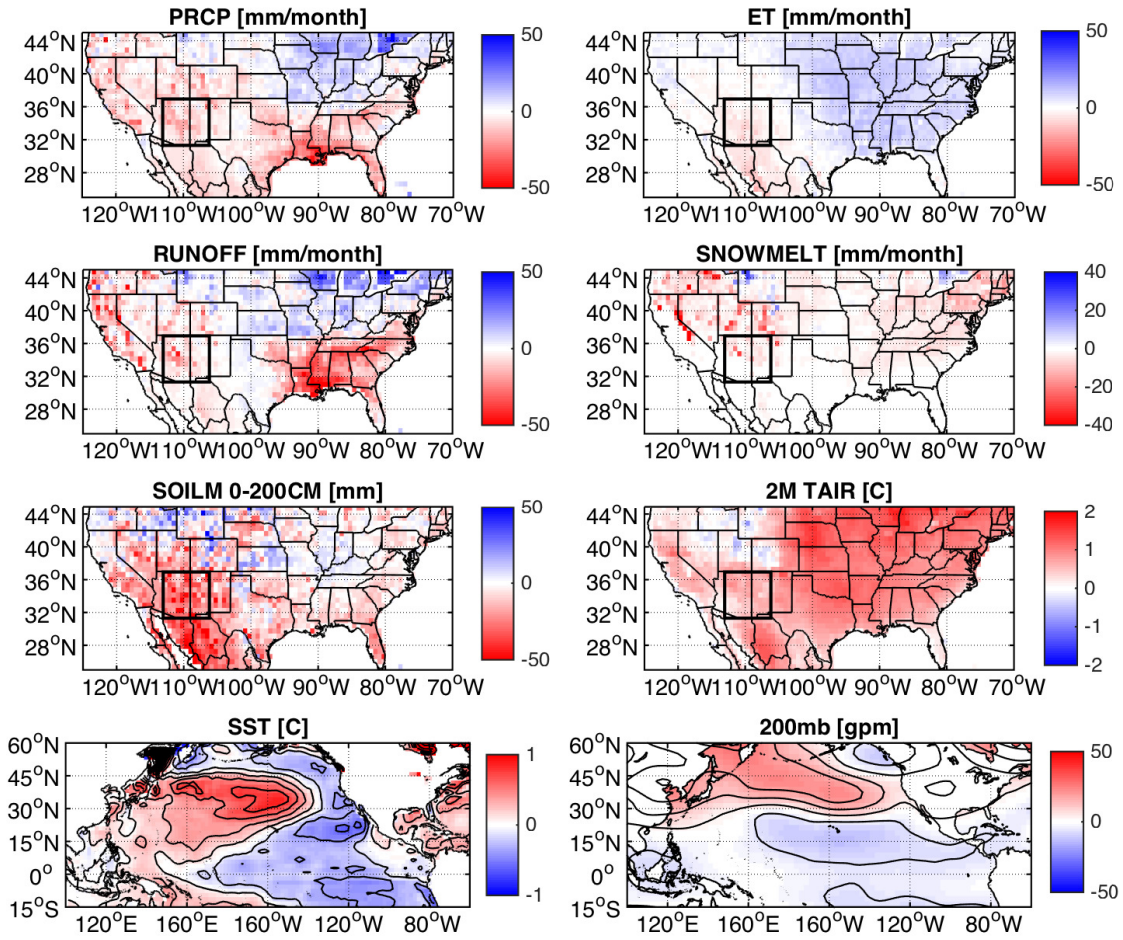

Figure 29: Maps showing difference in annual average for hydrological variables between dry decades (1999-2017) minus wet decades (1979-1997) for a) NLDAS-2 precipitation forcing, b) Noah ET, c) Noah total runoff, d) Noah snowmelt, e) Noah 0-200 cm soil moisture, f) NLDAS-2 temperature forcing (2 m level). For large-scale dynamical context g) shows NOAA NCEP-NCAR Reanalysis detrended SST, and h) NOAA NCEP-NCAR Reanalysis detrended 200mb geopotential height. Contours are plotted at 0.25C intervals for SST, and at 20m intervals for geopotential height.

Noah and SM-MCDI respectively).

For the soil moisture minimum, for 1979 to 1997 the average minimum occurs during the second week of July, and for 1999 to 2017 the minimum occurs in the first week of July (Figure 30b). This shift toward earlier spring is found to be significant for the average of Noah and SM-MCDI (based on results of a Mann Kendall significance test with τ = -3.50, p = 0.01). However, individually, only SM-MCDI has a significant trend toward an earlier spring soil moisture minimum.

Examining the average trend for the winter soil moisture peak in Noah and SM-MCDI, we find that from 1979 to 1997, the average peak is the third week of February, and for 1999 to 2017, the first week of February (Figure 30c). However this trend towards an earlier peak is not significant (based on results of a Mann Kendall significance test with τ = -6.53, p = 0.19).

The earlier spring minimum is consistent with less total moisture being delivered to soils in the winter and spring, and hence a faster drying out of the reduced available moisture. The lack of trend in the duration of the dry season is consistent with both the winter peak and spring minimum shifting to earlier in the year.

3.3.7 Simple soil moisture balance model

To better understand the processes responsible for the decadal differences in soil moisture we relate the change in soil moisture ($\frac{dS_m}{dT}$) to rain (P_{rain}), snow melt (S_n), ET (ET) and runoff (R_o) using the following:

$$\frac{dS_m}{dt} = \frac{S_{m_t+1} - S_{m_t-1}}{\Delta t} = P_{rain} + S_n - ET - R_o \quad (1)$$

We use the seasonal cycles of P_{rain}, S_n, ET and R_o in the bimodal SWUS region from NLDAS-

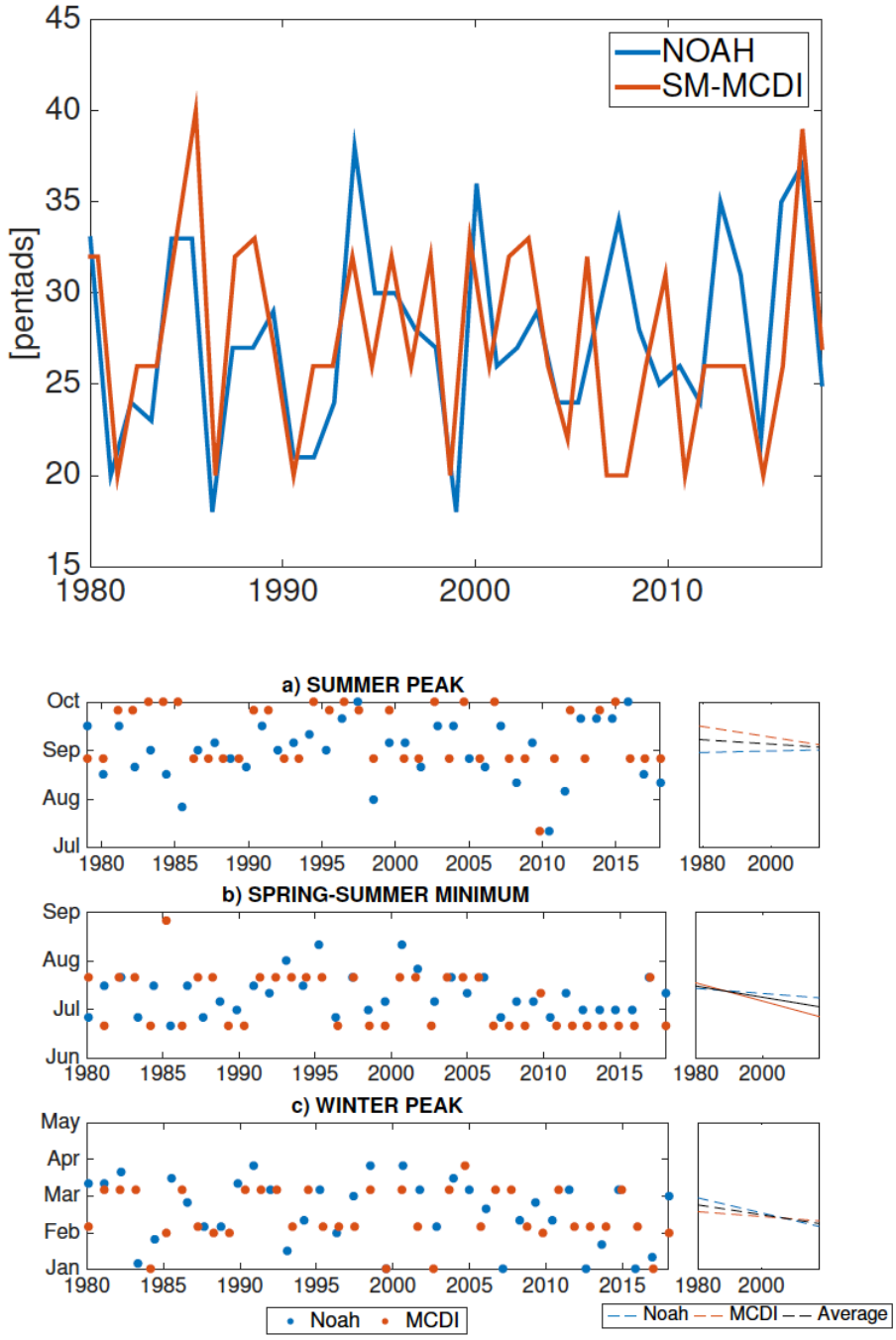

Figure 30: Top: Timeseries of the duration in the spring drying period for NLDAS-2 Noah (0 - 200cm) and SM-MCDI (0 - 200cm). The spring dry season duration is defined as the time between soil moisture winter peak to spring-summer minimum and is plotted in 5 day means (pentads). Bottom: the timing of the summer soil moisture peak (a), spring-summer minimum (b) and winter peak (c) (left column), with linear trend (right column). We use the deeper available soil moisture levels from the models as these exhibit less year-to-year variability and provide more consistent results in timing across models. Solid (dashed) lines indicate that trends are significant (insignificant) (using a Mann Kendall significance test at $\alpha = 0.05$).

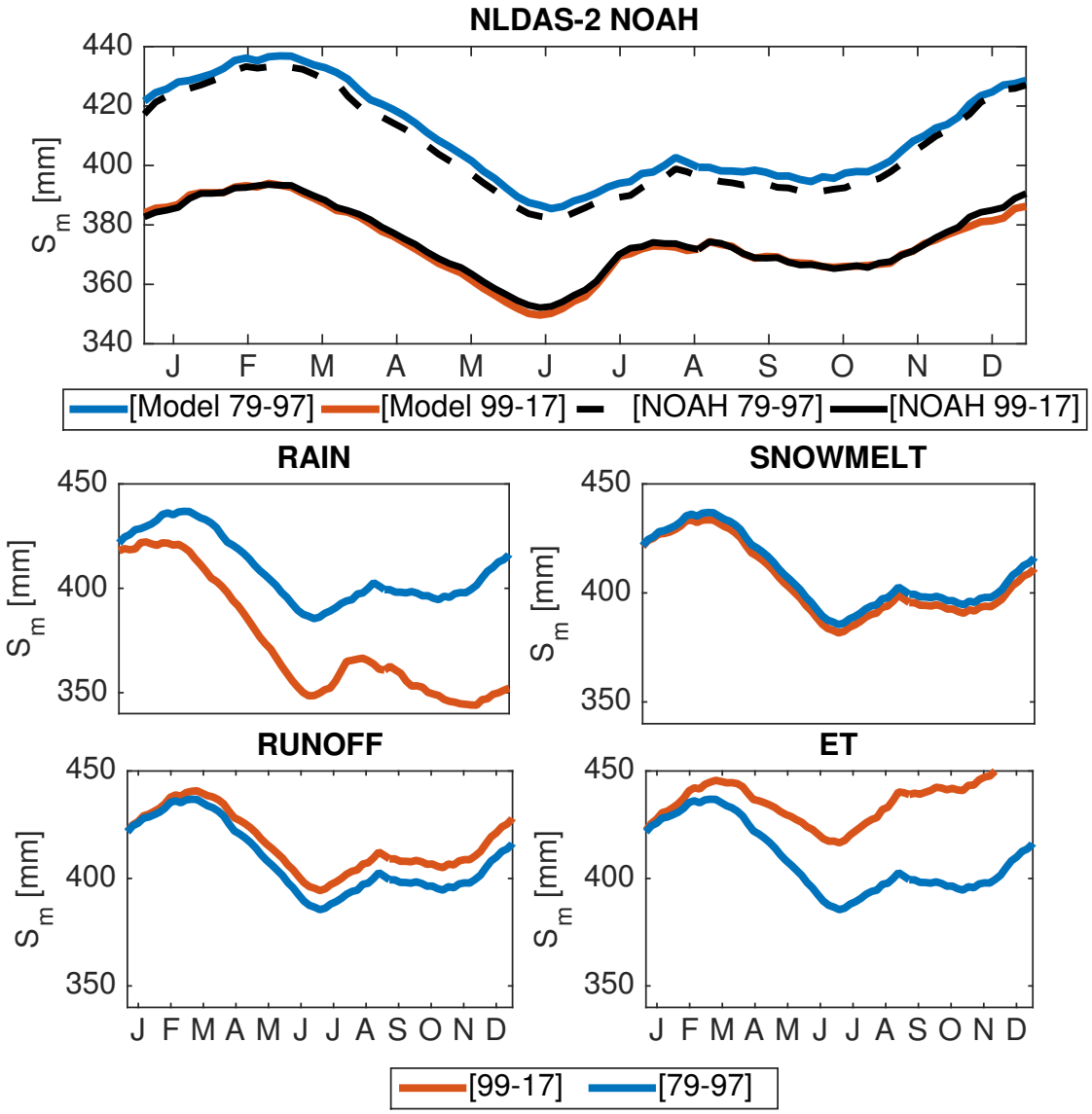

Figure 31: Top: Simple model for soil moisture (0 - 200cm) in the bimodal region run for the wet decades (1979-1997) (blue line) and dry decades (1999-2017) (red line). The simple model calculates soil moisture from the balance of rain, snow melt, ET and runoff. The simple model is compared with NLDAS-2 Noah soil moisture for either period. Bottom panel: contribution of each variable from the simple model to the observed drying from earlier to later decades. The model is run using the dry decades (1999-2017) value of one variable at a time (for each of rain, snow melt, ET, runoff) and wet decades (1979-1997) values for other variables. This is compared with the modeled wet decades soil moisture.

2 Noah output to calculate $\frac{dS_m}{dT}$ at each 5-day time step using values from the wet decades (1979 to 1997) and the dry decades (1999 to 2017) (Figure 31, top panel). The results of the soil moisture balance model are compared with Noah 0 - 200 cm soil moisture for each of these two decades. We use this deeper depth as it produces the best agreement with the output from our simple model, and is also consistent with the depth of the SM-MCDI soil moisture that we analyze. Like the 0 - 100 cm soil moisture layer, the 0 - 200 cm has more muted and later winter and summer peaks than the 0 - 10 cm, but still has a clear connection with vegetation green-up and decay in the spring and summer. The calculated soil moisture from the simple model generally agrees with the output from NLDAS-2 Noah in either decadal period.

We then decompose the change in soil moisture balance into contributions from P_{rain}, S_n, ET and R_o (Figure 31, bottom panels). Rain and snowmelt from the later decades drive the observed soil moisture decline, with rain producing the greatest change. This is consistent with the fact that much of the study region is mostly dominated by rain, and just a subset of the northern sites have snow cover during the winter. Rain also produces the observed shift to an earlier spring dry period. From the point of view of soil moisture, reductions in runoff and ET are then offsetting responses arising from the reduced soil moisture availability.

3.3.8 Contrasting the 1948-1966 and 1999-2017 droughts

The decadal shift to drier conditions in recent decades need not be due to long term climate change. Decadal variability is strong in this region of the SWUS, as evidenced in the SM-MCDI soil moisture extending back to 1948 (Figure 32). We focus on 1948 to present due to the greater accuracy of climate data and availability of comprehensive atmospheric Reanalysis in the second half of the 20th century. For the mid-century drought, we select the years 1948 to 1966 so that we

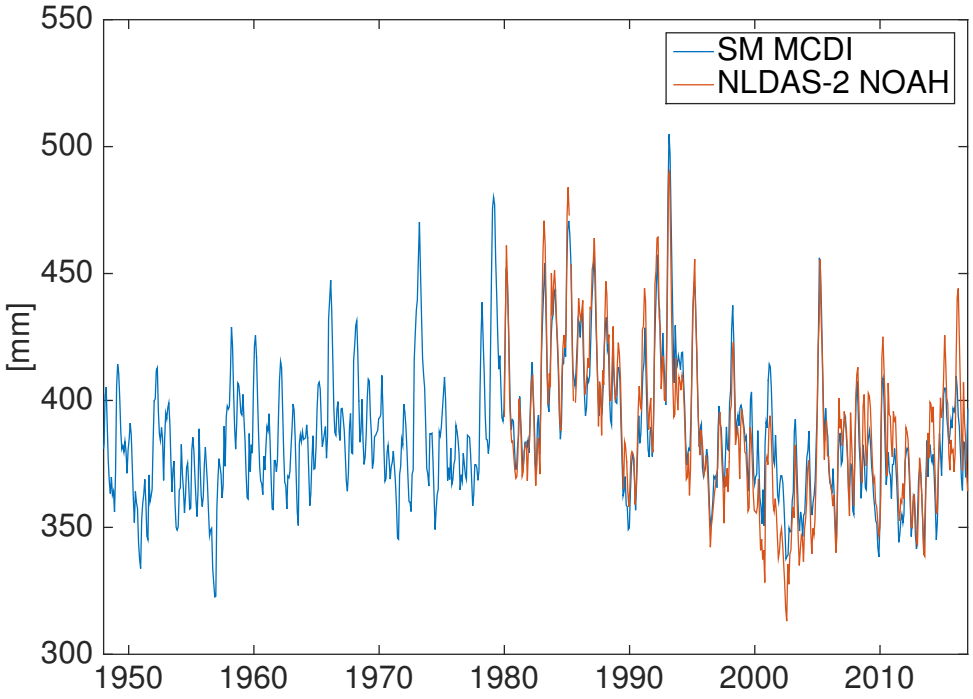

Figure 32: Timeseries of 0 - 200 cm soil moisture for NLDAS-2 Noah (monthly) and SM-MCDI soil moisture (monthly) (Williams et al. 2017).

are capturing the driest years during the mid-century period, and also so that we are contrasting two time periods of equal length (19 years).

The drought of the 1940s and 1950s is prominent in the historical timeseries, with soil moisture values falling almost as low as the current period of drying (1999-2017). This drought in the SWUS is well documented, and is associated with tropical Pacific SST anomalies and a ridge over the SWUS (also see Appendix Figure A1) (Seager et al. 2005b; Cook et al. 2011a). It appears amid an extended mid-century dry period that continues until the late 1970s and is also related to cool tropical Pacific SSTs (Huang et al. 2005).

Based on the SM-MCDI soil moisture, we find that soil moisture was lower in the more recent drought throughout the year compared to the 1940s/50s drought (Figure 33). This is hard

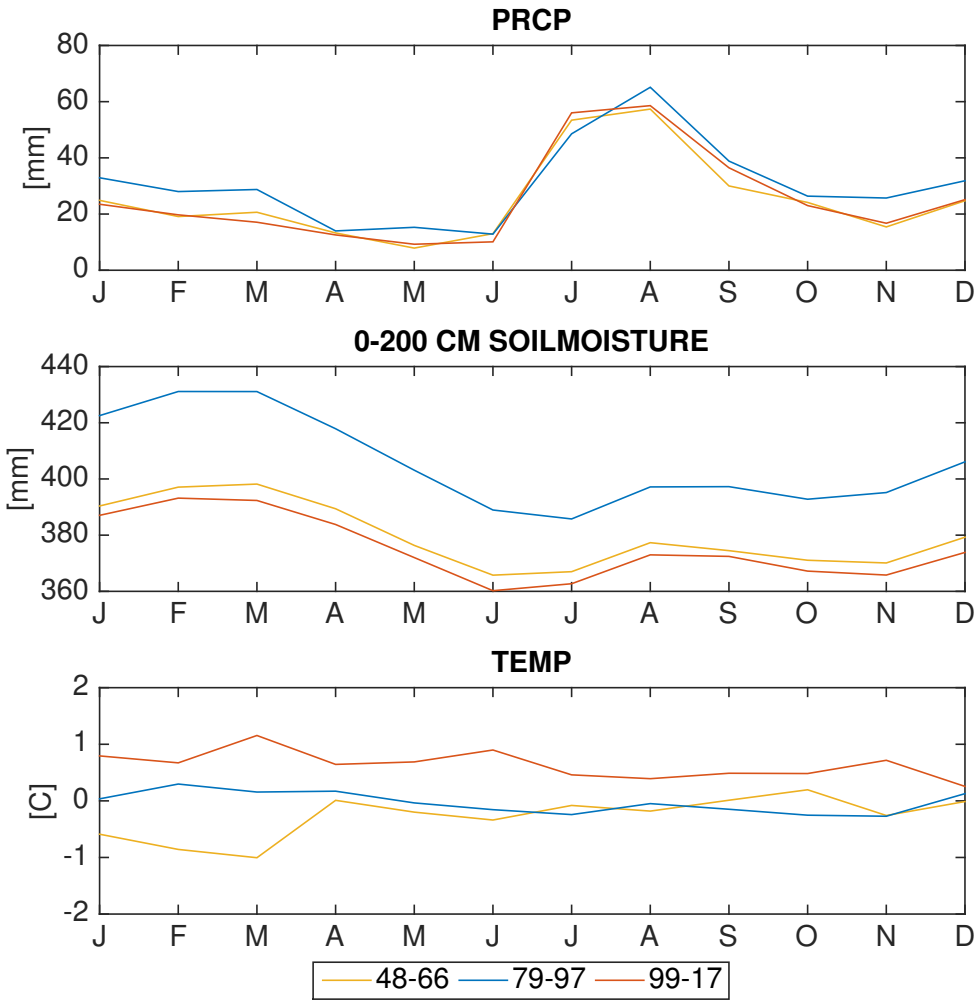

Figure 33: Seasonal cycle of the bimodal region showing decadal shift of hydrological variables: a) CLIMGRID precipitation (top panel), b) soil moisture (SM-MCDI) (middle panel), and c) CLIMGRID temperature seasonal cycle anomaly (anomaly based on 1948 - 2017 period) (bottom panel). For each of the variables we plot the average seasonal cycle from wet decades (1979-1997) and dry decades (the earlier dry period in 1948-1966 and the later period in 1999-2017).

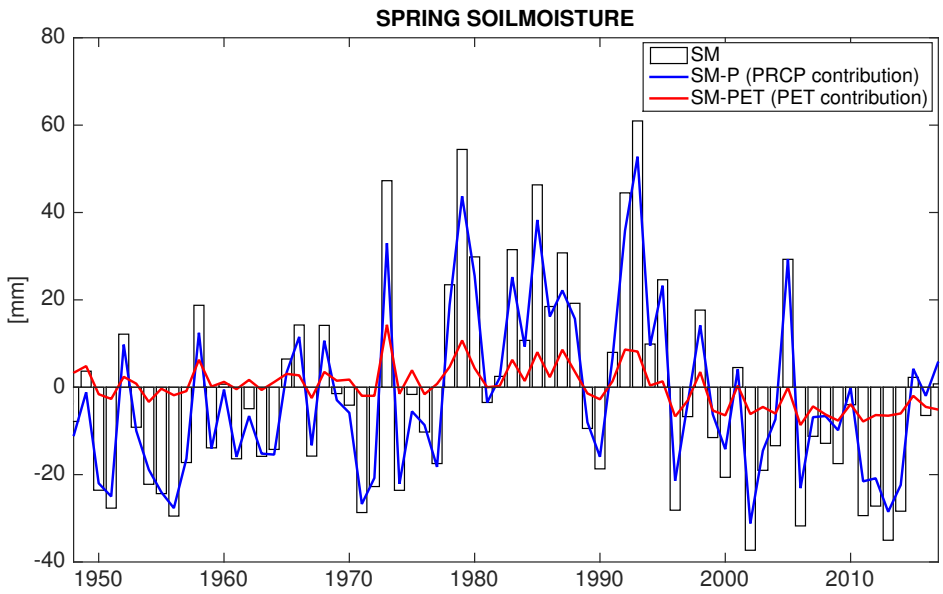

Figure 34: Decomposition of spring (AMJ) soil moisture to show the contribution of potential evapotranspiration (PET) (red line) and precipitation (SM-P) (blue line) to soil moisture anomalies (SM) (bars) for the SWUS bimodal region. Anomalies are calculated based relative to the 1921-2000 mean.

to explain in terms of a precipitation decrease given the small difference between precipitation in the mid-century and recent drought (Figure 33, top panel). The lack of explanatory power from precipitation change has also been noted in a study contrasting droughts in the Upper Colorado River Basin during the 20th century (Woodhouse et al. 2016). The temperature anomalies show more striking decadal changes, with the most recent drought having greater temperatures in each month of the year, compared to both the previous drought and the 1979-1997 wet period (Figure 33, bottom panel).

In light of warming temperatures in the region, we use the SM-MCDI soil moisture to investigate specifically the role of evaporative demand in each drought. In Figure 34 the spring (AMJ) SM-MCDI soil moisture is plotted as an anomaly relative to the 1921-2000 mean (bars) and is then decomposed to show the contribution of precipitation (SM-P, blue line) and PET (SM-PET, red

line). SM-P is forced by precipitation only, holding PET at its mean annual cycle for 1921- 2000. The difference between SM-MCDI and SM-P (SM-MCDI minus SM-P) is the effect of PET on soil moisture (SM-PET) (Williams et al. 2017). For the mid-century drought (1948 - 1966) PET contributed to 6% of the negative soil moisture anomaly, and for the recent drought (1999 - 2017), PET contributed to 39% of the soil moisture anomaly.

This analysis indicates the heightened role of temperature in exacerbating drying during the more recent drought despite similar precipitation amounts. This finding is consistent with the shift to warmer temperatures in the region throughout the year (Figure 33). As such, warming and higher evaporative demand lead to lower soil moisture in the most recent drought than in the prior drought, despite similar reductions in precipitation.

3.4 Discussion and Conclusions

3.4.1 What mechanisms produce the observed seasonal cycle of i) bimodal vegetation, ii) the intervening spring dry season?

A bimodal annual cycle of regional vegetation greenness in the SWUS arises from a combination of i) winter precipitation, which adds moisture to the soils, and which is subsequently drawn down in spring by enhanced ET due to transpiration and bare-soil evaporation, and ii) NAM rainfall during the summer. The existence of vegetation bimodality here, therefore, is because the region lies both sufficiently far north to be affected by the winter storm track and sufficiently far south to be affected by the summer monsoon. Although annual precipitation totals are dominated by the NAM, soil moisture storage during the summer months is smaller. This is due to both high levels of non-infiltrating runoff during the summer, as well as high rates of ET. The dry season, which lies

in between winter precipitation and the NAM, is characterized by a drying of soils and a decline in vegetation growth. Consistent with previous studies, we also find a clear negative connection between spring soil moisture and vegetation green-up (Notaro et al. 2010; Muldavin et al. 2008)

3.4.2 How has the hydroclimate of the spring dry season changed on decadal timescales and how has this influenced the magnitude, timing and duration of the spring dry season?

From 1999 to 2017, the spring dry season has become significantly drier and has shifted to earlier in the year compared to an earlier wet period (1979-1997), as represented in the NLDAS-2 Noah model and SM-MCDI soil moisture. This climatic shift in the SWUS is associated with the change from warmer to cooler SSTs in the tropical Pacific (McCabe et al. 2004; Mantua et al. 1997; Huang et al. 2005). Observed impacts include earlier timing of the soil moisture spring minimum, which we find is significant across the average of Noah and SM-MCDI. There is also a tendency towards earlier winter soil moisture maximum (however this is found to not be significant) with the result of shifting the dry season to earlier in the year. The earlier spring minimum is associated with a more rapid drying and resultant quicker achievement of very low soil moisture levels.

Another impact of this climatic shift is the observed significant shift to lower vegetation productivity in this region since 1999, according to GIMMS NDVI data, and consistent with previous studies (Notaro et al. 2010; Muldavin et al. 2008; Williams et al. 2012). This is associated with the reduction in winter-spring precipitation, which is critical for adding moisture to soils, and providing water for spring vegetation green-up. The smaller change in summer precipitation in the region has also meant that summer vegetation green-up has been relatively unchanged in 1999 - 2015 compared to 1981-1997.

Analysis of twentieth-century soil moisture (SM-MCDI), in conjunction with known periods of

drought and pluvials in the mid twentieth-century (Seager et al. 2005b; Cook et al. 2011a), indicate that this decadal variability in spring drying has been prevalent throughout the past century in the SWUS. During the mid-century drought the driest years in the 1950s were almost as severe as the recent drought, and both are largely attributed to cool tropical Pacific SSTs (Seager et al. 2005b; Seager and Vecchi 2010b; Delworth et al. 2015), while the wetter period from 1979 to 1997 is associated with warm SSTs (McCabe et al. 2004; Mantua et al. 1997; Huang et al. 2005; Pascolini-Campbell et al. 2017, 2015). Natural decadal variability in the region is therefore dominated by Pacific SST conditions (Flavio et al. 2018).

3.4.3 How are these decadal changes expressed in terms of the interaction of precipitation, snowmelt, ET, runoff, soil moisture and vegetation? Is there an influence of warming temperatures?

The lower magnitude and earlier average spring soil moisture minimum, are attributed to reduced winter precipitation, more precipitation falling as rain rather than snow during the winter, and earlier snowmelt. Earlier snowmelt in the west has also been well established in the literature (Barnett et al. 2008; Mote et al. 2018). The impact of earlier melt is more important in the northern portion of the study region which receives greater amounts of snow cover at elevation during the winter months. The dominant mechanism arises from the overall decrease in winter precipitation, which contributes to drying out of the soil moisture column earlier in the year as less moisture is initially available. Implications of this also include a reduction in runoff and ET, and a shift to lower spring vegetation productivity, which respond to the magnitude of moisture in the system.

Temperature increases and greater PET during the more recent period were found to enhance drying and soil moisture decline compared to the mid-century drought. The role of PET in soil

moisture drying increased from 6% for 1948-1966 to 39% in 1999-2017. This finding suggests that continued rising temperatures will exacerbate soil moisture drying in this region.

Nonetheless, precipitation plays the dominant role in spring drying for both the mid-century and recent drought. During the earlier period (1979 to 1997), 25% of precipitation fell as snow during January-February, compared to 15% during 1999 to 2017 consistent with warming. Winter rainfall reduction is also responsible for shifting the spring soil moisture minimum to earlier in the year due to an earlier drying out of stored water content. Changes in winter precipitation in the decades we analyze are consistent with climate shifts in tropical Pacific SSTs.

3.4.4 Ecological Implications

Our study indicates that to date precipitation in the winter-spring has been the dominant mechanism impacting drying. Precipitation in turn is strongly associated with tropical Pacific SST, and future decadal variability of the Pacific will be critical for controlling the dynamics of the spring dry season in the future. Given the relationship between winter precipitation, soil moisture and spring vegetation (Notaro et al. 2010; Vivoni et al. 2008; Robinson et al. 2013), future changes in winter precipitation due to the combined effects of natural decadal variability and emerging forced spring drying, could have negative consequences on ecosystem productivity.

Despite the dominant role of precipitation, we also detected a heightened role of temperature in the recent post 1999 drought compared to the mid-century drought. This has important implications in light of projected temperature increases. Anthropogenic climate change in the SWUS is projected to intensify aridification (Seager et al. 2007), particularly during the spring (Gao et al. 2014; Ting et al. 2018). The influence of natural changes in precipitation will occur against a background of enhanced PET due to higher temperatures in the future. However, if the tropical Pacific

returns to warm or neutral conditions (e.g. Ramesh et al. (2017)) then this would introduce a tendency to a wetter winter and a later onset and wetter spring dry season that would work against the human driven trend towards drying.

Other impacts include the response of vegetation to CO_2 fertilization, in which increased amounts of atmospheric CO_2 enhance vegetation growth (Milly and Dunne 2016). Analyzing projections of the 21st century with an Earth System Model, the SWUS was found to become both greener and drier (Mankin et al. 2017). Future research questions could focus on whether the model-projected enhanced spring drying will be offset by physiological effects of CO_2 on ecosystems in this region. Greater vegetation cover could also have the effect of enhancing water losses through ET in the spring and early summer, reducing soil moisture and runoff (Mankin et al. 2017, 2018a).

A changing climate may also impact ecosystems in other indirect ways. Warming has contributed to greater outbreaks of bark-beetles and wildfires in the western United States (Abatzoglou and Williams 2016; Westerling et al. 2006; Penelope et al. 2008; Raffa et al. 2008), both of which enhance tree mortality (Williams et al. 2012). Our study has found a reduction in moisture during the spring, in addition to warmer summer temperatures. Warming and reduced soil moisture increase the vapor pressure deficit (VPD), the difference between the water vapor content of the air and the saturation value, a quantity observed to correlate strongly to annual forest fire area in the western United States (Seager et al. 2015; Williams et al. 2015b). Changes in moisture, temperature and VPD could all increase susceptibility of trees to bark-beetle infestation and wildfire in the future.

Finally, a reduction and advance in the timing of peak runoff in the spring due to earlier snowmelt has been identified for western rivers (Stewart et al. 2005; Regonda et al. 2005). En-

hanced winter and spring drying in the future could also contribute to reduced and earlier streamflow peaks for this region, as suggested by observational studies on the increasing role of temprature (Woodhouse et al. 2016; Barnett et al. 2008), and hydroclimate projections (Seager et al. 2013; Barnett et al. 2008; Mankin et al. 2017; Ting et al. 2018). Reduced streamflow would be harmful to riparian ecosystems (Jaeger et al. 2014; Perkin and Gido 2011). River fragmentation is particularly deleterious to fish breeding which rely on flowing waters as part of their spawning process, and due to the impacts of fish being trapped in anoxic and stagnant river segments (Perkin and Gido 2011; Dudley and Platania 2007). Summer temperatures could potentially also lead to greater ET, reducing the summer streamflow peak in the future.

Given the sensitivity of this SWUS region to climate change, and the implications on ecosystems, wildfire, and streamflow, improved understanding of the mechanisms tying together the climate, hydrological and ecological systems is important for explaining past and future environmental variability and change.

4 Dynamics and variability of the spring dry season in the United States Southwest II: CMIP5 projections

4.1 Introduction

A previous study has shown that spring drying in the Southwest United States (SWUS) is primarily controlled by the magnitude of winter-spring precipitation, which is influenced by natural climate variability (Pascolini-Campbell et al. submitted). The severity of this drying has become more severe in the most recent drought (1999 to present), and has been exacerbated by increasing temperature in the region since the 1950s (Pascolini-Campbell et al. submitted). Implications of this drying include less available moisture for spring vegetation green-up, enhanced wildfire activity and dust emissions. Building on our understanding of how climate dynamics influence hydroclimate and ecosystems in this area, we explore 21st century climate projections using output from the Coupled Model Intercomparison Project Phase 5 (CMIP5) (Taylor et al. 2011) to assess future changes to the region.

We focus on a region of the Southwest United States (SWUS) which has two main seasons of precipitation and vegetation green-up: one from the winter storm track, and one from the North American summer monsoon (NAM). This bimodal region also has an intervening dry period of vegetation senescence during the spring. The SWUS is projected to become warmer and more arid in upcoming decades (Seager et al. 2007), as well as greener due to the effects of CO_2 fertilization (Mankin et al. 2017). The impact of higher temperatures and enhanced vegetation growth will affect both the hydroclimate and ecosystems in this moisture-sensitive region. In light of projected temperature and aridity increases, it is critical to examine how these changes will be reflected in

hydroclimate, ecosystem vitality, runoff and spring drying.

The dynamics of this region in the observational record have been explored in a previous study (Pascolini-Campbell et al. submitted). The timing and magnitude of the spring drying which occurs between the winter and summer wet periods are primarily controlled by winter-spring precipitation, which adds water to the soils providing moisture for the vegetation green-up (Pascolini-Campbell et al. submitted; Notaro et al. 2010; Muldavin et al. 2008). The amount of water added during the winter-spring in the form of rain or snowmelt also controls the timing of the spring minimum: a reduction in the initial water stored in soils and leads to more rapid soil drying due to plant growth and evapotranspiration (ET) losses.

The region is also characterized by natural decadal variability associated with sea surface temperatures (SSTs) in the Pacific: phases of cool (warm) SST produce drying (wetting) in the SWUS (McCabe et al. 2004). However, the most recent drought in the observational record cannot be explained by precipitation anomalies associated with Pacific variability alone. Warming temperatures in the region since 1948 have enhanced drying out of soil moisture during the spring (Pascolini-Campbell et al. submitted). The heightened role of temperature has also been detected in a study contrasting twentieth-century droughts for the upper Colorado River basin (Woodhouse et al. 2016). It follows that warming in the future has serious implications on the timing and magnitude of the dry season (Pascolini-Campbell et al. submitted), vitality of ecosystems, and for streamflow (Stewart et al. 2005; Regonda et al. 2005).

Modeling studies have noted a shift toward more arid conditions in the southwest in the 21st century (Seager et al. 2007), particularly during the spring (Gao et al. 2014; Ting et al. 2018). In addition to concerns over changing hydroclimate, increased atmospheric CO_2 in the coming century has been projected to enhance greening in the southwest (and elsewhere) via fertilization

(Mankin et al. 2017, 2018a), which may offset declines in vegetation from moisture limitations. Greater vegetation cover could also have the effect of enhancing water losses through ET in the spring and early summer, reducing soil moisture and runoff (Mankin et al. 2017, 2018a).

This study aims to investigate projections for this region by first i) identifying members of the CMIP5 ensemble which most accurately capture the climate of the bimodal region, and ii) investigate projections for the 21st century in this model subset. This study will help provide insights on how aridity and vegetation changes will impact the region given anthropogenic warming.

4.2 Data and Methods

We analyze monthly output from 18 CMIP5 models (the subset is based on availability of monthly precipitation, net primary production (NPP) and soil moisture, which we use in our evaluation) (Table 6). We use the historical runs (available from 1861 to 2005) and the Representative Concentration Pathway 8.5 (RCP8.5) emissions scenario for future projections (2006 to 2099). For validation, we focus on the period 1979 - 2015 (by combining the historical and RCP8.5 runs). We then analyze projections for 2021 to 2099.

The CMIP5 models are validated against observations and land surface model output (listed in Table 7). We use Parameter-elevation Regressions on Independent Slopes Model (PRISM) precipitation for the period 1979 to 2015 ((Daly et al. 2008b) available online at: http://prism.oregonstate.edu). The second phase of the National Land Data Assimilation system (NLDAS-2) land surface models (LSMs) Noah, Mosaic and VIC (Xia et al. 2015) are also used for validation. From the LSMs we use Noah leaf area index (LAI), and soil moisture 0 - 100 cm for Noah, Mosaic and VIC. We use LAI from only the Noah model given its superior performance in simulating the bimodal re-

Table 6: Summary of CMIP5 models used

Model	Resolution
BCC_CSM1.1	T42, L26
BCC_CSM1.1(m)	T106, L26
BNU-ESM	T42, L26
CanESM2	T63 (1.875^o x 1.875^o), L35
CESM1-BGC	0.9^o x 1.25^o, L53
CESM1-CAM5	0.9^o x 1.25^o, L53
GFDL-ESM2G	144 x 90 (2.5^o x 2.0^o), L24
GFDL-ESM2M	144 x 90 (2.5^o x 2.0^o), L24
GISS-E2-H	2.5^o x $2.0\ ^o$, L40
GISS-E2-R	2.5^o x $2.0\ ^o$, L40
HadGEM2-CC	1.25^o x 1.875^o, L38
HADGEM2-ES	1.25^o x 1.875^o, L38
IPSL-CM5A-LR	(96 x 96) 3.75^o x 1.875^o, L39
IPSL-CM5A-MR	(144 x 144) 2.5^o x 1.25^o, L39
MIROC-ESM	T42, L80
MIROC-ESM-CHEM	T42, L80
NorESM1-M	144 x 96 (2.5^o x 1.875^o), L26
NorESM1-ME	144 x 96 (2.5^o x 1.875^o), L26

Table 7: Summary of other data sets

Dataset	Temporal Availability	Resolution	Variable
NLDAS-2	1979 - 2018	$1/8\text{th}^o$, hourly	Soil moisture
Noah, Mosaic, VIC			0 - 10cm
PRISM	1895 - 2018	$1/24\text{th}^o$, monthly	Precipitation
Ameriflux	2006 - 2014	site, half-hourly	NEE

gion when compared with satellite and flux site observations (Pascolini-Campbell et al. submitted). This output is available in daily resolution, at 1/8th-degree spatial resolution, however we create monthly averages for comparison with the CMIP5 output.

We use net ecosystem exchange (NEE) from stations in the Ameriflux observing network that lie within the SWUS study region (available online at: http://ameriflux.lbl.gov) (Figure 35). NEE is the total respiration (autotrophic plus heterotrophic) minus net primary production (NPP) and reflects ecosystem exchange of carbon with the atmosphere. We use NEE to evaluate the seasonal cycle of NPP in CMIP5 models, and although it is not the same quantity, we are primarily interested in the seasonality, and these in general agree between the two measurements. The Ameriflux network uses eddy covariance methods to make half-hourly temporal resolution estimates of the fluxes of ecosystem CO_2, water and energy in North America (Baldocchi et al. 2001).

4.2.1 Metrics used for model selection

We use two metrics: one that assesses the spatial representation of the simulation of the bimodal region, and one that evaluates the average seasonal cycle area-averaged over the bimodal region (which is previously identified in Pascolini et al. [submitted]).

First, we create maps from observations and NLDAS-2 output which identify where the seasonal cycle averaged between 1979 to 2015 has both a winter and summer peak (hereafter referred to as 'reference maps'). These maps are created for i) PRISM precipitation, ii) NLDAS-2 Noah LAI, and ii) NLDAS-2 (Noah, Mosaic, VIC) 0-100 cm soil moisture. The method of identifying the two peak region is discussed in Pascolini et al. [submitted]. There, using NLDAS-2 and Ameriflux data, bimodality is found in precipitation, soil moisture and NPP. The bimodal region for precipitation is shown in Figure 35, and the box shown indicates where we area-average to find

the average seasonal cycle (31^oN to 37^oN, -111^oW to -106^oW) .

We also create maps for each of the 18 CMIP5 models which identify where the average seasonal cycle from 1979 to 2015 (by combining historical runs and RCP8.5) has a bimodal winter and summer peak in precipitation, NPP and upper column soil moisture. In each case, the CMIP5 model is regridded to the same resolution as the maps from the observations and NLDAS-2 output.

For the bimodal region within the boxed area (Figure 35), from the observed map of two peaks, we identify the number of grid points within this box that the CMIP5 also correctly classifies as having two peaks. This number is then divided by the total number of two peak grid points from the reference maps. This gives a possible score of 0 (no grid points correctly identified) to 1 (all grid points with two peaks correctly identified).

Next, we area-average the region of the SWUS within the box shown in Figure 35 for the CMIP5 models from 1979 to 2015. The seasonal cycle is standardized, and we calculate the root mean square error (RMSE) against the standardized seasonal cycle for PRISM precipitation, and Noah, Mosaic and VIC soil moisture. For our evaluation of CMIP5 NPP, we calculate the RMSE against the average seasonal cycle composited between the 15 Ameriflux monitoring sites in the bimodal region of the SWUS. The Ameriflux data are averaged to monthly resolution for a better comparison with CMIP5.

Each of the 18 models is then assigned a rank based on the percentage of the two peak region which is accurately simulated, and the RMSE, for each of the metrics (precipitation, NPP and Noah, Mosaic and VIC soil moisture) providing quantitative metrics that measure the skill of the models in representing the spatial character and seasonal cycle of the ecohydrology of the two peak region. Results are discussed in Section 3 below.

4.3 Results

4.3.1 CMIP5 model selection

4.3.1.1 Precipitation The results of the model selection process are shown in Figures 36 and 37. The majority of models capture at least 50% of the dual peak region in precipitation (Figure 36, top panel). The models which perform the worst are the GISS models (GISS-E2-H, GISS-E2-R), and those which best simulate the spatial extent of the two peak region ($>$%80) are BCCCSM1-1, CANESM2, GFDL-ESM2G, CESM2-BGC, IPSL-CM5A-MR,IPSL-CM5A-LR and NorESM1-ME. In terms of RMSE, the GISS models again have the largest standardized RMSE, while GFDL-ESM2G, CanESM2 AND IPSL-CM5A-MR have the least.

4.3.1.2 NPP The results using NPP against NLDAS-2 Noah LAI are more variable (Figure 36, bottom panel); only half of the 18 CMIP5 models analyzed capture more than 50% of the two peak area spatially. Of these models, the ones which best capture two-peak greening are NorESM1-M and NorESM1-ME (capturing 90% of the area). The worst performers are MIROC-ESM-CHEM and the GISS models, which is consistent with their poor simulation of the area of two-peak precipitation. CanESM2, GFDL-ESM2M and GFDL-ESM2G have the lowest standardized RMSE, and also do well in their simulation of the two peak vegetation greening spatially (greater than 70% of the area).

4.3.1.3 Soil moisture Upper column soil moisture also has variable performance in the CMIP5 models when evaluated against 0 - 100 cm soil moisture from NLDAS-2 Noah, Mosaic and VIC (Figure 37). For each of the NLDAS-2 comparisons, the same 6 CMIP5 models simulate at least 50% of the two peak region: the IPSL models (IPSL-CM5A-LR, IPSL-CM5A-MR), the GFDL

models (GFDL-ESM2G, GFDL-ESMS2M), CanESM2 and BCCCSM1-1. These same models also performed well in their simulation of dual season precipitation (Figure 36, top panel), and NPP (Figure 36, bottom panel). Of these, the CanESM2 model has the lowest standardized RMSE.

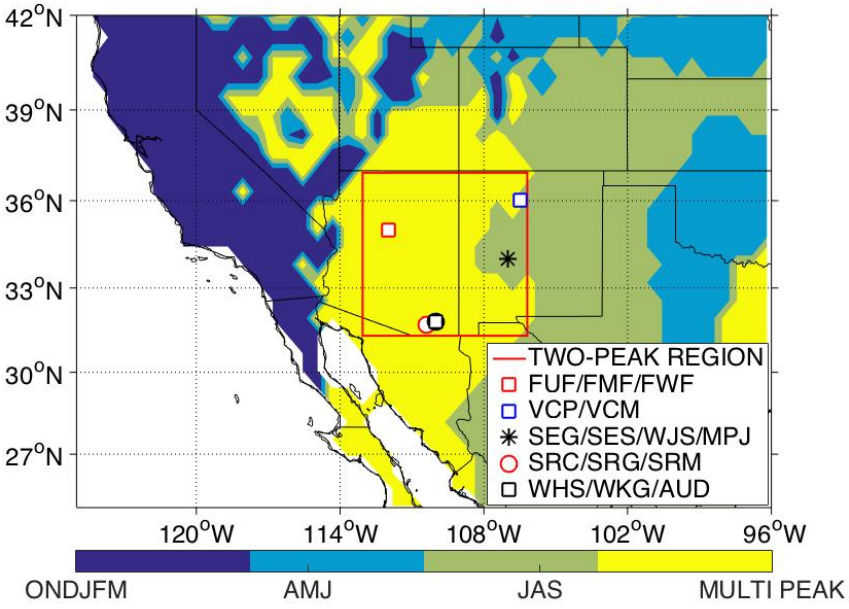

Figure 35: Map of study area. Shading indicates season of maximum precipitation (ONDJFM, AMJ, JAS or bimodal). Red box indicates region used in the study as the bimodal precipitation region. We indicate location of the Ameriflux sites (Fwf, Fuf, Fmf, Vcp, Vcm, Seg, Ses, Mpj, Wjs).(source: (Pascolini-Campbell et al. submitted))

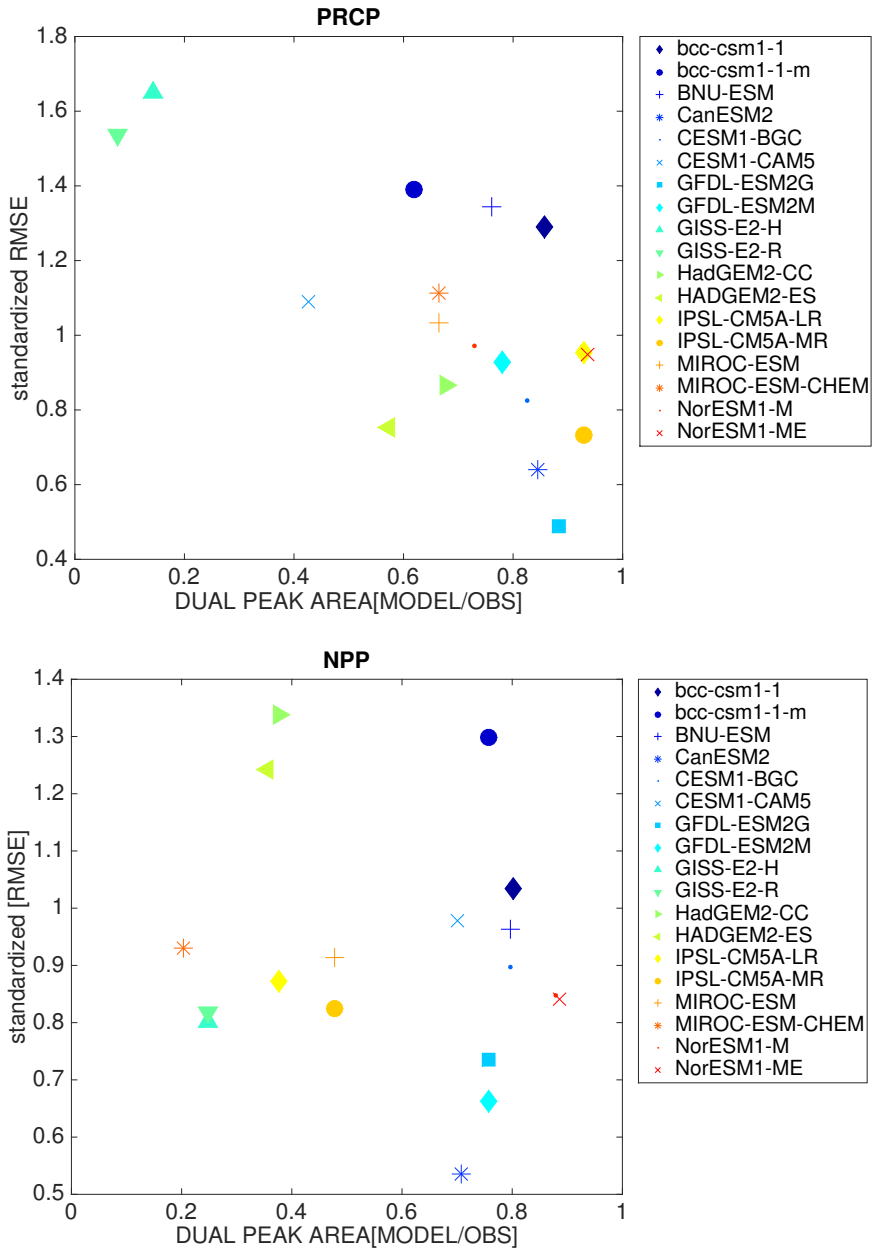

Figure 36: Scatterplot showing the results of model evaluation against PRISM precipitation (top panel) and NLDAS-2 Noah LAI and Ameriflux NEP (bottom panel). Y-axis: RMSE between CMIP5 and observations for the standardized average seasonal cycle (1979 - 2015) within the bimodal region (location indicated by box in Figure 35). X-axis: Where CMIP5 identifies a grid point as having two-peaks, we calculate whether it is correct compared to the two-peak map generated by observations, and divide by the total number of two-peak grid points from observations (values range from 0 - 1). The best models (low RMSE, high area of two-peak region correctly identified) are located on the bottom right of the scatterplots.

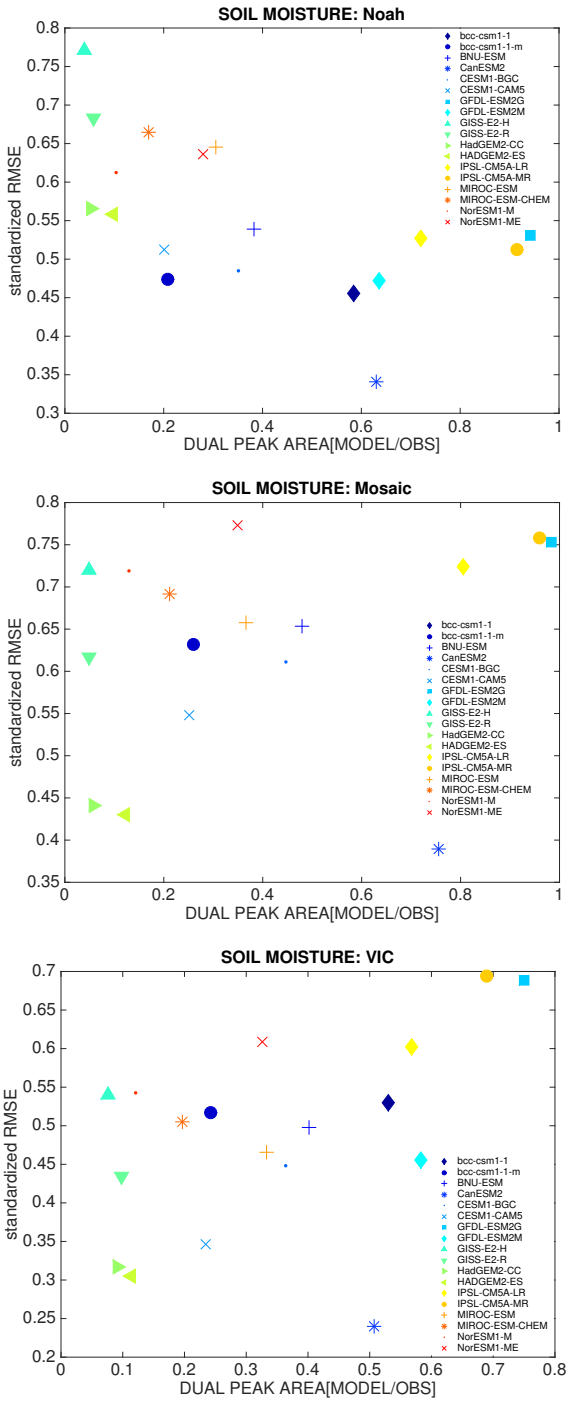

Figure 37: Same as Figure 36 for 0-100 cm soil moisture from Noah (top panel), Mosaic (middle panel) and Level 1 soil moisture from VIC (bottom panel).

Table 8: Ranks from model evaluation

Rank	Model	NPP Area	NPP RMSE	Precip Area	Precip RMSE	Noah S_m Area	Noah S_m RMSE	Mosaic S_m Area	Mosaic S_m RMSE	VIC S_m Area	VIC S_m RMSE	Total
1	CanESM2	9	1	6	2	5	1	4	1	6	1	36
2	GFDL-ESM2M	6	2	8	7	4	3	6	5	3	7	51
3	GFDL-ESM2G	2	3	4	1	1	9	1	16	1	17	55
4	CESM1-BGC	4	10	7	5	8	5	8	6	8	6	67
5	IPSL-CM5A-MR	13	6	3	3	2	6	2	17	2	18	72
6	BCC_CSM1.1	7	15	5	14	6	2	5	8	5	12	79
7	IPSL-CM5A-LR	12	9	2	9	3	8	3	15	4	15	80
8	BNU-ESM	8	13	9	15	7	10	7	10	7	9	95
9	NorESM1-ME	3	7	1	8	10	14	10	18	10	16	97
10	CESM1-CAM5	5	14	16	12	12	7	12	4	12	4	98
11	MIROC-ESM	14	11	12	11	9	15	9	11	9	8	109
12	HADGEM2-ES	15	16	15	4	15	11	15	2	15	2	110
13	NorESM1-M	1	8	10	10	14	13	14	13	14	14	111
14	BCC_CSM1.1(m)	10	17	14	16	11	4	11	9	11	11	114
15	HadGEM2-CC	11	18	11	6	17	12	16	3	17	3	114
16	MIROC-ESM-CHEM	16	12	13	13	13	16	13	12	13	10	131
17	GISS-E2-R	18	5	18	17	16	17	18	7	16	5	137
18	GISS-E2-H	17	4	17	18	18	18	17	14	18	13	154

4.3.1.4 Overall ranking

Next, for each of the metrics used (precipitation, NPP and the three soil moisture comparisons), we rank the models from 1 (best) to 18 (worst) for their performance in how well they simulate the dual area spatially, and their RMSE (Table 8). We sum the performance of the 18 models in each of these 10 rankings. The top three models (lowest score) are CanESM2, GFDL-ESM2M and GFDL-ESM2G. Following this evaluation, we focus the rest of the analysis for 21st century projections on CanESM2, GFDL-ESM2M and GFDL-ESM2G. Why the other models do not properly simulate the dual peak region is discussed in section 3.3.

4.3.2 Comparison of CanESM2, GFDL-ESM2M and GFDL-ESM2G with observations and LSMs

The average seasonal cycle for the period 1979 to 2015 for the three selected CMIP5 models and the observations used for evaluation are shown in Figure 38. For each quantity, the CMIP5 models simulate bimodality in at least precipitation and NEE.

The timing of precipitation seasonality in CanESM2 agrees well with observed values, however the summer peak in NAM is not sufficiently large (20 mm/month compared with 60 mm/month from PRISM) (Figure 38, top panel, left column). The GFDL models both simulate the precipitation bimodality, however the magnitude is too great for GFDL-ESM2G NAM precipitation, and too great in GFDL-ESM2M for winter precipitation (Figure 38, top panel, right columns). The NAM onset and peak is also later in the GFDL models compared with observed precipitation.

We compare standardized CMIP5 NPP and standardized composited NEE across the 15 Ameriflux monitoring sites, and find that there is in general good agreement between CMIP5 output and observations in the timing and magnitude of vegetation green-up (Figure 38, middle panels). The first peak for each of the three models occurs in April-May, declining during May-June in a period

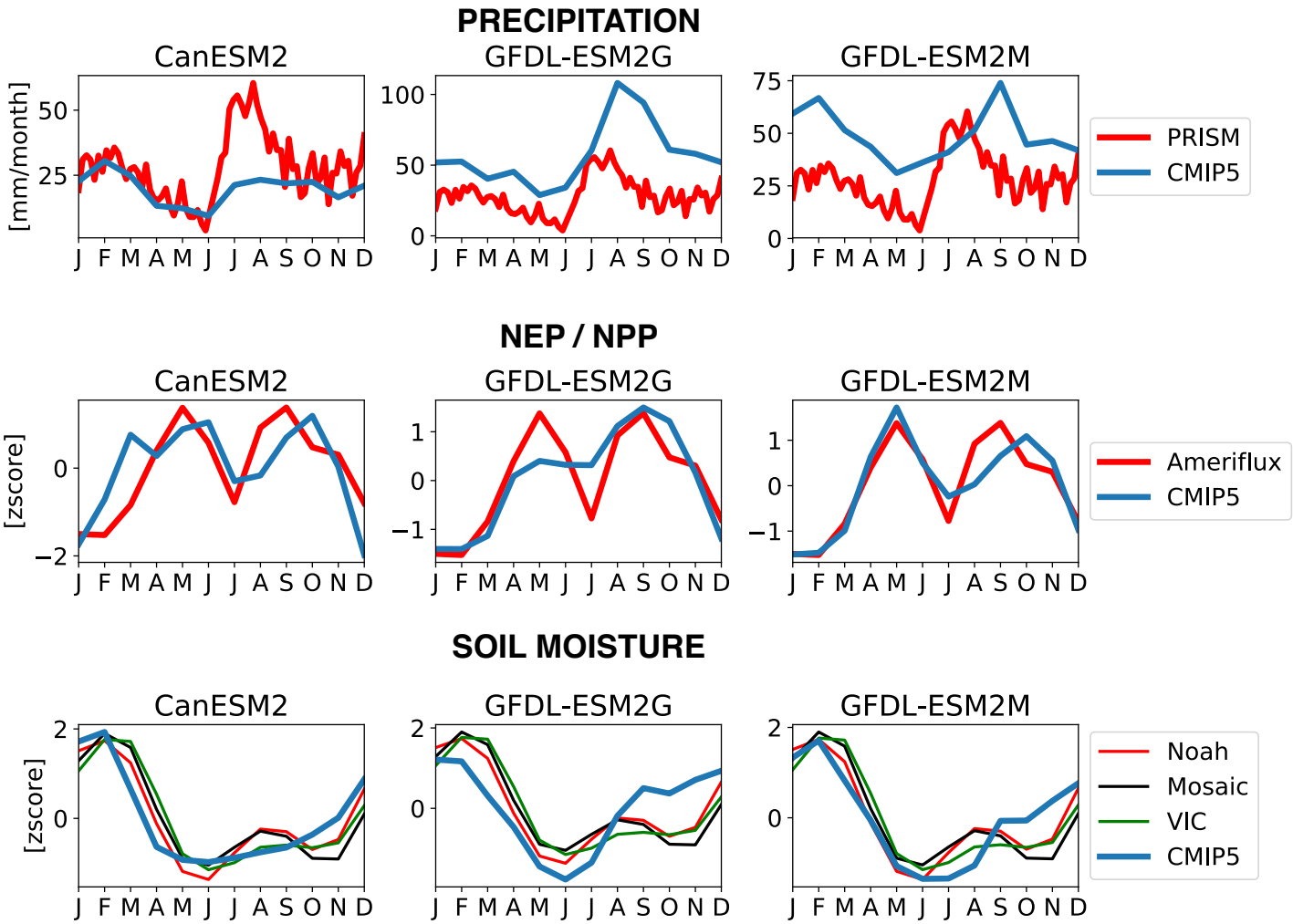

Figure 38: Seasonal cycle 1979 - 2005 (historical CMIP5) for best models CanESM2 (left column), GFDL-ESM2G (middle column), GFDL-ESM2M (right column). Compared with PRISM precipitation, NEE from Ameriflux, and 0-10cm soil moisture from NDLAS-2 Noah, Mosaic, VIC.

of vegetation senescence before recovering to a secondary summer peak in September-October. The timing of the summer peak is one month late in CanESM2 and GFDL-ESM2M. The period of spring drying and vegetation senescence is however well simulated by all three models.

While the three models correctly have greater upper column soil moisture in winter than summer, they fail to simulate the smaller summer monsoon related peak (Figure 38, bottom panels). In nature, the smaller summer peak of soil moisture, and greater winter peak of precipitation are consistent with higher ET during the summer months and greater rates of infiltration during the winter associated with snowmelt (Loik et al. 2004), as well as enhanced drying from a reduction in precipitation minus ET (P - ET) Ting et al. (2018). The models generally simulate the timing of the winter peak. Reasons for model failure in summer are discussed below in Section 3.3.2. We note that even these three "successful" models have individual biases that mean their realism in terms of projection must be assessed with skepticism.

4.3.3 Future projections in CanESM2, GFDL-ESM2G, GFDL-ESM2M

We analyze future climate projections area averaged over the bimodal region of the SWUS for the following four periods: 2021 to 2040, 2041 to 2060, 2061 to 2080 and 2081 to 2099.

4.3.3.1 Temperature Temperature increases for every month of the year in each of the three different CMIP5 models (Figure 39, top panels). Averaged annually, the temperature increase for 2081 to 2099 is 6.1^{o}C, 4.7^{o}C and 4.2^{o}C above the 1980 to 2000 average for CanESM2, GFDL-ESM2M and GFDL-ESM2G respectively. Using a Student's t-test to test the distribution of months in either of these periods (1980 - 2000 and 2050 to 2099) we find that the temperature increase is significant for each of the three models at each month during the year (at α = 0.05). This

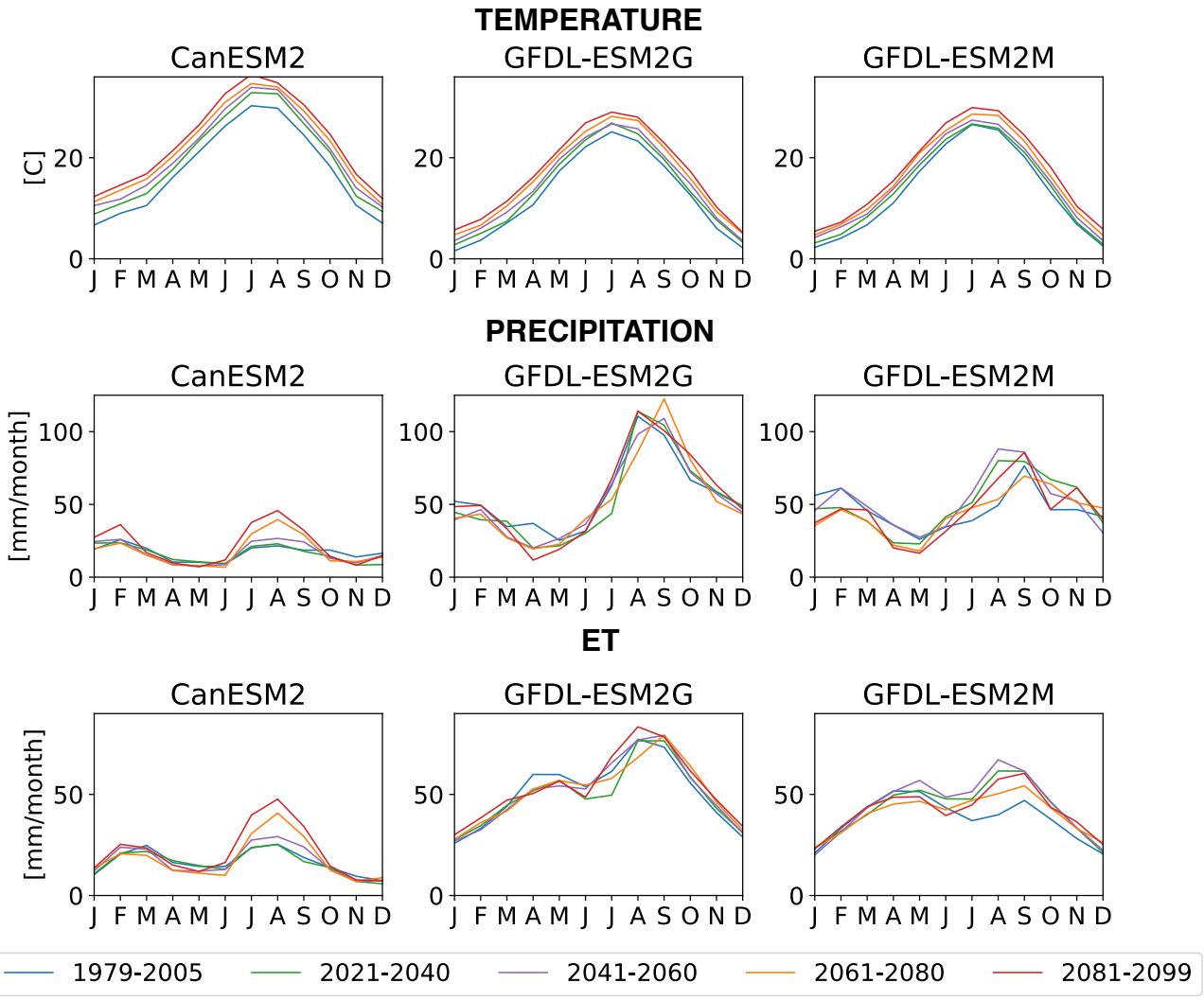

Figure 39: Seasonal cycle area-averaged in the bimodal region of decadal averages for 1979 - 2005 (historical runs), 2021 - 2040, 2041 - 2060, 2061 - 2080 and 2081 - 2099 (RCP8.5) for temperature (top panels), precipitation (middle panels) and ET (bottom panels).

substantial increase in temperatures in all months for the SWUS region is consistent across all 18 CMIP5 models (appendix A2).

4.3.3.2 Precipitation Next we analyze projected changes to precipitation in these four future periods and find the results are more variable across the three chosen models (Figure 39, middle panels). CanESM2 projects large increases in both summer precipitation in 2061 to 2099 and in winter precipitation in 2081 to 2099 (Figure 39, middle panels, left column).

The GFDL models do not show this large increase in NAM precipitation, nor a consistent change in winter precipitation (Figure 39, middle panels, right columns). In terms of seasonality, the only change that is consistent is an earlier monsoon onset in GFDL-ESM2G.

In all three CMIP5 models, spring precipitation in the second half of the current century declines between April to June. However, more generally there is considerable lack of consistency in changes during winter and summer indicating that projections for precipitation are highly variable in this region. Using the ensemble of all 18 CMIP5 models, we find that overall, annual average precipitation is projected to decrease in the region by end of the century driven primarily by declines in March-April-May precipitation (Appendix A3). This drying is also observed across the multi-model ensemble for P - E (not shown), and this agrees with other studies (Gao et al. 2014; Ting et al. 2018).

The spring drying, including in P - E, is apparently robust across the 18 models and will tend to reduce soil moisture and streamflow. However, previous analysis indicates that it is declines in the winter which most influence spring soil moisture drying in this region (Pascolini-Campbell et al. submitted), and therefore declines in the winter precipitation are of particular significance.

To assess whether the precipitation projections discussed above fall outside natural climate

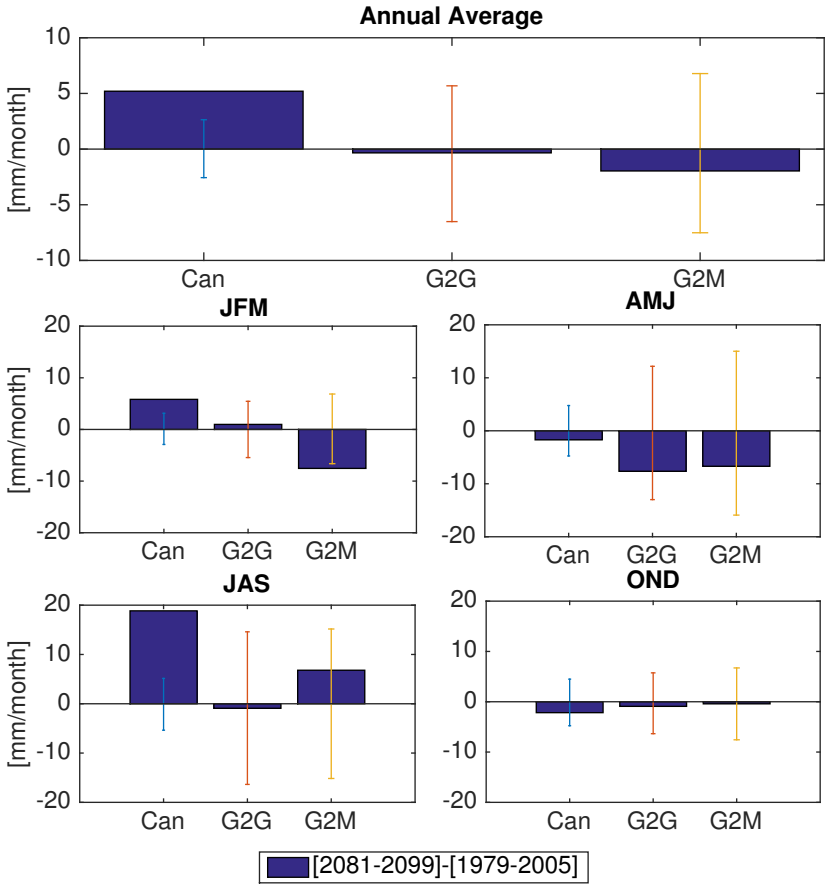

Figure 40: Difference between future (2081-2099) minus historical (1979-2005) precipitation for CanESM2 (Can), GFDL-ESM2G (G2G) and GFDL-ESM2M (G2M) (blue bars) for average annual (top panel), JFM (middle row, left), AMJ (middle row, right), JAS (bottom row, left) and OND (bottom row, right). Averages are computed over the bimodal region. The range of variability is computed by bootstrap methods using the pre-industrial control runs and plotted as error bars. The difference in future minus historical precipitation change is thought to exceed natural variability if the value (blue bars) exceeds natural climate variability (error bars).

variability, we use a bootstrapping method to sample variability in the pre-industrial control runs for each of the three models (Figure 40). We first calculate the mean difference in precipitation for a future period (2081-2099) and the historical period (1979-2005) for annual, January-February-March (JFM), April-May-June (AMJ), July-August-September (JAS) and October-November-December (OND) seasons (plotted as blue bars on Figure 40).

To sample variability, we randomly select 19-year periods and 26-year periods (non-overlapping) from the pre-industrial control runs to correspond to the length of the future (2081-2099) and historical (1979-2005) periods. For the CanESM2 model we sample 5 random periods, and for the GFDL 1 to correspond to their number of model runs. From these we compute the average of these periods, and find the difference (future minus historical). This is then performed 5000 times, and from the 5000 differences calculated we find the upper 97.5th percentile and lower 2.5th percentile to create the bounds of natural climate variability (plotted as error bars on Figure 40). If the anomaly calculated from the future minus historical period exceeds the error bars, this indicates that the anomaly is significant and there is less than a 2.5% chance of an anomaly occurring as small (or large) in the sample of the pre-industrial control runs.

The results indicate that overall, CanESM2 has annual average precipitation increase in the future which exceeds natural variability, while the GFDL models project annual average declines that fall within the range of natural climate variability. The projected increase in annual precipitation for CanESM2 is driven by increased JFM and JAS precipitation; both of which are projected to exceed natural model variability. Declines in spring precipitation in the CanESM2 and GFDL models do not exceed model natural variability. The decline in winter precipitation is the GFDL model (GFDL-ESM2M) slightly exceeds model natural variability.

It is of interest that spring precipitation declines are found to not to exceed model natural

variability, despite the overall decline projected in the multi-model mean of the 18 CMIP5 models. Gao et al. (2014) found that spring drying was robust in the SWUS, and particularly in the southern portion of our study region, with the upper portions of New Mexico and Arizona nevertheless indicating spring drying (but not at a significant level). To assess this, we analyze a more southern portion of the SWUS for the 18 models from 25^{o}N to 30^{o}N, we find that spring drying trend is indeed more pronounced, in agreement with other studies (Gao et al. 2014; Ting et al. 2018). Therefore, it is possible that the modest spring decline in Figure 40 results from including areas further to the north in our bimodal region.

4.3.3.3 ET, runoff, soil moisture and snowmelt For CanESM2 ET changes track the projected precipitation changes (Figure 39, bottom panels),increasing by the end of the 21st century, particularly the increase during the summer accompanying the projected increases in NAM precipitation for 2061 to 2099. There are no consistent changes over time, or between the GFDL models.

Projections of runoff are more consistent across the three models, and are found to decrease in the four future periods (Figure 41, top panels). The GFDL models, which best capture the bimodal runoff, indicate declines in the magnitude of both the winter and summer runoff pulses. The winter/spring peak and spring minimum flows also move to earlier in the year in the later time periods. The GFDL models do not indicate major changes in the timing of the summer runoff peak but do show that it also declines in magnitude. The CanESM2 model does not capture the summer runoff peak. This could be due ET during summer being sufficiently high in this model leading to account for all the NAM precipitation leaving none for runoff (Figure 39, bottom panels, left column). When we examine P - ET (not shown), we note there are negative values during the summer months.

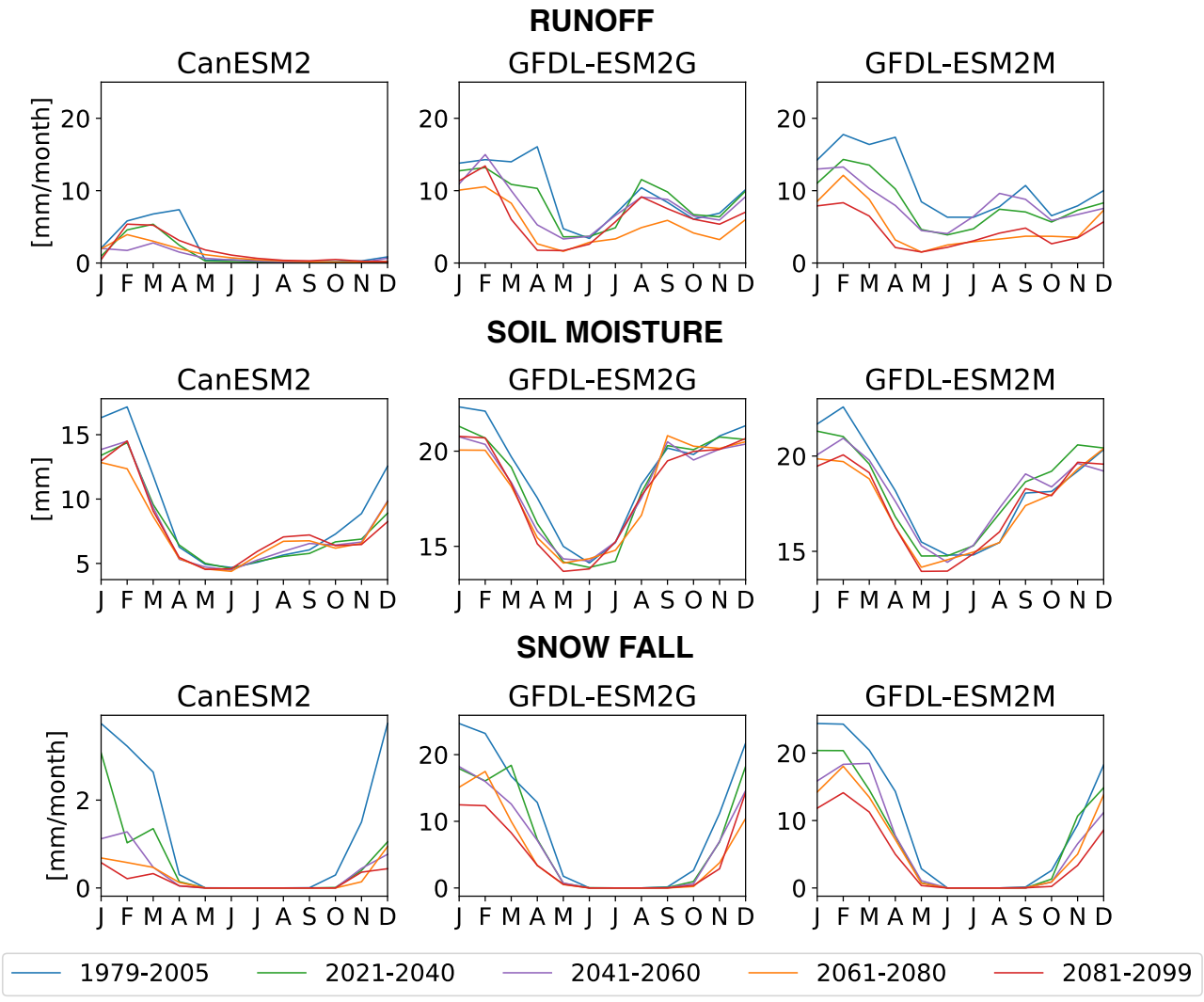

Figure 41: Seasonal cycle area-averaged in the bimodal region of decadal averages for 1979 - 2005 (historical runs), 2021 - 2040, 2041 - 2060, 2061 - 2080 and 2081 - 2099 (RCP8.5) for total runoff (top panels), upper column soil moisture (middle panels) and snow fall (bottom panels).

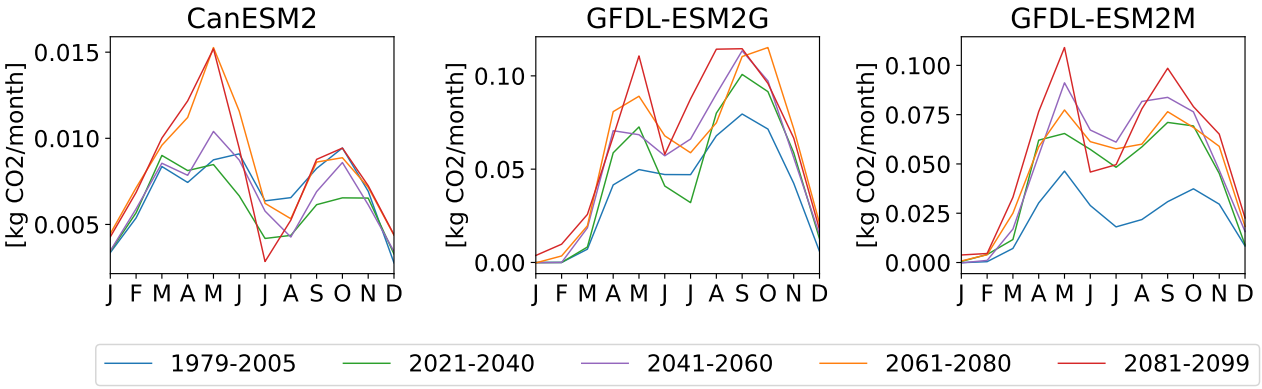

Figure 42: Seasonal cycle area-averaged in the bimodal region of decadal averages for 1979 - 2005 (historical runs), 2021 - 2040, 2041 - 2060, 2061 - 2080 and 2081 - 2099 (RCP8.5) for NPP.

Upper column soil moisture also declines in the coming decades for the GFDL models, for most months of the year (Figure 41, middle panels). The CanESM2 model does not indicate consistent changes overtime in winter soil moisture but projects increased summer soil moisture. This is in keeping with the CanESM2 models projections for enhanced NAM precipitation in future. All three models do however indicate reductions in spring soil moisture, consistent with the spring precipitation decline.

Consistent with the warming temperatures, snowfall decreases in the models in the SWUS in upcoming decades (Figure 41, bottom panels). The declines in snowmelt also will enhance drying of soil moisture in the spring, as soil moisture replenishment by spring snowmelt and gradual water infiltration to soils is diminished (Loik et al. 2004).

4.3.3.4 Vegetation NPP is projected to increase in both growing seasons for each of the three selected models (Figure 42). NPP increases are greater during the winter-spring growing season in the CanESM2. The projected annual NPP increase in 2081 to 2099 is significant above historical NPP (1980-2000) for each of the two GFDL models (using a Student's t-test for the distribution of months in each of the decadal periods we obtain t = 2.25, p = 0.07 for GFDL-ESM2G and $\alpha = 0.05$

and t = 3.2, p = 0.008, α =0.05 for GFDL-ESM2M). The increase is not found to be significant for CanESM2 (t = 1.45, p = 0.32, α = 0.05).

4.3.4 Representation of bimodal region in CMIP5: simulation of the NAM

Many of the models do not adequately capture the summer NAM peak, and hence fail to simulate accurate precipitation, vegetation and soil moisture bimodality in this region. One possible reason is the models do not extend the NAM far enough north. To investigate this, we create seasonal cycles of precipitation averaged from 1979 to 2015 from the CMIP5 models for two regions in the SWUS: a northern monsoon region, and a southern monsoon region (box outline of regions used shown in Figure 43, top panel). We compare the CMIP5 seasonal cycles using precipitation observations from PRISM for the same time period, and correlate the seasonal cycle with that from the CMIP5 models for both regions (Figure 43, bottom panel).

Results indicate that a number of the CMIP5 models have high r-values for their simulation of the monsoon in both northern and southern regions ($r > 0.5$), indicating that the simulated monsoon extends sufficiently north. These high performing models include our three selected models (CanESM2, GFDL-ESM2M and GFDL-ESM2G). In general, models that do well in the northern region also do well in the south.

Models with a low r-value for the northern region include the GISS models ($r < -0.5$) and the BCC_CSM1.1(m) model ($r < 0$). These models also performed poorly in the southern region where their seasonal cycle of precipitation is negatively correlated with observations. Hence they simulate the NAM poorly across its domain, not just in the north. These models also ranked overall poorly in our evaluation using precipitation, NPP and soil moisture (ranking 18th, 17th and 14th for GISS-E2-H, GISS-E2-R and BCC_CSM1.1(m) respectively).

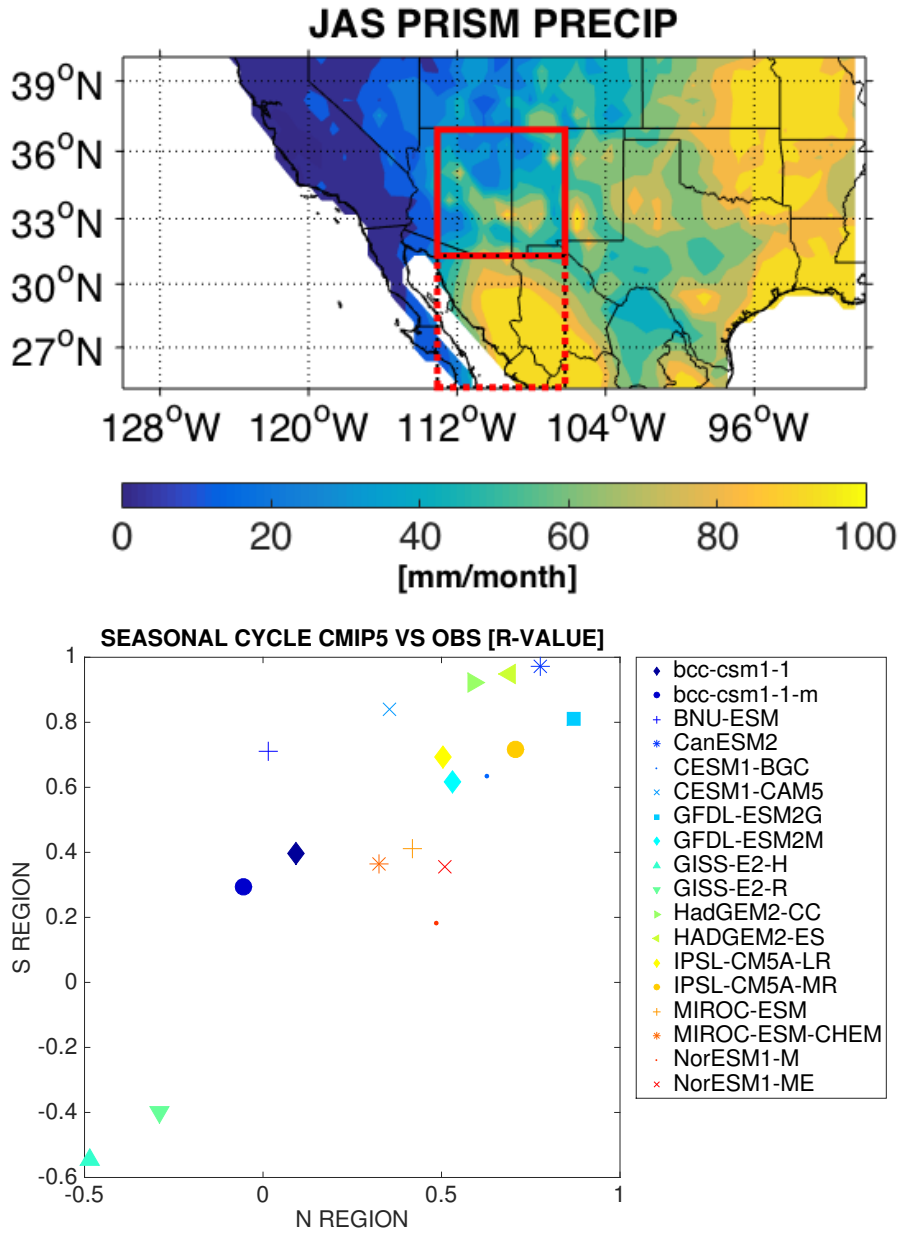

Figure 43: Top: Regions used to average i) northern monsoon, ii) southern monsoon, and average JAS precipitation (PRISM 1979 - 2005). Bottom: Correlation of seasonal cycle of CMIP5 historical runs (1979-205) with PRISM precipitation for the southern NAM region (y-axis) and northern region (x-axis).

We further explore this by creating a scatter plot of the magnitude of JAS precipitation in the northern and southern regions for each of the models (Appendix A4), and find similar results: models with large northern monsoon values also have large magnitude southern monsoon values. This suggests that the models which fail to simulate the monsoon in the north (for example the GISS models), generally fail in both regions.

4.4 Discussion & Conclusions

The three models we select that best represent this bimodal region of the SWUS (CanESM2, GFDL-ESM2M, GFDL-ESM2G) all predict significant temperature increases in the 21st century. Temperatures are projected to increase throughout the year, with annual average increases between 4.2^oC to 6.1^oC for the three models. This temperature increase is also consistent in the multi model mean for all 18 CMIP5 models.

Precipitation changes are more variable: the CanESM2 model projects larger magnitude and earlier summer NAM onset by 2081 to 2099, and these changes exceed natural climate variability. The GFDL models do not show increases in the magnitude of NAM. Changes in winter precipitation in the CanESM2 and GFDL models are also small. However, all three models do indicate a decline in spring precipitation by the end of the 21st century, however these declines only exceed natural variability for the CanESM2 model. Examining the multi model mean across the 18 CMIP5 models, we find an overall decline in annual average precipitation, largely driven by declines in spring (March-April-May).

We find that among the 18 CMIP5 models analyzed, those which perform the worst in our evaluation of the bimodal region (including the GISS models, BCC_CSM1.1(m), BNU-ESM, MIROC-

ESM, MIROC-ESM-CHEM), also tend to not adequately simulate the summer NAM in the northern portion of the study area. Furthermore, these models do not adequately simulate the summer NAM in the southern region either, indicating an overall poor representation of the monsoon. The poor simulation of NAM among these models is consistent with other work evaluating NAM simulation in CMIP5 (Geil et al. 2013).

Our results indicate that despite the varied projections of precipitation, the bimodal region of the SWUS is projected to become drier during the spring by the end of the 21st century. The declines in spring soil moisture are likely due to reduced winter snowfall and hence less infiltration of snowmelt into the soils, which is critical for building spring moisture supply (Loik et al. 2004). Runoff also is reduced in magnitude and subsides earlier in the year, reducing spring moisture availability.

Despite drying during the winter and spring, the models unanimously project NPP to increase in future decades due to CO_2 fertilization. This is consistent with other model based studies which have found that the western United States will become, paradoxically, both drier and greener (Mankin et al. 2017). The increased greening is particularly prominent during the first spring peak, although the three models also project increases during the summer peak. The greening of the SWUS will increase water drawdown and evaporative losses, further exacerbating drying during the spring and summer. The water losses from enhanced plant growth will also lead to reduced surface runoff, which could reduce the spring streamflow pulse, and have ramifications on water management in the west in the 21st century.

The role of CO_2 enhanced greening leading to drying has been detected in observations from the satellite period (Ukkola et al. 2015). However, other studies comparing observations with models have found that models overpredict vegetation growth due to CO_2 fertilization (Smith

et al. 2015), and therefore model projections of greening -but-drying must be treated with extra skepticism. Further studies comparing the impacts of observed CO_2 fertilization with fertilization simulated by models are needed to constrain projections of future vegetation change in this region.

The impacts on summer hydroclimate is more variable, with the GFDL models indicating drying out of the secondary peak in soil moisture in later decades and the CanESM2 model instead projecting wetting. Resolving these disagreements will rely on improving projections of precipitation in the SWUS, and future analysis of CMIP6 output could help to provide new insights on the fate of hydroclimate for the bimodal region.

Despite caveats, a number of results for this region of the bimodal region of the SWUS stand out from our analysis of model output:

- The SWUS will become warmer by the end of the 21st century for every month of the year.
- Less precipitation will be in the form of snow.
- Runoff during the spring season will be earlier and reduced.
- The spring will be drier: the multi-model ensemble results indicate a decline in spring precipitation, P - E, and this agrees with other studies (Gao et al. 2014; Ting et al. 2018).

There are also a number of unresolved points from this model analysis, including future projections of winter and summer precipitation. The three selected models disagree in how winter and summer precipitation will respond to warming temperatures, and many of the changes are apparently due to natural climate variability. The change in the timing and magnitude of the NAM also remains uncertain, and requires further investigation. Finally, despite robust increases in NPP in this region, which is consistent with other studies (Mankin et al. 2017), the behavior of vegetation

in the future is still uncertain and this is due to the divergence between observed and modeled CO_2 fertilization.

Conclusion

Main findings

The variability of hydroclimate in the SWUS determines water availability, streamflow, and vegetation green up, and these also influence wildfire outbreak, and riparian ecosystems. The social and economic vitality of the SWUS depends on the interaction of climate and ecosystems, and understanding their driving mechanisms is of importance in light of the ongoing drought, fresh water shortages, and wildfire outbreaks which afflict the region. Temperatures have also been increasing in the SWUS throughout the twentieth and twenty-first centuries, and this trend is expected to continue (Hoerling and Kunkel 2013). For the 9.6 million people who reside in this region, it is critical to understand the ecohydrology, and use this understanding to inform analysis of future projections. This thesis has used observations and model output to address these issues, and our findings, as well future research directions are discussed below.

Streamflow

Streamflow in the SWUS is predominantly influenced by natural climate variability. The spring streamflow peak of rivers lying further west, such as the Gila, is driven by winter precipitation and snowmelt modulated by Pacific SST (Chapter 1). The spring peak in streamflow occurs in February-March-April-May. On interannual timescales, spring streamflow responds to ENSO, while on longer timescales, the Pacific Decadal Oscillation (PDO) generates extended periods of low and high streamflow. A warm (cold) ENSO or PDO will produce anomalously high (low) spring streamflow which arrises from the teleconnection of SST with precipitation. Spring streamflow experiences a lag with winter precipitation by one-two months and peaks following snowmelt,

while summer streamflow (e.g. for the Gila) is concurrent with the North American Monsoon (NAM). The magnitude of the summer streamflow peak depends on variability of the NAM which is itself controlled by localized convective activity, and is not influenced by Pacific SST.

The upper Rio Grande, whose headwaters lie further to the east in the San Juan Mountains of southern Colorado, has one peak in streamflow occurring later in the year (in spring-summer (AMJJ)) than that of the Gila, which is consistent with its more northern location and the delayed effects of snowmelt. It is affected by both Pacific and Atlantic SST, and the warm phases of ENSO and PDO, and the cold phase of the Atlantic Multidecadal Oscillation (AMO), produce above normal precipitation anomalies in the headwaters of the upper Rio Grande (Chapter 2). The relationship on interannual timescales with ocean SST is imperfect; indeed, some of the largest streamflow anomalies have occurred during cold tropical Pacific SST events, such as 1942, 1984 and 1985. This emphasizes that internal atmosphere variability exerts a strong control on Rio Grande flow, sufficient to at times override the ocean influence. The relationship is more coherent on longer timescales, with phases of the PDO with cold tropics agreeing with long term periods of hydrological drought in the upper Rio Grande.

These findings suggest that though SWUS streamflow is influenced by natural modes of climate variability, higher predictability occurs on longer timescales while shorter time scales are more influenced by random weather fluctuations that will not be predictable on the seasonal or interannual timescale. These findings also indicate the importance of location in controlling SST predictability of streamflow; more western rivers are primarily influenced by the Pacific, and rivers further east in the SWUS are influenced by both the Pacific and Atlantic oceans. For the upper Rio Grande basin, the more southern gages have a more coherent teleconnection with Pacific and Atlantic SST, consistent with being closer to the center of teleconnections driven by the Pacific and

Atlantic SSTs.

Both annual and spring-summer streamflows have declined for the Gila and upper Rio Grande rivers since 1998, and this region has also undergone warming during this period (Hoerling and Kunkel 2013). When we removed the portion of annual and spring-summer flow predicted by tropical Pacific, and in the case of the upper Rio Grande, also tropical north Atlantic SSTs, we did not find any additional streamflow declines not explained by SST. This suggests that the recent declines are attributed to natural decadal variability influenced by SSTs. For the Gila River, summer streamflow (August-September) constitutes a substantial portion of annual flow contributing on average $\sim$15% during 1928 to 2012, and summer flow has not declined in the latest dry period, indicating that the annual declines are driven by changes in the spring peak.

Based on the findings in this dissertation, we have found that SST in the tropical Pacific only provides limited explanatory power in predicting Upper Rio Grande streamflow on interannual timescales, with some of the largest streamflow events resulting from random weather. Therefore year-to-year management of this basin can not be based on SST alone, and water management should be conservative in water allocation even following warm tropical Pacific events.

Ecohydrology of the SWUS dual-peak precipitation region

Precipitation in the winter is the dominant control on spring soil moisture and ecosystem productivity in the SWUS. Precipitation and subsequent snowmelt, builds up soil moisture and the soil moisture is then used up in spring vegetation green-up and lost via ET, in agreement with previous studies (Notaro et al. 2010; Vivoni et al. 2008). Winter-spring precipitation also controls the severity and timing of the spring dry season in the SWUS. The shift from a wet period (1979 - 1997) to the recent period of drying (1999 - 2017) was dominated by a drop in winter-spring pre-

cipitation and reduced snowmelt leading to drier conditions. The spring dry season also shifted to earlier in the year due to less total winter precipitation and snowmelt, and hence a faster drying out of available moisture. These changes were associated with the observed shift in the Pacific from warm to cold tropical SST conditions (Zhang et al. 1997; Mantua et al. 1997) (explored in Chapter 3) and which we identified led to low streamflows in the Gila and upper Rio Grande basins.

This decadal shift in hydroclimate observed in the regional ecosystem was observed in an analysis of GIMMS NDVI. A decline in average spring NDVI occurred during the recent dry period (post-1999) relative to the earlier wetter decades (1981-1997). Summer vegetation activity was not affected by the winter-spring shift to drier conditions, indicating that the NAM (which was largely unchanged between the two periods) is the dominant control on summer green-ups, and has a concurrent impact on vegetation productivity which agrees with previous studies (Notaro et al. 2010).

To place the recent changes in a longer term context, we also investigated a period of extended drying in the region in the mid-century (from 1948 to 1966) that occurred in response to anomalously low winter-precipitation. The decline in annual average precipitation is similar for both the mid-century dry periods (1948-1966) and the recent dry period (1999-2017). However, the spring drying during the recent period is more severe. Annual average temperatures are also greater during the recent drying compared to the mid-century. Using a decomposition for the impact of precipitation and potential evapotranspiration (PET) on soil moisture (Williams et al. 2017), it was found that PET contributed 39% to drying in the recent dry period, compared to 6% in the mid-century. This increase indicates the enhanced role of PET, and therefore temperature, on exacerbating the severity of SWUS drying which agrees with a similar analysis for the Colorado River (Woodhouse et al. 2016).

Observed temperature increases in the SWUS can be attributed to human-induced climate change. The temperatures during 2000 to 2010 are on average $\sim 0.8^{o}$C warmer compared to the the average for 1900 to 2000 (Hoerling and Kunkel 2013), and studies have indicated this warming is attributed to human-induced climate change for increases in minimum and maximum daily temperature (Bonfils et al. 2008), snowpack reduction (Pierce et al. 2008), and streamflow timing (Hidalgo et al. 2009). Given the human contribution to temperature increases, snowpack reduction, and streamflow timing, it is possible the enhanced spring drying of soil moisture detected in this study is also influenced by anthropogenic warming, but future studies are required to analyze this.

CMIP5 Model projections for the SWUS

Next we investigated projected changes to the region for the 21st century by analyzing the archive of CMIP5 models' RCP8.5 scenario (Chapter 4). We evaluated the CMIP5 models based on comparisons of the historical runs with observations of precipitation, net ecosystem productivity (NEP), and land surface model output of soil moisture and leaf area index. We then ranked the performance of each model, and selected three which best simulated the bimodal region: CanESM2, GFDL-ESM2G and GFDL-ESM2M. Many of the CMIP5 models failed in simulating the bimodal region due to a poor representation of the NAM: either the NAM did not extend sufficiently far north, or the model entirely failed to simulate the monsoon in both the northern and southern core region (e.g. the GISS-E2-H and GISS-E2-R models).

From the three selected models we found, in agreement with previous studies, that the SWUS region is projected to become drier by the end of the 21st century, particularly during the spring (Gao et al. 2014; Ting et al. 2018). By the end of the 21st century, projections indicate a decline in winter and spring soil moisture, as well as reduced and earlier runoff and snowmelt. However

the three models disagree on future projections of precipitation: CanESM2 projects large increases in NAM by the end of the 21st century above 1979 to 2005 levels, and this drives an overall annual precipitation increase for the CanESM2 model. The GFDL models instead project overall precipitation declines, which are driven by declines in spring precipitation.

For the most part, the precipitation changes by the end of the 21st century above 1979 to 2005 levels are found to be insignificant: the projections lie within the range of variability predicted by sampling from the pre-industrial control runs for each model (details in Chapter 4). The only significant changes for projected precipitation for the end of the century above 1979 to 2005 levels occur fro the CanESM2 model in winter (JFM) and summer (JAS). The insignificant changes for the GFDL models and CanESM2 in other seasons, indicates that for the most part, precipitation changes by the end of the century do not exceed natural variability. Even if the precipitation projections do not exceed natural decadal variability, they can however be of importance for the SWUS (for example the shift to drier conditions, and reduced streamflow resulting from the post-1998 Pacific shift as discussed in Chapters 1 to 3). The ensemble size of each of the CMIP5 models also affects the natural variability: the CanESM2 has 5 ensemble members compared to the GFDL models which each have 1, and the greater number of members narrows the natural variability, which could explain why the signal is stronger for this model.

Turning to the multi-model ensemble for precipitation, the average CMIP5 model response to CO_2 emissions indicated a decline in total precipitation by the end of the century, driven by declines in winter and particularly spring precipitation, in agreement with other studies (Gao et al. 2014; Ting et al. 2018). The multi-model ensemble also indicates an increase in summer precipitation. CanESM2 and the GFDL models project declines in spring precipitation by the end of the century, and are therefore representative of the multi-model mean.

Large increases in net primary productivity (NPP) in both growing seasons are also projected for the end of the 21st century, due to the effects CO_2 fertilization (Mankin et al. 2017). The NPP increases are likely to cause further drying of soils and reduced streamflow by increased water uptake during vegetation growth, and via enhanced ET.

This region is heavily dependent on winter-spring precipitation, which varies greatly due to natural variability. The future of this region will therefore depend on how natural variability in the tropical Pacific, and to a lesser extent the Atlantic, evolves and how these are translated into SWUS precipitation anomalies in addition to any radiatively-forced changes in precipitation. Warming has also exacerbated spring drying in recent decades, and this trend will continue and it can be expected that water resources will become increasingly stressed in future. Water managers can therefore expect exacerbation of drought conditions in the future with rising temperatures, and as such should be conservative in water allocation.

Spring soil moisture also influences runoff due to the role of soil moisture saturation on infiltration. In general, more saturated soils will increase surface runoff, while unsaturated soils allow greater infiltration and therefore reduce runoff (Penna et al. 2011). Drying of soils in the future implies that surface runoff during spring will more readily infiltrate, and this could reduce surface runoff during the spring, and therefore lead to a further decline in streamflow. However, the infiltration capacity of soils is also influenced by a number of other factors including soil permeability, residence time of water (with longer residence events, such as snowmelt, leading to greater infiltration), and intensity of precipitation events (with high intensity events often leading to greater runoff) (Loik et al. 2004). Therefore, the intensity as well as magnitude of rainfall during the spring in the future will be of importance in predicting changes in runoff.

Future research directions

Further work is necessary to constrain our understanding of future changes. In particular, constraining projections of precipitation change, and the impacts of the competing effects of CO_2-fertilization versus drying on vegetation, are needed.

Precipitation The ensemble average of the CMIP5 models indicates an overall decline in SWUS precipitation by the end of the 21st century, however the response among the models which best simulate this particular area (CanESM2, GFDL-ESM2G, GFDL-ESM2M) is varied. The changes in projected future precipitation for the most part are not significant at a 5% level when compared to sampling from the pre-industrial controls, except for projected increases in JFM and JAS season precipitation in CanESM2. Given the critical importance of winter precipitation on snowpack, melt, soil moisture and spring vegetation greening, it is necessary to enhance the robustness of precipitation projections for the SWUS, and we suggest this can be achieved through regional climate modeling (discussed below).

This thesis has indicated a failure of many CMIP5 models to adequately simulate both the seasonality and magnitude of the NAM. The SWUS vitally depends on summer rainfall for vegetation, summer streamflow and hence a number of aquatic species that rely on streamflow for fish spawning (Perkin and Gido 2011; Dudley and Platania 2007), but the response of the NAM to CO_2-forcing disagrees among the three selected CMIP5 models. Other CMIP5 models also inadequately simulate the NAM in the bimodal SWUS region, as well as in the core NAM region entirely (e.g. the GISS models). It is necessary to properly simulate the NAM due to its importance for SWUS hydroclimate and ecosystems, in light of potential changes to NAM characteristics under CO_2-forcing (Cook and Seager 2013; Pascale et al. 2017).

Studies have indicated that using regional models driven by dynamically downscaled output from global climate models, improves the simulation of the NAM (Castro et al. 2012; Chan and Misra 2010; Bukovsky et al. 2013). The improvement is attributed to the better simulation of daily convective activity, which is characteristic of the NAM (Castro et al. 2012), however biases in the driving global models may still lead to a misrepresentation of the magnitude of precipitation. Future work using dynamically downscaled projections may improve the robustness of precipitation changes within this region in the 21st century, and will also help constrain our understanding of how other components of hydroclimate may respond.

Impact on vegetation of CO_2 fertilization The SWUS is projected to become both "greener and drier" by the end of the 21st century in CMIP5 models, in agreement with other studies for the North American west (Mankin et al. 2017). The CMIP5 projections indicate large increases in NPP in both the spring and summer green-ups, despite decreases in snowmelt, soil moisture and run off, which suggests that CO_2-fertilization offsets vegetation decline from drying. The observational analyses presented in this thesis using Ameriflux and NDVI, indicate that vegetation growth declined in response to natural shifts to drier conditions post-1998; this indicates the importance of moisture availability to changes in vegetation productivity. Studies of NDVI and leaf area index response to CO_2-fertilization during the satellite period (1981 to present) have also indicated that Earth system models overpredict the effect of fertilization on plants by almost a factor of two globally, and the divergence between models and observations is even greater in arid locations including the SWUS (Smith et al. 2015). This presents a major caveat in our interpretation of NPP projections from CMIP5 models, and further studies comparing the observed response of vegetation to CO_2-fertilization (in i.e. NDVI) with land surface models are needed.

Enhanced future vegetation growth is also likely to further exacerbate drying in terms of soil moisture draw down, reduced runoff and increased ET by plants, and this mechanism has been found in other modeling studies (Mankin et al. 2017), as well as in observations (Ukkola et al. 2015). It is of interest to quantify these shifts in how water is used for the future in both the spring and summer green-ups. It will also be of interest to directly relate how changes in vegetation cover influence streamflow, soil moisture, and ET. Modeling studies have indicated that the CO_2-fertilization enhancement of vegetation growth in the will lead to more water from precipitation going to ecosystems rather than runoff in the future (Mankin et al. 2018b). However, as stated above, the magnitude of these changes depend on the reliability of future projections of vegetation under CO_2 emissions.

Wildfire, streamflow and ecosystems Investigating the direct connection between SWUS climate dynamics and wildfire is also of value. This thesis has indicated that natural climate variability plus human-induced warming produced a shift towards drier conditions post-1998, leading to an earlier spring soil moisture minimum, which based on other studies implies an earlier and more severe fire season (Westerling et al. 2006). Observational studies have also indicated that the burn area and severity of fires has increased in the western United States during the recent dry periods compared to earlier in the 20th century (Crockett and Westerling 2017). A quantitative assessment using records of wildfire (and satellite imagery of burned area e.g. Williams et al. (2013)), could provide important insights into the relationship between spring drying and wildfire outbreak in this region. A further analysis of how annual timing and magnitude of the NAM impacts the duration of the wildfire season in this region would also provide important information.

The direct impact of the dry season on streamflow and aquatic ecosystems is also of value. This

thesis found a shift toward earlier and reduced runoff post-1998 in the bimodal SWUS region, as well as declines in streamflow of the the spring peaks of the Gila and upper Rio Grande, associated with natural decadal SST variability. Future research could use observations to relate fish population to the magnitude of the spring and streamflow pulses, and whether interannual and decadal variations forced by SST are reflected. The CMIP5 model projections for this region analyzed in this thesis indicated declines in runoff by the end of the 21st century, with the implication of increased stream fragmentation, reduced streamflow, which would therefore be detrimental for fish populations (Dudley and Platania 2007; Perkin and Gido 2011). To constrain estimates of future ecosystem vitality, it will be necessary to first investigate the role of climate on aquatic species using available population records. The predictability of ecosystem vitality is of importance in resource management for the SWUS, including efforts to protect a number of endangered species living in the SWUS (Dahm et al. 2005).

Final remarks

This thesis has used observations, climate reconstructions, land surface model output and future projections to investigate the mechanisms influencing the variability of hydroclimate and ecosystems in the SWUS. This research enhances our knowledge of the dynamics influencing precipitation, streamflow, soil moisture, and vegetation growth on interannual to decadal timescales, as well as how these processes interact. This thesis has also presented future projections for the region under CO_2-forcing. This research therefore contributes to our understanding of climate dynamics in the SWUS, and informs water resource management. However, significant challenges remain for projecting changes into the 21st century, and these are due foremost to the poor representation

of NAM and the bimodal seasonal cycle of hydroclimate and vegetation in this region, and we suggest future work with regional models may improve the robustness of projections. In addition, uncertainty in the effects of CO_2-fertilization need to also be resolved in order to assess the role of vegetation in further drying in the future. Finally, we also recognize the need for additional studies which relate climate to riparian ecosystems (fish, birds) and wildfire, in order to constrain our knowledge of how they response to climatic shifts and therefore how they may evolve.

References

Abatzoglou, J. T., and A. P. Williams, 2016: Impact of anthropogenic climate change on wildfire across western us forests. *Proceedings of the National Academy of Sciences*, **113 (42)**, 11 770–11 775, doi:10.1073/pnas.1607171113, URL http://www.pnas.org/content/113/42/11770, http://www.pnas.org/content/113/42/11770.full.pdf.

Adams, D. K., and A. C. Comrie, 1997: The North American Monsoon. *Bulletin of the American Meteorological Society*, **78 (10)**, 2197–2213, doi:10.1175/1520-0477(1997)078⟨2197:TNAM⟩2.0.CO;2, URL http://dx.doi.org/10.1175/1520-0477(1997)078⟨2197:TNAM⟩2.0.CO;2.

Ault, T. R., 2015: Trends and natural variability of spring onset in the coterminous United States as evaluated by a new gridded dataset of spring indices. *J. Clim.*, **28**, 8363–8378.

Ault, T. R., J. E. Cole, J. T. Overpeck, G. T. Pederson, and D. M. Meko, 2014: Assessing the risk of persistent drought using climate model simulations and paleoclimate data. *Journal of Climate*, **27 (20)**, 7529–7549.

Baldocchi, D., and Coauthors, 2001: Fluxnet: A new tool to study the temporal and spatial variability of ecosystem-scale carbon dioxide, water vapor, and energy flux densities. *Bulletin of the American Meteorological Society*, **82 (11)**, 2415–2434, doi:10.1175/1520-0477(2001)082⟨2415:FANTTS⟩2.3.CO;2, URL https://doi.org/10.1175/1520-0477(2001)082⟨2415:FANTTS⟩2.3.CO;2.

Barlow, M., S. Nigam, and E. Berbery, 1998: Evolution of the North American Monsoon System. *Journal of Climate*, **11 (9)**, 2238–2257, doi:10.1175/1520-0442(1998)011⟨2238:EOTNAM⟩2.0.CO;2.

Barlow, M., S. Nigam, and E. H. Berbery, 2001: ENSO, Pacific decadal variability, and U.S. summertime precipitation, drought, and stream flow. *Journal of Climate*, **14 (9)**, 2105–2128, doi:10.1175/1520-0442(2001)014⟨2105:EPDVAU⟩2.0.CO;2, URL http://dx.doi.org/10.1175/1520-0442(2001)014⟨2105:EPDVAU⟩2.0.CO;2.

Barnett, T. P., and Coauthors, 2008: Human-Induced Changes in the Hydrology of the Western United States. *Science*, **319 (5866)**, 1080–1083, doi:10.1126/science.1152538, URL http://science.sciencemag.org/content/319/5866/1080, http://science.sciencemag.org/content/319/5866/1080.full.pdf.

Bentz, B., 2008: Western U.S. bark beetles and climate change. *U.S. Department of Agriculture Forest Service, Climate Change Resource Center*.

Bonfils, C., and Coauthors, 2008: Detection and attribution of temperature changes in the mountainous Western United States. *Journal of Climate*, **21 (23)**, 6404–6424, doi:10.1175/2008JCLI2397.1, URL https://doi.org/10.1175/2008JCLI2397.1.

Bukovsky, M. S., D. J. Gochis, and L. O. Mearns, 2013: Towards assessing NARCCAP regional climate model credibility for the North American Monsoon: current climate simulations. *Journal of Climate*, **26 (22)**, 8802–8826, doi:10.1175/JCLI-D-12-00538.1, URL https://doi.org/10.1175/JCLI-D-12-00538.1.

Castro, C. L., H.-I. Chang, F. Dominguez, C. Carrillo, J.-K. Schemm, and H.-M. Henry Juang, 2012: Can a regional climate model improve the ability to forecast the North American Monsoon? *Journal of Climate*, **25 (23)**, 8212–8237, doi:10.1175/JCLI-D-11-00441.1, URL https://doi.org/10.1175/JCLI-D-11-00441.1.

Castro, C. L., T. B. McKee, and R. A. Pielke, 2001: The relationship of the north american monsoon to tropical and north pacific sea surface temperatures as revealed by observational analyses. *Journal of Climate*, **14 (24)**, 4449–4473, doi:10.1175/1520-0442(2001)014⟨4449:TROTNA⟩2.0.CO;2, URL https://doi.org/10.1175/1520-0442(2001)014⟨4449:TROTNA⟩2.0.CO;2.

Cayan, D., K. Redmond, and L. Riddle, 1999: ENSO and hydrologic extremes in the western United States (vol 12, pg 2881, 1999). *Journal of Climate*, **12 (12)**, 3516–3516.

Cayan, D. R., M. D. Dettinger, S. A. Kammerdiener, J. M. Caprio, and D. H. Peterson, 2001: Changes in the Onset of Spring in the Western United States. *Bulletin of the American Meteorological Society*, **82 (3)**, 399–415, doi:10.1175/1520-0477(2001)082⟨0399:CITOOS⟩2.3.CO;2, URL https://doi.org/10.1175/1520-0477(2001)082⟨0399:CITOOS⟩2.3.CO;2.

Chan, S. C., and V. Misra, 2010: Dynamic downscaling of the North American Monsoon with the NCEP–Scripps Regional Spectral Model from the NCEP CFS Global Model. *Journal of Climate*, **24 (3)**, 653–673, doi:10.1175/2010JCLI3593.1, URL https://doi.org/10.1175/2010JCLI3593.1.

Chen, X., and J. M. Wallace, 2015: ENSO-Like Variability: 1900–2013. *Journal of Climate*, **28 (24)**, 9623–9641, doi:10.1175/JCLI-D-15-0322.1, URL http://dx.doi.org/10.1175/JCLI-D-15-0322.1.

Christof, B., K. Dominik, and V. T. T., 2005: Multiple disturbance interactions and drought influence fire severity in Rocky Mountain subalpine forests. *Ecology*, **86 (11)**, 3018–3029, doi:10.1890/05-0011, URL https://doi.org/10.1890/05-0011.

Cook, B. I., T. R. Ault, and J. E. Smerdon, 2015: Unprecedented 21st century drought risk in

the American Southwest and Central Plains. *Science Advances*, **1 (1)**, URL http://advances.sciencemag.org/content/1/1/e1400082.abstract.

Cook, B. I., E. R. Cook, K. J. Anchukaitis, R. Seager, and R. L. Miller, 2011a: Forced and unforced variability of twentieth century North American droughts and pluvials. *Climate Dynamics*, **37 (5)**, 1097–1110, doi:10.1007/s00382-010-0897-9, URL https://doi.org/10.1007/s00382-010-0897-9.

Cook, B. I., and R. Seager, 2013: The response of the North American Monsoon to increased greenhouse gas forcing. *Journal of Geophysical Research. Atmospheres*, **118 (4)**, 1690–1699, doi:10.1002/jgrd.50111.

Cook, B. I., R. Seager, and R. L. Miller, 2011b: On the causes and dynamics of the early twentieth-century North American pluvial*. *Journal of Climate*, **24 (19)**, 5043–5060, doi:10.1175/2011JCLI4201.1, URL http://dx.doi.org/10.1175/2011JCLI4201.1.

Cook, E., U. Lall, C. Woodhouse, and D. Meko, 2004: North american pdsi reconstructions. *NOAA Paleoclimatology*.

Cook, E. R., R. Seager, M. A. Cane, and D. W. Stahle, 2007: North american drought: Reconstructions, causes, and consequences. *Earth-Science Reviews*, **81 (1-2)**, 93–134, doi:10.1016/j.earscirev.2006.12.002.

Cook, E. R., R. Seager, R. R. Heim, R. S. Vose, and C. Herweijer, 2010: Megadroughts in North America: placing IPCC projections of hydroclimatic change in a long-term palaeoclimate context. *Journal of Quaternary Science*, **25 (1)**, 48–61, doi:10.1002/jqs.1303.

Córdoba-Machado, S., R. Palomino-Lemus, S. R. Gámiz-Fortis, Y. Castro-Díez, and M. J. Esteban-Parra, 2016: Seasonal streamflow prediction in Colombia using atmospheric and oceanic patterns. *Journal of Hydrology*, **538**, 1–12.

Crockett, J. L., and A. L. Westerling, 2017: Greater temperature and precipitation extremes intensify western U.S. droughts, wildfire severity, and Sierra Nevada Tree Mortality. *Journal of Climate*, **31 (1)**, 341–354, doi:10.1175/JCLI-D-17-0254.1, URL https://doi.org/10.1175/JCLI-D-17-0254.1.

Dahm, C. N., R. J. Edwards, F. P. Gelwick, A. C. Benke, and C. E. Cushing, 2005: *Gulf Coast rivers of the Southwestern United States*, 180–228. Academic Press, Burlington, doi:https://doi.org/10.1016/B978-012088253-3/50008-0, URL http://www.sciencedirect.com/science/article/pii/B9780120882533500080.

Dai, A., 2013: The influence of the inter-decadal Pacific oscillation on US precipitation during 1923–2010. *Climate Dynamics*, **41 (3-4)**, 633–646, doi:10.1007/s00382-012-1446-5.

Daly, C., M. Halbleib, J. I. Smith, W. P. Gibson, and M. K. Doggett, 2008a: Physiographically sensitive mapping of climatological temperature and precipitation across the conterminous United States. *International Journal of Climatology*, **28 (15)**, 2031–2064, doi:10.1002/joc.1688.

Daly, C., M. Halbleib, J. I. Smith, W. P. Gibson, M. K. Doggett, G. H. Taylor, J. Curtis, and P. P. Pasteris, 2008b: Physiographically sensitive mapping of climatological temperature and precipitation across the conterminous United States. *International Journal of Climatology*, **28 (15)**, 2031–2064.

Dee, D. P., and Coauthors, 2011: The ERA-Interim reanalysis: configuration and performance of

the data assimilation system. *Quarterly Journal of the Royal Meteorological Society*, **137 (656)**, 553–597, doi:10.1002/qj.828, URL http://dx.doi.org/10.1002/qj.828.

Delworth, T. L., F. Zeng, A. Rosati, G. A. Vecchi, and A. T. Wittenberg, 2015: A Link between the Hiatus in Global Warming and North American Drought. *Journal of Climate*, **28 (9)**, 3834–3845, doi:10.1175/JCLI-D-14-00616.1, URL https://doi.org/10.1175/JCLI-D-14-00616.1.

Dore, S., and Coauthors, 2010: Carbon and water fluxes from ponderosa pine forests disturbed by wildfire and thinning. *Ecological Applications*, **20 (3)**, 663–683.

Dudley, R. K., and S. P. Platania, 2007: Flow regulation and fragmentation imperil pelagic[U+2010]spawning riverine fishes. *Ecological Applications*, **17 (7)**, 2074–2086, doi: doi:10.1890/06-1252.1, URL https://doi.org/10.1890/06-1252.1.

Enfield, D. B., A. Mestas-Nunez, and P. Trimble, 2001: The Atlantic Multidecadal Oscillation and its relation to rainfall and river flows in the continental U.S. *Geophysical Research Letters*, **28 (10)**, 2077–2080.

Faulstich, H. L., C. A. Woodhouse, and D. Griffin, 2013: Reconstructed cool- and warm-season precipitation over the tribal lands of northeastern Arizona. *Climatic Change*, **118 (2)**, 457–468, doi:10.1007/s10584-012-0626-y.

Flavio, L., D. Clara, S. I. R., and T. Laurent, 2018: Attributing the US Southwest's recent shift into drier conditions. *Geophysical Research Letters*, **0 (ja)**, doi:doi:10.1029/2018GL078312, URL https://doi.org/10.1029/2018GL078312.

Fritze, H., I. T. Stewart, and E. Pebesma, 2011: Shifts in western North American snowmelt runoff regimes for the recent warm decades. *Journal of Hydrometeorology*, **12 (5)**, 989–1006.

Fulp, T., 2005: How low can it go? *Southwest Hydrology*, **4 (2)**, 16–17.

Gao, Y., L. R. Leung, J. Lu, Y. Liu, M. Huang, and Y. Qian, 2014: Robust spring drying in the southwestern U.S. and seasonal migration of wet/dry patterns in a warmer climate. *Geophysical Research Letters*, **41 (5)**, 1745–1751, doi:10.1002/2014GL059562, URL http://dx.doi.org/10.1002/2014GL059562, 2014GL059562.

Gebremichael, M., E. R. Vivoni, C. J. Watts, and J. C. Rodriguez, 2007: Submesoscale spatiotemporal variability of North American monsoon rainfall over complex terrain. *Journal of Climate*, **20 (9)**, 1751–1773.

Geil, K. L., Y. L. Serra, and X. Zeng, 2013: Assessment of CMIP5 Model Simulations of the North American Monsoon System. *Journal of Climate*, **26 (22)**, 8787–8801, doi:10.1175/JCLI-D-13-00044.1, URL https://doi.org/10.1175/JCLI-D-13-00044.1.

Grantz, K., B. Rajagopalan, M. Clark, and E. Zagona, 2007: Seasonal Shifts in the North American Monsoon. *Journal of Climate*, **20 (9)**, 1923–1935, doi:10.1175/JCLI4091.1, URL https://doi.org/10.1175/JCLI4091.1.

Greene, A. M., and R. Seager, 2016: Categorical representation of North American precipitation projections. *Scientific reports*, **6**, 23 888.

Griffin, D., D. M. Meko, R. Touchan, S. W. Leavitt, and C. A. Woodhouse, 2011: Late chronology development for summer moisture reconstruction in the U.S. Southwest. *Tree-Ring Research*, **67 (2)**, 87–101.

Griffin, D., C. A. Woodhouse, D. M. Meko, D. W. Stahle, and H. L. Faulstich, 2013: North

American monsoon precipitation reconstructed from tree-ring latewood. *Geophysical Research Letters*, **40 (5)**, 954–958, doi:10.1002/grl.50184.

Guan, H., E. R. Vivoni, and J. L. Wilson, 2005: Effects of atmospheric teleconnections on seasonal precipitation in mountainous regions of the southwestern US: A case study in northern New Mexico. *Geophysical research letters*, **32 (23)**.

Guirguis, K. J., and R. Avissar, 2008: A Precipitation Climatology and Dataset Intercomparison for the Western United States. *Journal of Hydrometeorology*, **9 (5)**, 825–841, doi:10.1175/2008JHM832.1, URL https://doi.org/10.1175/2008JHM832.1.

Gutzler, D. S., 2013: Streamflow projections for the Upper Gila River. *New Mexico Interstate Stream Commission*.

Gutzler, D. S., D. Kann, and C. Thornbrugh, 2002: Modulation of ENSO-Based Long-Lead Outlooks of Southwestern U.S. Winter Precipitation by the Pacific Decadal Oscillation. *Weather and Forecasting*, **17 (6)**, 1163–1172, doi:10.1175/1520-0434(2002)017⟨1163:MOEBLL⟩2.0.CO;2.

Hamlet, A. F., P. W. Mote, M. P. Clark, and D. P. Lettenmaier, 2007: Twentieth-century trends in runoff, evapotranspiration, and soil moisture in the western united states. *Journal of Climate*, **20 (8)**, 1468–1486, doi:10.1175/JCLI4051.1, URL http://dx.doi.org/10.1175/JCLI4051.1, http://dx.doi.org/10.1175/JCLI4051.1.

Hand, J. L., W. H. White, K. A. Gebhart, N. P. Hyslop, T. E. Gill, and B. A. Schichtel, 2016: Earlier onset of the spring fine dust season in the southwestern United States. *Geophysical Research Letters*, **43 (8)**, 4001–4009, doi:10.1002/2016GL068519, URL http://dx.doi.org/10.1002/2016GL068519, 2016GL068519.

Hidalgo, H. G., and J. A. Dracup, 2003: ENSO and PDO effects on hydroclimatic variations of the Upper Colorado river basin. *Journal of Hydrometeorology*, **4 (1)**, 5–23, doi:10.1175/1525-7541(2003)004⟨0005:EAPEOH⟩2.0.CO;2, URL https://doi.org/10.1175/1525-7541(2003)004⟨0005:EAPEOH⟩2.0.CO;2.

Hidalgo, H. G., and Coauthors, 2009: Detection and attribution of streamflow timing changes to climate change in the western United States. *Journal of Climate*, **22 (13)**, 3838–3855.

Higgins, R. W., Y. Chen, and A. V. Douglas, 1999: Interannual Variability of the North American Warm Season Precipitation Regime. *Journal of Climate*, **12 (3)**, 653–680, doi:10.1175/1520-0442(1999)012⟨0653:IVOTNA⟩2.0.CO;2, URL https://doi.org/10.1175/1520-0442(1999)012⟨0653:IVOTNA⟩2.0.CO;2.

Higgins, R. W., and W. Shi, 2001: Intercomparison of the principal modes of interannual and intraseasonal variability of the north american monsoon system. *Journal of Climate*, **14 (3)**, 403–417, doi:10.1175/1520-0442(2001)014⟨0403:IOTPMO⟩2.0.CO;2, URL https://doi.org/10.1175/1520-0442(2001)014⟨0403:IOTPMO⟩2.0.CO;2.

Hoerling, M., X.-W. Quan, and J. Eischeid, 2009: Distinct causes for two principal u.s. droughts of the 20th century. *Geophysical Research Letters*, **36 (19)**, doi:10.1029/2009GL039860.

Hoerling, M. D. K. W. J. L. J. E. R. N. B. L., M., and K. Kunkel, 2013: *Chapter 5 - Assessment of Climate Change in the Southwest United States: A Report Prepared for the National Climate Assessment*. Island Press, Washington D.C.

Huang, H.-P., R. Seager, and Y. Kushnir, 2005: The 1976/77 transition in precipitation over the

Americas and the influence of tropical sea surface temperature. *Climate Dynamics*, **24 (7-8)**, 721–740.

Hurd, B. H., and J. Coonrod, 2008: *Climate change and its implications for New Mexico's water resources and economic opportunities*. New Mexico State University, Agricultural Experiment Station, Cooperative Extension Service, College of Agriculture and Home Economics.

Jaeger, K. L., J. D. Olden, and N. A. Pelland, 2014: Climate change poised to threaten hydrologic connectivity and endemic fishes in dryland streams. *Proceedings of the National Academy of Sciences*, **111 (38)**, 13 894–13 899.

Jana, S., B. Rajagopalan, M. A. Alexander, and A. J. Ray, 2018: Understanding the Dominant Sources and Tracks of Moisture for Summer Rainfall in the Southwest United States. *Journal of Geophysical Research: Atmospheres*, **123 (10)**, 4850–4870, doi:doi:10.1029/2017JD027652, URL https://doi.org/10.1029/2017JD027652.

Jenkins, M. J., E. Hebertson, W. Page, and C. A. Jorgensen, 2008: Bark beetles, fuels, fires and implications for forest management in the Intermountain West. *Forest Ecology and Management*, **254 (1)**, 16–34, doi:https://doi.org/10.1016/j.foreco.2007.09.045, URL http://www.sciencedirect.com/science/article/pii/S037811270700713X.

Jong, B.-T., M. Ting, R. Seager, N. Henderson, and D. E. Lee, 2017: Role of Equatorial Pacific SST Forecast Error in the Late Winter California Precipitation Forecast for the 2015/16 El Niño. *Journal of Climate*, **31 (2)**, 839–852, doi:10.1175/JCLI-D-17-0145.1, URL https://doi.org/10.1175/JCLI-D-17-0145.1.

Kahya, E., and J. A. Dracup, 1993: US streamflow patterns in relation to the El Niño/Southern Oscillation. *Water Resources Research*, **29 (8)**, 2491–2503.

Kahya, E., and J. A. Dracup, 1994: The influences of type 1 El Nino and La Nina events on streamflows in the Pacific southwest of the United States. *Journal of Climate*, **7 (6)**, 965–976.

Kalnay, E., M. Kanamitsu, R. Kistler, W. Collins, and D. Deaven, 1996: The NCEP/NCAR 40-Year Reanalysis Project. *Bulletin of the American Meteorological Society*, **77 (3)**, 437–471, doi:10.1175/1520-0477(1996)077⟨0437:TNYRP⟩2.0.CO;2.

Karl, T. R., and W. E. Riebsame, 1989: The impact of decadal fluctuations in mean precipitation and temperature on runoff: a sensitivity study over the United States. *Climatic Change*, **15 (3)**, 423–447.

Khedun, C., A. Mishra, M. Özger, H. Kato-Beaudoing, J. Bolten, J. Giardino, and V. Singh, 2010: *Assessing the impacts of climate variability on the water resources in the Rio Grande/Río Bravo basin*, 69–80. American Society of Civil Engineers, doi:doi:10.1061/41114(371)9, URL http://dx.doi.org/10.1061/41114(371)9.

Kiem, A. S., and S. W. Franks, 2004: Multi-decadal variability of drought risk, eastern Australia. *Hydrological Processes*, **18 (11)**, 2039–2050.

Kiem, A. S., S. W. Franks, and G. Kuczera, 2003: Multi-decadal variability of flood risk. *Geophysical Research Letters*, **30 (2)**, n/a–n/a, doi:10.1029/2002GL015992, URL http://dx.doi.org/10.1029/2002GL015992, 1035.

King, A. D., L. V. Alexander, and M. G. Donat, 2013: The efficacy of using gridded data to examine

extreme rainfall characteristics: a case study for Australia. *International Journal of Climatology*, **33 (10)**, 2376–2387, doi:10.1002/joc.3588, URL http://dx.doi.org/10.1002/joc.3588.

Konieczki, A. D., and J. Heilman, 2004: Water-use Trends in the Desert Southwest, 1950-2000. *U.S. Geological Survey Scientific Investigations Report 2004 - 5148*, 32.

Koster, R. D., S. P. P. Mahanama, B. Livneh, D. P. Lettenmaier, and R. H. Reichle, 2010: Skill in streamflow forecasts derived from large-scale estimates of soil moisture and snow. *Nature Geoscience*, **3 (9)**, 613–616, URL http://dx.doi.org/10.1038/ngeo944.

Kurc, S. A., and E. E. Small, 2007: Soil moisture variations and ecosystem-scale fluxes of water and carbon in semiarid grassland and shrubland. *Water Resources Research*, **43 (6)**, n/a–n/a, doi:10.1029/2006WR005011, URL http://dx.doi.org/10.1029/2006WR005011.

Kushnir, Y., R. Seager, M. Ting, N. Naik, and J. Nakamura, 2010: Mechanisms of Tropical Atlantic SST Influence on North American Precipitation Variability. *Journal of Climate*, **23 (21)**, 5610–5628, doi:10.1175/2010JCLI3172.1.

Lee, S., A. Klein, and T. Over, 2004: Effects of the El Niño-Southern Oscillation on temperature, precipitation, snow water equivalent and resulting streamflow in the Upper Rio Grande river basin. *Hydrological Processes*, **18 (6)**, 1053–1071, doi:10.1002/hyp.5511, URL http://dx.doi.org/10.1002/hyp.5511.

Lehner, F., E. R. Wahl, A. W. Wood, D. B. Blatchford, and D. Llewellyn, 2017: Assessing recent declines in Upper Rio Grande runoff efficiency from a paleoclimate perspective. *Geophysical Research Letters*, **44 (9)**, 4124–4133.

Liang, X., 1994: A two-layer variable infiltration capacity land surface representation for general circulation models. *Thesis (PH.D.)-University of Washington*.

Liverman, D., and R. Merideth, 2002: Climate and society in the US Southwest: the context for a regional assessment. *Climate Research*, **21 (3)**, 199–218, doi:10.3354/cr021199.

Llewellyn, D., and S. Vaddey, 2013: *West-wide climate risk assessment: Upper Rio Grande Impact Assessment: Report*. US Department of the Interior, Bureau of Reclamation, Upper Colorado Region, Albuquerque Area Office.

Loik, M. E., D. D. Breshears, W. K. Lauenroth, and J. Belnap, 2004: A multi-scale perspective of water pulses in dryland ecosystems: climatology and ecohydrology of the western USA. *Oecologia*, **141 (2)**, 269–281, doi:10.1007/s00442-004-1570-y, URL https://doi.org/10.1007/s00442-004-1570-y.

MacDonald, G. M., 2010: Water, climate change, and sustainability in the southwest. *Proceedings of the National Academy of Sciences*, **107 (50)**, 21 256–21 262, doi:10.1073/pnas.0909651107, URL http://www.pnas.org/content/107/50/21256, http://www.pnas.org/content/107/50/21256.full.pdf.

Mankin, J., S. Richard, S. J. E., C. B. I., W. A. Park, and H. R. M., 2018a: Blue Water Trade-Offs With Vegetation in a CO2-Enriched Climate. *Geophysical Research Letters*, **45 (7)**, 3115–3125, doi:doi:10.1002/2018GL077051, URL https://doi.org/10.1002/2018GL077051.

Mankin, J. S., R. Seager, J. E. Smerdon, B. I. Cook, A. P. Williams, and R. M. Horton, 2018b: Blue water trade-offs with vegetation in a CO2-enriched climate. *Geophysical Re-*

search Letters, **45 (7)**, 3115–3125, doi:doi:10.1002/2018GL077051, URL https://doi.org/10.1002/2018GL077051.

Mankin, J. S., J. E. Smerdon, B. I. Cook, A. P. Williams, and R. Seager, 2017: The Curious Case of Projected Twenty-First-Century Drying but Greening in the American West. *Journal of Climate*, **30 (21)**, 8689–8710, doi:10.1175/JCLI-D-17-0213.1, URL https://doi.org/10.1175/JCLI-D-17-0213.1.

Mantgem, V., and Coauthors, 2009: Widespread increase of tree mortality rates in the western United States. *Science*, **323 (5913)**, 521–524.

Mantua, N. J., S. R. Hare, Y. Zhang, J. M. Wallace, and R. C. Francis, 1997: A Pacific interdecadal climate oscillation with impacts on salmon production. *Bulletin of the american Meteorological Society*, **78 (6)**, 1069–1079.

Maurer, E. P., and D. P. Lettenmaier, 2003: Predictability of seasonal runoff in the Mississippi River basin. *Journal of Geophysical Research: Atmospheres*, **108 (D16)**, n/a–n/a, doi:10.1029/2002JD002555, URL http://dx.doi.org/10.1029/2002JD002555, 8607.

McCabe, G., M. Palecki, and J. Betancourt, 2004: Pacific and Atlantic Ocean influences on multidecadal drought frequency in the United States. *Proceedings of the National Academy of Sciences*, **101 (12)**, 4136–41, doi:10.1073/pnas.0306738101.

Meehl, G. A., and H. Teng, 2007: Multi-model changes in El Niño teleconnections over North America in a future warmer climate. *Climate Dynamics*, **29 (7-8)**, 779–790.

Meko, D. M., and C. H. Baisan, 2001: Pilot study of latewood-width of conifers as an indicator of

variability of summer rainfall in the north american monsoon region. *International Journal of Climatology*, **21 (6)**, 697–708.

Meko, D. M., C. A. Woodhouse, C. A. Baisan, T. Knight, J. J. Lukas, M. K. Hughes, and M. W. Salzer, 2007: Medieval drought in the upper colorado river basin. *Geophysical Research Letters*, **34 (10)**.

Mesinger, F., and Coauthors, 2006: North American regional reanalysis. *Bulletin of the American Meteorological Society*, **87 (3)**, 343–360.

Milly, P. C., and K. A. Dunne, 2016: Potential evapotranspiration and continental drying. *Nature Climate Change*, **6 (10)**, 946.

Molles, M. C., and C. Dahm, 1990: A Perspective on El Niño and La Niña: Global Implications for Stream Ecology. *Journal of the North American Benthological Society*, **9 (1)**, 68–76, doi: 10.2307/1467935.

Mote, P. W., A. F. Hamlet, M. P. Clark, and D. P. Lettenmaier, 2005: Declining mountain snowpack in Western North America. *Bulletin of the American Meteorological Society*, **86 (1)**, 39–49, doi: 10.1175/BAMS-86-1-39, URL https://doi.org/10.1175/BAMS-86-1-39.

Mote, P. W., S. Li, D. P. Lettenmaier, M. Xiao, and R. Engel, 2018: Dramatic declines in snowpack in the western US. *npj Climate and Atmospheric Science*, **1 (1)**, 2, doi:10.1038/s41612-018-0012-1, URL https://doi.org/10.1038/s41612-018-0012-1.

Muldavin, E. H., D. I. Moore, S. L. Collins, K. R. Wetherill, and D. C. Lightfoot, 2008: Above-ground net primary production dynamics in a northern chihuahuan desert ecosystem. *Oecologia*, **155 (1)**, 123–132.

Notaro, M., Z. Liu, R. G. Gallimore, J. W. Williams, D. S. Gutzler, and S. Collins, 2010: Complex seasonal cycle of ecohydrology in the southwest United States. *Journal of Geophysical Research: Biogeosciences*, **115 (G4)**, doi:10.1029/2010JG001382, URL http://dx.doi.org/10.1029/2010JG001382.

Nowak, K., M. Hoerling, B. Rajagopalan, and E. Zagona, 2012: Colorado River basin hydroclimatic variability. *Journal of Climate*, **25 (12)**, 4389–4403, URL http://dx.doi.org/10.1175/JCLI-D-11-00406.1.

Noy-Meir, I., 1973: Desert ecosystems: environment and producers. *Annual review of ecology and systematics*, **4 (1)**, 25–51.

Pascale, S., W. R. Boos, S. Bordoni, T. L. Delworth, S. B. Kapnick, H. Murakami, G. A. Vecchi, and W. Zhang, 2017: Weakening of the North American monsoon with global warming. *Nature Climate Change*, **7**, 806 EP –, URL http://dx.doi.org/10.1038/nclimate3412.

Pascolini-Campbell, M., R. Seager, A. Pinson, and B. I. Cook, 2017: Covariability of climate and streamflow in the Upper Rio Grande from interannual to interdecadal timescales. *Journal of Hydrology: Regional Studies*, **13**, 58–71.

Pascolini-Campbell, M., R. Seager, A. P. Williams, B. I. Cook, and A. Pinson, submitted: Dynamics and variability of the spring dry season in the United States Southwest as observed in AmeriFlux and NLDAS-2 data. *submitted J. Hydrometeorology*.

Pascolini-Campbell, M. A., R. Seager, D. S. Gutzler, B. I. Cook, and D. Griffin, 2015: Causes of interannual to decadal variability of Gila River streamflow over the past century. *Journal*

of Hydrology: Regional Studies, **3**, 494–508, doi:http://dx.doi.org/10.1016/j.ejrh.2015.02.013, URL http://www.sciencedirect.com/science/article/pii/S2214581815000178.

Penelope, M., H. E. K., and G. C. E., 2008: Multiseason climate synchronized forest fires throughtout the 20th century, Northern Rockies, U.S.A. *Ecology*, **89 (3)**, 717–728, doi:doi:10.1890/06-2049.1, URL https://doi.org/10.1890/06-2049.1.

Penna, D., H. Tromp-van Meerveld, A. Gobbi, M. Borga, and G. Dalla Fontana, 2011: The influence of soil moisture on threshold runoff generation processes in an alpine headwater catchment. *Hydrology and Earth System Sciences*, **15 (3)**, 689–702.

Perkin, J. S., and K. B. Gido, 2011: Stream Fragmentation Thresholds for a Reproductive Guild of Great Plains Fishes. *Fisheries*, **36 (8)**, 371–383, doi:doi:10.1080/03632415.2011.597666, URL https://doi.org/10.1080/03632415.2011.597666.

Pierce, D. W., and Coauthors, 2008: Attribution of declining western US snowpack to human effects. *Journal of Climate*, **21 (23)**, 6425–6444.

Raffa, K. F., B. H. Aukema, B. J. Bentz, A. L. Carroll, J. A. Hicke, M. G. Turner, and W. H. Romme, 2008: Cross-scale drivers of natural disturbances prone to anthropogenic amplification: The dynamics of bark beetle eruptions. *BioScience*, **58 (6)**, 501–517, URL http://dx.doi.org/10.1641/B580607.

Rajagopalan, B., N. Kenneth, P. James, H. Martin, H. Benjamin, B. Joseph, R. Andrea, and U. Bradley, 2009: Water supply risk on the Colorado River: Can management mitigate? *Water Resources Research*, **45 (8)**, doi:doi:10.1029/2008WR007652, URL https://doi.org/10.1029/2008WR007652.

Ramesh, N., M. A. Cane, R. Seager, and D. E. Lee, 2017: Predictability and prediction of persistent cool states of the Tropical Pacific Ocean. *Climate Dynamics*, **49 (7-8)**, 2291–2307.

Redmond, K. T., and R. W. Koch, 1991: Surface climate and streamflow variability in the western united states and their relationship to large-scale circulation indices. *Water Resources Research*, **27 (9)**, 2381–2399, doi:10.1029/91WR00690, URL http://dx.doi.org/10.1029/91WR00690.

Regonda, S. K., B. Rajagopalan, M. Clark, and J. Pitlick, 2005: Seasonal Cycle Shifts in Hydroclimatology over the Western United States. *Journal of Climate*, **18 (2)**, 372–384, doi:10.1175/JCLI-3272.1, URL https://doi.org/10.1175/JCLI-3272.1.

Robinson, T. M., K. J. La Pierre, M. A. Vadeboncoeur, K. M. Byrne, M. L. Thomey, and S. E. Colby, 2013: Seasonal, not annual precipitation drives community productivity across ecosystems. *Oikos*, **122 (5)**, 727–738.

Rodell, M., P. Houser, U. Jambor, J. Gottschalck, and Mitchell, 2004: The Global Land Data Assimilation System. *Bulletin of the American Meteorological Society*, **85 (3)**, 381–394, doi:10.1175/BAMS-85-3-381.

Ropelewski, C. F., and M. Halpert, 1996: Quantifying Southern Oscillation-Precipitation Relationships. *Journal of Climate*, **9 (5)**, 1043–1059, doi:10.1175/1520-0442(1996)009⟨1043:QSOPR⟩2.0.CO;2.

Ropelewski, C. F., and M. S. Halpert, 1986: North American Precipitation and Temperature Patterns Associated with the El Niño/Southern Oscillation (ENSO). *Monthly Weather Review*, **114 (12)**, 2352–2362, doi:10.1175/1520-0493(1986)114⟨2352:NAPATP⟩2.0.CO;2.

Ropelewski, C. F., and M. S. Halpert, 1989: Precipitation Patterns Associated with the High Index Phase of the Southern Oscillation. *Journal of Climate*, **2 (3)**, 268–284, doi:10.1175/1520-0442(1989)002⟨0268:PPAWTH⟩2.0.CO;2.

Schubert, S., 2009: A U.S. CLIVAR Project to Assess and Compare the Responses of Global Climate Models to Drought-Related SST Forcing Patterns: Overview and Results. *Journal of Climate*, **22 (19)**, 5251–5272, doi:10.1175/2009JCLI3060.1.

Schubert, S., and Coauthors, 2009: A US CLIVAR project to assess and compare the responses of global climate models to drought-related SST forcing patterns: overview and results. *Journal of Climate*, **22 (19)**, 5251–5272.

Schubert, S. D., M. Suarez, P. Pegion, R. Koster, and J. Bacmeister, 2004: On the cause of the 1930s dust bowl. *Science (New York, N.Y.)*, **303 (5665)**, 1855–1859, doi:10.1126/science.1095048.

Seager, R., L. Goddard, J. Nakamura, N. Henderson, and D. E. Lee, 2014: Dynamical Causes of the 2010/11 Texas–Northern Mexico Drought*. *Journal of Hydrometeorology*, **15 (1)**, 39–68, doi:10.1175/JHM-D-13-024.1.

Seager, R., N. Harnik, W. Robinson, Y. Kushnir, and M. Ting, 2005a: Mechanisms of ENSO-forcing of hemispherically symmetric precipitation variability. *Quarterly Journal of the Royal Meteorological Society*, **131 (608)**, 1501–1527, doi:10.1256/qj.04.96.

Seager, R., A. Hooks, A. P. Williams, B. Cook, J. Nakamura, and N. Henderson, 2015: Climatology, Variability, and Trends in the U.S. Vapor Pressure Deficit, an Important Fire-Related

Meteorological Quantity. *Journal of Applied Meteorology and Climatology*, **54 (6)**, 1121–1141, doi:10.1175/JAMC-D-14-0321.1, URL https://doi.org/10.1175/JAMC-D-14-0321.1.

Seager, R., Y. Kushnir, C. Herweijer, N. Naik, and J. Velez, 2005b: Modeling of Tropical Forcing of Persistent Droughts and Pluvials over Western North America: 1856–2000. *Journal of Climate*, **18 (19)**, 4065–4088, doi:10.1175/JCLI3522.1.

Seager, R., M. Ting, I. Held, Y. Kushnir, and J. Lu, 2007: Model projections of an imminent transition to a more arid climate in southwestern North America. *Science*, **316 (5828)**, 1181–4, doi:10.1126/science.1139601.

Seager, R., M. Ting, C. Li, N. Naik, B. Cook, J. Nakamura, and H. Liu, 2012: Projections of declining surface-water availability for the southwestern united states. *Nature Climate Change*, **3**, 482 EP –, URL http://dx.doi.org/10.1038/nclimate1787.

Seager, R., M. Ting, C. Li, N. Naik, B. Cook, J. Nakamura, and H. Liu, 2013: Projections of declining surface-water availability for the southwestern United States. *Nature Climate Change*, **3 (5)**, 482.

Seager, R., and G. A. Vecchi, 2010a: Greenhouse warming and the 21st century hydroclimate of southwestern North America. *Proceedings of the National Academy of Sciences*, **107 (50)**, 21 277–21 282, doi:10.1073/pnas.0910856107, URL http://www.pnas.org/content/107/50/21277, http://www.pnas.org/content/107/50/21277.full.pdf.

Seager, R., and G. A. Vecchi, 2010b: Greenhouse warming and the 21st century hydroclimate of southwestern North America. *Proceedings of the National Academy of Sciences*, **107 (50)**, 21 277–21 282, doi:10.1073/pnas.0910856107.

Seth, A., S. A. Rauscher, M. Biasutti, A. Giannini, and S. J. Camargo, 2013: CMIP5 projected changes in the annual cycle of precipitation in monsoon regions. *Journal of Climate*, **26 (19)**, 7328–7351, doi:10.1175/JCLI-D-12-00726.1.

Sheffield, J., G. Goteti, and E. F. Wood, 2006: Development of a 50-year high-resolution global dataset of meteorological forcings for land surface modeling. *Journal of Climate*, **19 (13)**, 3088–3111.

Sheppard, P., A. Comrie, G. Packin, K. Angersbach, and M. Hughes, 2002: The climate of the US Southwest. *Climate Research*, **21 (3)**, 219–238, doi:10.3354/cr021219.

Skagen, S. K., C. P. Melcher, W. H. Howe, and F. L. Knopf, 1998: Comparative use of riparian corridors and oases by migrating birds in southeast Arizona. *Conservation Biology*, **12 (4)**, 896–909.

Small, E. E., 2001: The influence of soil moisture anomalies on variability of the North American Monsoon System. *Geophysical Research Letters*, **28 (1)**, 139–142, doi:10.1029/2000GL011652, URL http://dx.doi.org/10.1029/2000GL011652.

Smith, T. M., R. W. Reynolds, T. C. Peterson, and J. Lawrimore, 2008: Improvements to NOAA's Historical Merged Land–Ocean Surface Temperature Analysis (1880–2006). *Journal of Climate*, **21 (10)**, 2283–2296, doi:10.1175/2007JCLI2100.1.

Smith, W., S. C. Reed, C. C. Cleveland, A. P. Ballantyne, W. R. L. Anderegg, W. R. Wieder, Y. Y. Liu, and S. W. Running, 2015: Large divergence of satellite and Earth system model estimates of global terrestrial CO2 fertilization. *Nature Climate Change*, **6**, 306 EP –, URL http://dx.doi.org/10.1038/nclimate2879.

St. George, S., D. M. Meko, and E. R. Cook, 2010: The seasonality of precipitation signals embedded within the North American Drought Atlas. *Holocene*, **20 (6)**, 983–988, doi: 10.1177/0959683610365937.

Stahle, D. W., M. K. Cleaveland, H. D. Grissino-Mayer, R. D. Griffin, and F. K. Fye, 2009: Cool- and Warm-Season Precipitation Reconstructions over Western New Mexico. *Journal of Climate*, **22 (13)**, 3729–3750, doi:10.1175/2008JCLI2752.1.

Stewart, I. T., D. Cayan, and M. D. Dettinger, 2005: Changes toward earlier streamflow timing across western North America. *Journal of climate*, **18 (8)**, 1136–1155.

Sullivan, B. W., T. E. Kolb, S. C. Hart, J. P. Kaye, B. A. Hungate, S. Dore, and M. Montes-Helu, 2011: Wildfire reduces carbon dioxide efflux and increases methane uptake in ponderosa pine forest soils of the southwestern USA. *Biogeochemistry*, **104 (1-3)**, 251–265.

Swetnam, T. W., and J. L. Betancourt, 1990: Fire-Southern Oscillation Relations in the Southwestern United States. *Science*, **249 (4972)**, 1017–1020, doi:10.1126/science.249.4972.1017, URL http://science.sciencemag.org/content/249/4972/1017, http://science.sciencemag.org/content/249/4972/1017.full.pdf.

Taylor, K. E., R. J. Stouffer, and G. A. Meehl, 2011: An Overview of CMIP5 and the Experiment Design. *Bulletin of the American Meteorological Society*, **93 (4)**, 485–498, doi: 10.1175/BAMS-D-11-00094.1, URL https://doi.org/10.1175/BAMS-D-11-00094.1.

Thomas, B. E., 2007: Climatic fluctuations and forecasting of streamflow in the lower Colorado River basin. *Journal of the American Water Resources Association*, **43 (6)**, 1550–1569.

Ting, M., R. Seager, C. Li, H. Liu, and N. Henderson, 2018: Mechanism of Future Spring Drying in the Southwest U.S. in CMIP5 Models. *Journal of Climate*, doi:10.1175/JCLI-D-17-0574.1, URL https://doi.org/10.1175/JCLI-D-17-0574.1.

Tozer, C. R., A. S. Kiem, and D. C. Verdon-Kidd, 2012: On the uncertainties associated with using gridded rainfall data as a proxy for observed. *Hydrology and Earth System Sciences*, **16 (5)**, 1481–1499, doi:10.5194/hess-16-1481-2012, URL http://www.hydrol-earth-syst-sci.net/16/1481/2012/.

Trenberth, K. E., 1997: The Definition of El Niño. *Bulletin of the American Meteorological Society*, **78 (12)**, 2771–2777, doi:10.1175/1520-0477(1997)078⟨2771:TDOENO⟩2.0.CO;2.

Trenberth, K. E., G. W. Branstator, D. Karoly, A. Kumar, N.-C. Lau, and C. Ropelewski, 1998: Progress during TOGA in understanding and modeling global teleconnections associated with tropical sea surface temperatures. *Journal of Geophysical Research: Oceans*, **103 (C7)**, 14 291–14 324, doi:10.1029/97JC01444, URL http://dx.doi.org/10.1029/97JC01444.

Tucker, C. J., J. E. Pinzon, M. E. Brown, and E. Molly, 2004: Global inventory modeling and mapping studies (GIMMS) satellite drift corrected and NOAA-16 incorporated normalized difference vegetation index (NDVI), monthly 1981-2002. *University of Maryland*.

Ukkola, A. M., I. C. Prentice, T. F. Keenan, A. I. J. M. van Dijk, N. R. Viney, R. B. Myneni, and J. Bi, 2015: Reduced streamflow in water-stressed climates consistent with CO2 effects on vegetation. *Nature Climate Change*, **6**, 75 EP –, URL http://dx.doi.org/10.1038/nclimate2831.

United States Census Bureau, P. D., 2018: Annual Estimates of the Resident Population: April 1,

2010 to July 1, 2017 – United States – Metropolitan Statistical Area; and for Puerto Rico. *2017 Population Estimates*.

Vano, J. A., and Coauthors, 2014: Understanding uncertainties in future Colorado River streamflow. *Bulletin of the American Meteorological Society*, **95 (1)**, 59–78.

Vivoni, E. R., H. A. Moreno, G. Mascaro, J. C. Rodriguez, C. J. Watts, J. Garatuza-Payan, and R. L. Scott, 2008: Observed relation between evapotranspiration and soil moisture in the North American monsoon region. *Geophysical Research Letters*, **35 (22)**, n/a–n/a, doi:10.1029/2008GL036001, URL http://dx.doi.org/10.1029/2008GL036001.

Vose, R. S., and Coauthors, 2014: Improved Historical Temperature and Precipitation Time Series for U.S. Climate Divisions. *Journal of Applied Meteorology and Climatology*, **53 (5)**, 1232–1251, doi:10.1175/JAMC-D-13-0248.1, URL https://doi.org/10.1175/JAMC-D-13-0248.1.

Ward, P. J., M. Kummu, and U. Lall, 2016: Flood frequencies and durations and their response to El Niño Southern Oscillation: Global analysis. *Journal of Hydrology*, **539**, 358–378, doi:https://doi.org/10.1016/j.jhydrol.2016.05.045, URL http://www.sciencedirect.com/science/article/pii/S0022169416303122.

Weiss, J. L., D. S. Gutzler, J. E. Allred Coonrod, and C. N. Dahm, 2004: Seasonal and inter-annual relationships between vegetation and climate in central New Mexico, USA. *Journal of Arid Environments*, **57 (4)**, 507–534, doi:https://doi.org/10.1016/S0140-1963(03)00113-7, URL http://www.sciencedirect.com/science/article/pii/S0140196303001137.

Westerling, A. L., H. G. Hidalgo, D. R. Cayan, and T. W. Swetnam, 2006: Warming and Earlier Spring Increase Western U.S. Forest Wildfire Activity. *Science*, **313 (5789)**, 940–

943, doi:10.1126/science.1128834, URL http://science.sciencemag.org/content/313/5789/940, http://science.sciencemag.org/content/313/5789/940.full.pdf.

Wigley, T., and P. Jones, 1985: Influences of precipitation changes and direct CO2 effects on streamflow. *Nature*, **314 (6007)**, 149.

Williams, A., and Coauthors, 2012: Temperature as a potent driver of regional forest drought stress and tree mortality. *Nature Climate Change*, **3**, 292 EP –, URL http://dx.doi.org/10.1038/nclimate1693.

Williams, A. P., C. D. Allen, C. I. Millar, T. W. Swetnam, J. Michaelsen, C. J. Still, and S. W. Leavitt, 2010: Forest responses to increasing aridity and warmth in the southwestern United States. *Proceedings of the National Academy of Sciences*, **107 (50)**, 21 289–21 294.

Williams, A. P., R. Seager, J. T. Abatzoglou, B. I. Cook, J. E. Smerdon, and E. R. Cook, 2015a: Contribution of anthropogenic warming to California drought during 2012–2014. *Geophysical Research Letters*, **42 (16)**, 6819–6828.

Williams, A. P., and Coauthors, 2013: Temperature as a potent driver of regional forest drought stress and tree mortality. *Nature Climate Change*, **3 (3)**, 292–297.

Williams, A. P., and Coauthors, 2014: Causes and Implications of Extreme Atmospheric Moisture Demand during the Record-Breaking 2011 Wildfire Season in the Southwestern United States. *Journal of Applied Meteorology and Climatology*, **53 (12)**, 2671–2684, doi:10.1175/JAMC-D-14-0053.1, URL http://dx.doi.org/10.1175/JAMC-D-14-0053.1.

Williams, A. P., and Coauthors, 2015b: Correlations between components of the water balance

and burned area reveal new insights for predicting forest fire area in the southwest United States. *International Journal of Wildland Fire*, **24 (1)**, 14–26.

Williams, P., C. B. I., S. J. E., B. D. A., S. Richard, and M. J. S., 2017: The 2016 Southeastern U.S. Drought: An Extreme Departure From Centennial Wetting and Cooling. *Journal of Geophysical Research: Atmospheres*, **122 (20)**, 10,888–10,905, doi:doi:10.1002/2017JD027523, URL https://doi.org/10.1002/2017JD027523.

Woodhouse, C., P. G. T., M. Kiyomi, M. S. A., and M. G. J., 2016: Increasing influence of air temperature on upper Colorado River streamflow. *Geophysical Research Letters*, **43 (5)**, 2174–2181, doi:doi:10.1002/2015GL067613, URL https://doi.org/10.1002/2015GL067613.

Woodhouse, C. A., K. E. Kunkel, D. R. Easterling, and E. R. Cook, 2005: The twentieth-century pluvial in the western United States. *Geophysical Research Letters*, **32 (7)**, n/a–n/a, doi:10.1029/2005GL022413, URL http://dx.doi.org/10.1029/2005GL022413.

Woodhouse, C. A., D. M. Meko, D. Griffin, and C. L. Castro, 2013: Tree rings and multiseason drought variability in the lower Rio Grande Basin. *Water Resources Research*, **49 (2)**, 844–850, doi:10.1002/wrcr.20098.

Woodhouse, C. A., D. M. Meko, G. M. MacDonald, D. W. Stahle, and E. R. Cook, 2010: A 1,200-year perspective of 21st century drought in southwestern North America. *Proceedings of the National Academy of Sciences*, **107 (50)**, 21 283–21 288, doi:10.1073/pnas.0911197107, URL http://www.pnas.org/content/107/50/21283, http://www.pnas.org/content/107/50/21283.full.pdf.

Woodhouse, C. A., D. W. Stahle, and J. Villanueva Diaz, 2012: Rio Grande and Rio Conchos water supply variability over the past 500 years. *Climate Research*, **51 (2)**, 147.

Wu, B., T. Zhou, and T. Li, 2009: Contrast of Rainfall–SST Relationships in the Western North Pacific between the ENSO-Developing and ENSO-Decaying Summers. *Journal of Climate*, **22 (16)**, 4398–4405, doi:10.1175/2009JCLI2648.1.

Xia, Y., M. B. Ek, Y. Wu, T. Ford, and S. M. Quiring, 2015: Comparison of NLDAS-2 Simulated and NASMD Observed Daily Soil Moisture. Part I: Comparison and Analysis. *Journal of Hydrometeorology*, **16 (5)**, 1962–1980, doi:10.1175/JHM-D-14-0096.1, URL https://doi.org/10.1175/JHM-D-14-0096.1.

Xia, Y., and Coauthors, 2012: Continental-scale water and energy flux analysis and validation for north american land data assimilation system project phase 2 (nldas-2): 2. validation of model-simulated streamflow. *Journal of Geophysical Research: Atmospheres*, **117 (D3)**.

Zhang, T., J. Perlwitz, and M. P. Hoerling, 2014: What is responsible for the strong observed asymmetry in teleconnections between El Niño and La Niña? *Geophysical Research Letters*, **41 (3)**, 2013GL058 964, doi:10.1002/2013GL058964, URL http://dx.doi.org/10.1002/2013GL058964.

Zhang, Y., Y. Qian, V. Duliere, E. P. Salathe, and L. R. Leung, 2012: ENSO anomalies over the Western United States: present and future patterns in regional climate simulations. *Climatic Change*, **110 (1-2)**, 315–346, doi:10.1007/s10584-011-0088-7.

Zhang, Y., J. M. Wallace, and D. S. Battisti, 1997: ENSO-like Interdecadal Variability: 1900–93. *Journal of Climate*, **10 (5)**, 1004–1020, doi:10.1175/1520-0442(1997)010⟨1004:ELIV⟩2.0.CO;2, URL http://dx.doi.org/10.1175/1520-0442(1997)010⟨1004:ELIV⟩2.0.CO;2.

Appendix

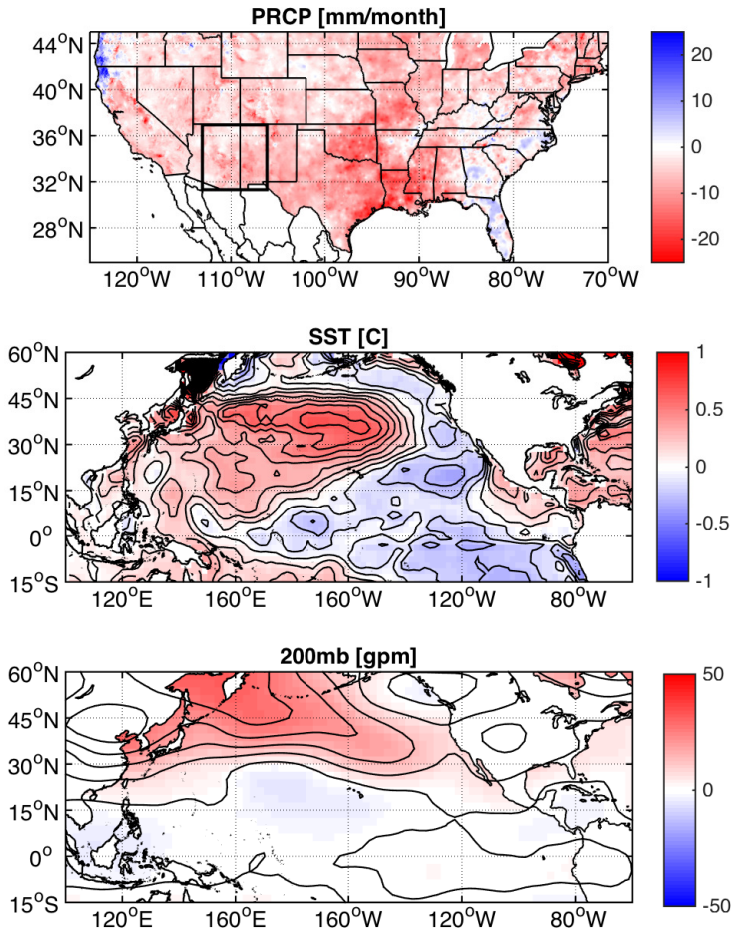

FIG A1. Mid-century dry decades (1948-1966) minus wet decades (1979-97) for a) PRISM precipitation, b) detrended NOAA NCEP-NCAR SST, and c) NOAA NCEP-NCAR 200mb geopotential heights. Contours are plotted at 0.25C intervals for SST, and at 20m intervals for geopotential height.

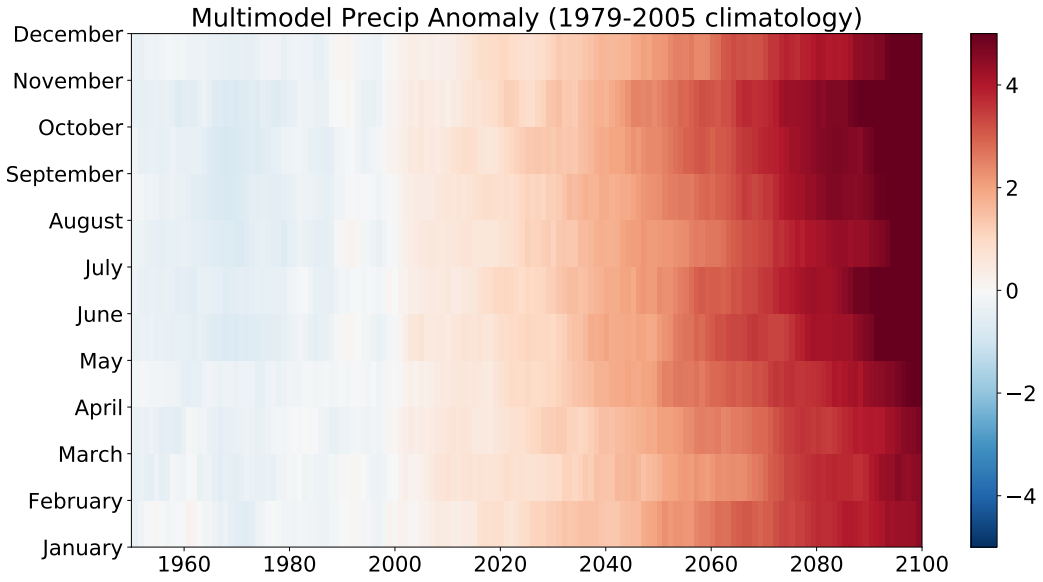

FIG. A2 CMIP5 multi model monthly temperature anomaly (calculated based on 1979-2005 climatology from historical runs). Shading shows value of anomaly [C].

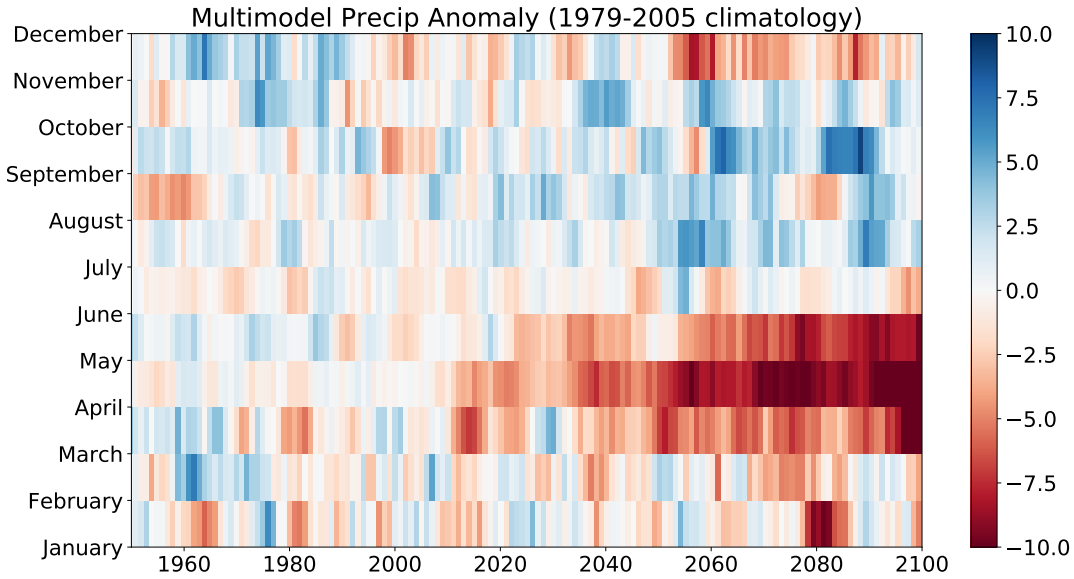

FIG. A3 CMIP5 multi model monthly precipitation anomaly (calculated based on 1979-2005 climatology from historical runs). Shading indicates value of anomaly [mm/month].

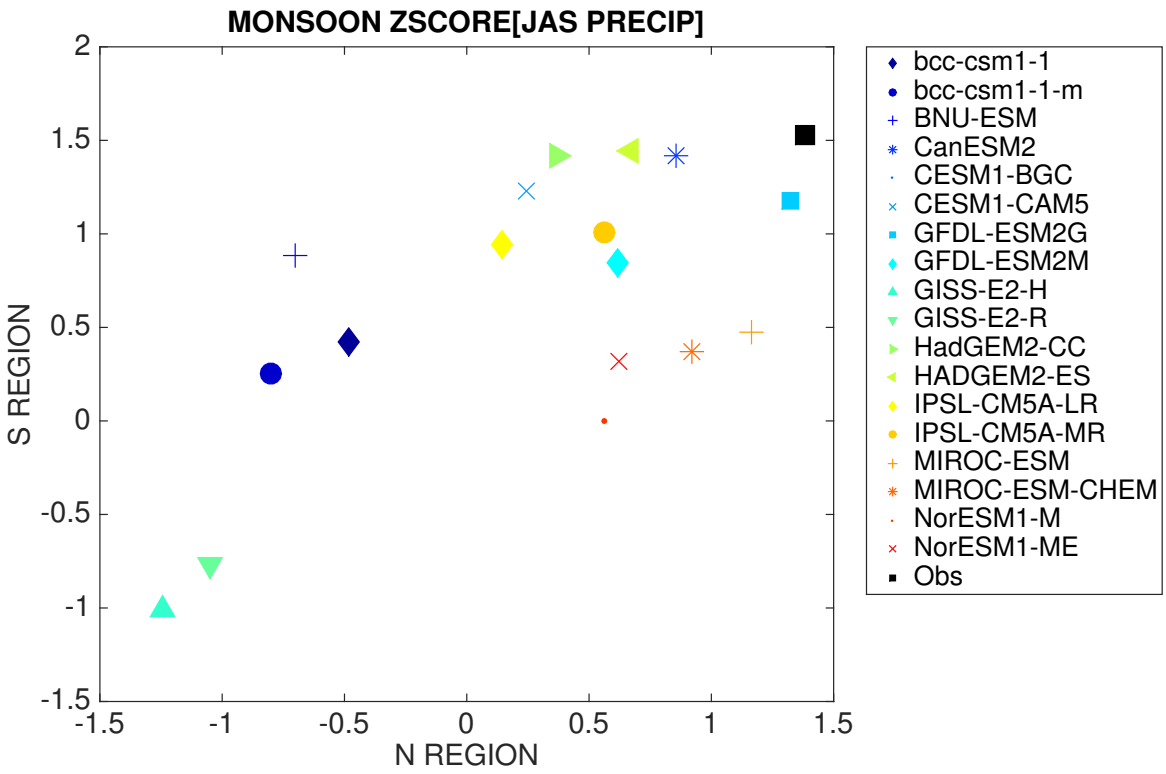

FIG. A4 Standardized JAS precipitation (1979 - 2015) in southern monsoon region (y-axis) correlated against northern monsoon region (x-axis) for 18 CMIP5 models and PRISM observations.